UC Berkeley
UC Berkeley Electronic Theses and Dissertations

Title

Sustainable CO2 valorization by coupling electro- and biocatalysis

Permalink

https://escholarship.org/uc/item/59z8p5g8

Author

Cestellos Blanco, Stefano

Publication Date

2022

Peer reviewed|Thesis/dissertation

eScholarship.org Powered by the California Digital Library
University of California

Sustainable CO_2 valorization by coupling electro- and biocatalysis

By

Stefano Cestellos Blanco

A dissertation submitted in partial satisfaction of the

requirements for the degree of

Doctor of Philosophy

in

Engineering - Materials Science & Engineering

in the

Graduate Division

of the

University of California, Berkeley

Committee in charge:

Professor Peidong Yang, Chair
Professor Phillip B. Messersmith
Professor Adam P. Arkin

Spring 2022

Abstract

Sustainable CO_2 valorization by coupling electro- and biocatalysis

By

Stefano Cestellos Blanco

Doctor of Philosophy in Materials Science & Engineering

University of California, Berkeley

Professor Peidong Yang, Chair

The core of the research presented in this dissertation consists of using solar energy to renewably drive the conversion of CO_2 and N_2 to value-added chemicals, materials, feedstocks, and fuels. Nature has provided a blueprint for capturing and storing solar energy in chemical bonds through photosynthesis. However, our energy demands realistically outmatch the short-term capability of this natural process. Meanwhile, the solar capture ability of semiconductor materials outpaces that of biological organisms. Through my work I have developed photosynthetic biohybrid systems combining the solar capture of semiconductor nanomaterials and the selectivity and low substrate activation of whole cell "living" biocatalysts.

Chapter 1 lays out the current state of the field and how it has evolved from the first demonstrations combining semiconductor materials with whole-cell biocatalysts for CO_2 fixation. In Chapter 2 I describe an approach to improve the interface between light-active silicon nanowires and *Sporomusa ovata* (*S. ovata*), an electrophilic bacterium that converts CO_2 into multi-carbon acetate. The silicon nanowires function as a cathode within an electrochemical cell allowing for a superior interface with the bacterial biocatalysts. *S. ovata* take up electrons at the cathode interface to jumpstart their native CO_2 fixing metabolism. Although considerable efforts have been invested to optimize microorganism species and electrode materials separately, the microorganism-cathode interface has not been systematically studied as a function of operational parameters including applied electrochemical potential, electrolyte composition and biocatalyst loading. We found that as a more negative electrochemical potential was applied to an unoptimized system, the CO_2-reducing current plateaued resulting from a fragmented bioinorganic interface as the bacteria broke away due to increasing local pH**.** By mitigating the pH change at the cathode-bacteria interface, we achieved a direct CO_2 bioelectrosynthesis current density of 0.65 mA cm^{-2} with an ~80% faradaic efficiency. Furthermore, when powered with solar light, our platform attained a 3.6% solar-to-chemical efficiency.

Acetate represents a valuable multi-carbon product because it can be readily used as a feedstock for a secondary bacterium. By carefully selecting a downstream microorganism, we achieved a broader biomanufacturing platform where acetate serves as a universally upgradeable cornerstone. In Chapter 3, I demonstrate that acetate, the primary product of the nanowire-bacteria biohybrid system, can be used as a feedstock for a secondary bacterial biocatalyst that upgrades the acetate to a biopolyester. This proof-of-concept consists of fueling the generation of biopolymer polyhydroxybutyrate (PHB) by *Cupriavidus basilensis* with CO_2-derived acetate Our bioprocess enables the complete conversion of CO_2 to PHB which is to be spun into 3D printing

filament material. Although this demonstration contextualizes the ability to upgrade acetate to a material for additive manufacturing, the production rate is too low for successful industrial scaling. Through modeling of the bioprocess, we uncovered the reaction bottleneck to the be the H_2 mass transfer from the gas phase to the liquid phase during autotrophic cultivation of *S. ovata* with CO_2 and H_2, as reducing substrate. By increasing the H_2 mass transfer modestly, the time required to produce the equivalent mass of acetate would decrease by 75%. Furthermore, adapting the design to a flow cell platform would increase productivity two-fold and limit pH imbalances caused by acetate acidification.

The sequential biocatalysis approach enables the straightforward downstream conversion of the initial CO_2 product acetate to a higher value chemical, fuel, or material by a secondary bacterium. In Chapter 4, I report an advance on this concept by expanding the bioelectrosynthesis beyond CO_2 reduction to include N_2 reduction. We directly co-culture primary CO_2-fixing *S. ovata* producing acetate with a secondary N_2-fixing bacteria in *Rhodopseudomonas palustris* (*R. palustris*) that uses the acetate to both fuel N_2 fixation and for the generation of a biopolyester. We demonstrate that the co-culture platform provides a robust ecosystem for continuous CO_2 and N_2 fixation where its outputs are directed by substrate gas composition. Moreover, we show the ability to support the co-culture on a high surface-area silicon nanowire cathodic platform. The biohybrid co-culture achieved peak faradaic efficiencies of at least 100, 19.1, and 6.3% for acetate, nitrogen in biomass and ammonia respectively while maintaining product tunability. Ultimately, this work demonstrates the ability to employ and electrochemically manipulate bacterial communities on demand to expand the suite of CO_2 and N_2 bioelectrosynthesis products.

There are several advantages of bioelectrochemical CO_2 fixation over the purely inorganic approach. Bioelectrochemical CO_2 fixation offers products that are inaccessible to inorganic electrocatalysis, lower substrate activation energy translating to small overpotentials and the catalysts are self-regenerating and self-repairing. However, inorganic electrocatalysis reduces CO_2 at rates that are orders of magnitudes higher. In Chapter 5 I lay out a roadmap to further combine the best attributes of electrocatalysis and the biologically mediated approach. CO_2 was electrochemically converted to glycolaldehyde using a copper nanoparticle decorated cathode. Glycolaldehyde served as the key autocatalyst for the formose reaction, where it was combined with formaldehyde in the presence of an alkaline earth metal catalyst to form a variety of C_4 - C_8 sugars, including glucose. In turn, these sugars were used as a feedstock for fast-growing and genetically modifiable *Escherichia coli*. By electrocatalytically generating sugars, a high-energy bacterial feedstock, from CO_2 we open the door to biomanufacturing with metabolically rapid and flexible microorganism. There are several obstacles to overcome but we introduce a roadmap to push the boundaries of product complexity achievable from CO_2 conversion while demonstrating CO_2 integration into life-sustaining sugars.

Dedication

I dedicate this work to the women in my life who have made me into the man I am today.

Elvia Carrasquilla, my great-grandmother, who I never had the privilege to meet. It all started with her. She worked in the kitchen of a catholic school in Colombia so that my grandmother could have the education that she never received. She set the expectation that the next generation should always seek more.

Rosa Miguelina Perez Carrasquilla, my grandmother, mi tata, who was a second mother to me. Through her unconditional love, she gave me some of the happiest memories of my childhood. She made everything better. I am so thankful for the time we had together, and I miss her more than words can describe.

Catalina Blanco Perez, my mother, who saw a future for me before I could see it for myself. She made sacrifices, the depths of which I have only come to understand in adulthood, so that I could have a brighter future. Her belief in me has helped me achieve all that I have done and propelled me to always keep growing as a person and as a professional.

Jessica Cestellos Spradlin, my wife and the love of my life. She knows me better than I know myself. She is my thousand suns. She has supported me and helped me navigate the most difficult moments. I wake up every day happy to continue building a life together.

Acknowledgements

When all is said and done the personal connections made during my graduate studies are what I will hold most dear as I move on and progress in my career. Thank you to all of those who took the time to help me, listen to me, volunteered their time, supported me, and advocated on my behalf. I am indebted to you and grateful that our paths crossed.

I would like to thank my Ph.D. advisor Professor Peidong Yang without whom I would not be where I am today. Peidong, thank you for pushing me to see past what simply works and to interrogate the "molecular mechanism" of things. Thank you for having my back in important moments in my Ph.D. while allowing me to freedom to find my own path.

I would like to thank many brilliant researchers, friends, and colleagues from the Yang Group. Firstly, I would like to acknowledge those who were part of the biology subgroup. Our small battalion saw a lot of action together! Thank you to Dr. Hao Zhang who taught me early on much of the bacterial biology. Thank you to Dr. Yue-xiao Shen for being a close friend and trusted colleague. Thank you to Rachel Chan who I saw transition from an inexperienced undergraduate to a confident researcher. Thank you to Tom Tacken for keeping me sane during a tough part of my Ph.D. Thank you to Jimin Kim for a lot of help and insightful discussions. Thank you to Nick Watanabe helping me finish strong. And thank you to Libby Lineberry for helping me become a better mentor.

Secondly, I would like to acknowledge Team SSwEET and other contributors who shaped one of the most impactful projects of my Ph.D. Thank you to Dr. Michael Ross who became a lifelong friend, for advising me through a lot of tough times and for always being down to take on crazy ideas. Thank you to Dr. Yifan Li for big contributions to this project. Thank you to Dr. Sheena Louisia without whom this project would not have been realized. Thank you to Dr. Jessica Cestellos Spradlin and Dr. Tyler Detomasi for contributions in product characterization. And thank you to Nathan Soland for bringing a fresh perspective to this work.

Thirdly, I would like to acknowledge key collaborators who helped me grow as a scientist. From the Yang Group I would like to thank Dr. Sunmoon Yu, Maria Folgueras and Inwhan Roh. I would also like to thank Dr. Zhenni Lin, Martin Siron and Dr. Teng Lei for the great and fun memories we made together. From the wider UC Berkeley community, I would like to acknowledge Anthony Abel, Professor Douglas Clark, Skyler Friedline, Dr. Kyle Sander and Professor Adam Arkin for significant contributions to upgrading acetate. And from Utah State University, I would like to thank Dr. Rhesa Ledbetter and Professor Lance Seefeldt for providing invaluable assistance in exploring N_2 biocatalysis. I would also like to thank my dissertation committee members Professors Peidong Yang, Adam Arkin and Phil Messersmith.

I want to also take a moment to acknowledge many teachers and mentors who prior to my Ph.D. were instrumental in fostering a desire to explore a career in scientific research. Thank you to all the teachers at the German school who saw potential in me. Thank you to several mentors at Stanford without whom I would not have reached graduate school.

And finally, the most emotional thank you to my family for supporting me throughout everything. Thank you again to my wife Jessica. Thank you to my mother Catalina and my stepfather Benjamin. And thank you to my siblings Eric, Carolina and Vicente. I love you all and thank you for being in my life.

Abstract
Dedication
Acknowledgements

Table of Contents

Chapter 1: Introduction **1**

1.1 The case for combining semiconductor inorganic electrocatalysis with whole cell "living" biocatalysts 1

1.2 Photoelectrochemical semiconductor biohybrids 2

1.3 Charge Transfer 4

1.6 Figures 8
Figure 1.1 8

Chapter 2: Overcoming limiting factors affecting the cathode-bacteria interface to boost solar-driven biohybrid CO_2 fixation **9**

2.1 Preface 9

2.2 Introduction 9

2.3 Materials and Methods 10
2.3.1 Preparation of p^+ Si nanowire array electrode 10
2.3.2 Electrochemical characterization 10
2.3.3 Analysis of acetate production 11
2.3.4 Scanning electron microscopy (SEM) characterization 12
2.3.5 Numerical simulation 12
2.3.6 Solar-driven acetate production 13

2.4 Results and Discussion 13
2.4.1 Factors affecting the formation of a close interface between S. ovata and Si nanowire cathode 13
2.4.2 Formation of a close-packed S. ovata and Si nanowire biohybrid and its electrochemical operation 15
2.4.3 Solar-driven operation of the close-packed biohybrid 16

2.5 Figures 17
Figure 2.1 17
Figure 2.2 18
Figure 2.3 19
Figure 2.4 20

Chapter 3: Conversion of acetate from CO_2 to a biopolyester via a tandem biocatalytic process and its potential for space biomanufacturing **21**

3.1 Preface 21

3.2 Introduction 21

3.3 Methods and Materials 23
3.3.1 Cultivation of Sporomusa ovata 23
3.3.2 Cultivation of Cupriavidus basilensis 4G11 23
3.3.3 PHB cell biomass preparation and HPLC analysis 24
3.3.4 Dilution and Aeration of Media 24

3.3.5 Calculation of carbon yield and PHB productivity 24
3.3.6 SEM imaging 24
3.3.7 Modeling of S. ovata growth and acetate production with periodic replenishment of H_2/CO_2 25
3.3.8 Modeling of C. basiliensis growth and PHB accumulation fed by S. ovata spent medium 27
3.4 Results and Discussion 28
3.4.1 Optimization of base medium for bioprocess 28
3.4.2 Process integration for PHB production 29
3.4.3 Qualitative cell population analysis 29
3.4.4 Bioprocess modeling 30
3.4.5 Advantages of minimal processing between bioprocesses 30
3.4.6 Identification of process bottleneck 31
3.4.7 Process consideration for space biomanufacturing 31
3.5 Figures 33
Figure 3.1. 33
Figure 3.2 34
Figure 3.3 35
Figure 3.4 36
Figure 3.5 37
Figure 3.6 37
Chapter 4: Biohybrid co-culture for tandem and tunable CO_2 and N_2 fixation **38**
4.1 Preface 38
4.2 Introduction 38
4.3 Materials and Methods 40
4.3.1 Cell culture 40
4.3.2 Analysis of acetate, ammonia, total nitrogen and hydrogen 40
4.3.3 Electrochemical and solar-driven experiments 41
4.3.4 SEM characterization 43
4.4 Results and Discussion 43
4.4.1 Characterization of individual S. ovata and R. palustris nifA* cultures 44
4.4.2 Characterization and manipulation of S. ovata and R. palustris nifA* co-cultures 45
4.4.3 Electrochemically- and solar-powered S. ovata and R. palustris nifA* based CO_2 and N_2 fixation 47
4.5 Figures 50
Figure 4.1 50
Figure 4.2 51
Figure 4.3 52
Chapter 5: Abiotic sugar synthesis autocatalyzed by CO_2 electrolysis products **54**
5.1 Preface 54
5.2 Introduction 54
5.3 Materials and Methods 55
5.3.1 Electrochemical CO_2 reduction 55
5.3.2 Formose reaction 56
5.3.3 Product and material characterization 57
5.3.4 Cell culture 57
5.4 Results and Discussion 58
5.4.1 CO_2 electrochemical reduction to aldehyde precursors 58

5.4.2 Sugar syntheses using the formose reaction 59
5.4.3 CO_2 electrolysis products as sugar building blocks 60
5.4.4 E. coli cultures supported by CO_2-derived sugars 62
5.5 Figures 63
Figure 5.1 64
Figure 5.2 64
Figure 5.3 65
Figure 5.4 66
Figure 5.5 67
References **68**
Supplementary Information **82**
S.I.: Chapter 2 82
S.I.: Chapter 3 90
S.I.: Chapter 4 95
S.I.: Chapter 5 107

Chapter 1: Introduction

Reproduced[1] in part with permission from:
Cestellos-Blanco, S., Zhang, H., Kim, J. M., Shen, Y. & Yang, P. Photosynthetic semiconductor biohybrids for solar-driven biocatalysis. *Nature Catalysis* **3**, 245–255 (2020).
Copyright 2020, Springer Verlag

1.1 The case for combining semiconductor inorganic electrocatalysis with whole cell "living" biocatalysts

Societal and industrial development has yielded a plethora of benefits for a quickly expanding and interconnected global population. While our quality of life has vastly improved over the last century, it has come at a cost exemplified by depletion of finite energy reserves as well as release of harmful greenhouse gases into the atmosphere contributing to increasingly erratic climatic patterns.[2] The consumption of hydrocarbon fuels is further aggravated, as the carbon ends up as dilute and nearly inert CO_2. In order to prevent further environmental deterioration and secure a lasting energy source, we must find a deployable strategy to simultaneously tap into renewable energy and close the carbon cycle.

In regard to renewable energy, sunlight provides an unparalleled abundance of energy on earth with one hour of solar irradiation matching our yearly global consumption.[3,4] It is no coincidence that earth's biomass is largely derived from solar energy. Although electricity obtained from photovoltaics has gained a foothold in the energy landscape, carbon-based liquid drop-in fuels remain critically important for their stability and high-energy density. Overcoming our global energy challenge will undoubtedly require the development of strategies to harvest and store solar power.[5]

Nature has provided a blueprint for capturing and storing solar energy in chemical bonds in photosynthesis.[6] However, our energy demands realistically outmatch the short-term capability of this natural process.[7] Attempts to directly use plant biomass have resulted in noncompetitive economics and deviation of resources from agricultural needs.[8] Overall, nature does not perform satisfactorily at solar capture as conventional crops only have a 1-2% solar-to-biomass conversion efficiency.[9]

In contrast, inorganic materials, in particular devices consisting of doped semiconductors, have benefited from decades of intense research and technological development. Commercial silicon-based photovoltaic cells customarily reach 20% solar-to-electricity conversion rates even securing profitability.[10] Additionally, photovoltaic-driven electrolysis could achieve at least 10-12% solar energy to water splitting efficiency.[11,12] Advantageously, inorganic light harvesters do not suffer from photodamage and can be engineered to scale to specific light environments. Biological organisms, on the other hand, require a stable light source, and an appropriate climatic environment.[13] Although the benefits of inorganic materials for light capture are significant, they do not hold the upper hand over biology regarding CO_2 fixation. Most semiconducting materials are not suitable catalysts for CO_2 reduction.[14] Therefore, light capture and charge transfer to CO_2

must occur on different platforms. Even though catalysts for CO_2 reduction have progressed expediently, the catalytic understanding necessary for solar-to-chemical conversion is not fully mature.[15] Photoelectrochemical reactors for CO_2 reduction have produced mostly C_1 compounds such as carbon monoxide, methane, methanol and formate.[16,17,18] These devices also suffer from low product selectivity, often employ rare metals and long-term stability has not been entirely fulfilled. By comparison biological organisms engage an army of enzymes and reductive pathways to produce long-chain hydrocarbons from naturally available constituents including CO_2, H_2O and N_2. Enzymes and proteins within the metabolic pathways of cells benefit from an ingrained building code in genetic information and are repaired and replicated as necessary. For these reasons, the combination of inorganic light-harvesters and whole-cell biocatalysts would exploit the most salient attributes of each component. In particular, semiconducting nanomaterials are highly configurable, pair well with cellular organisms due to similar lengths scales and provide adequate light capture.

1.2 Photoelectrochemical semiconductor biohybrids

Economic expansion has rendered the worldwide carbon flux unidirectional with CO_2 serving as a final carbon sink following the utilization of fossil fuels. Nature is the single biggest contributor to atmospheric CO_2 fixation through photosynthesis, however our energy demands vastly outmatch nature's time-scale. Artificial photosynthesis aims to mimic the conversion of CO_2 into value-added carbon products powered by solar energy.[19] Recent advances in semiconductor materials enable broadband light absorption and high photoconversion rates.[20] Photoelectrochemical (PEC) systems integrating light-harvesting semiconducting materials with catalysts primed for CO_2 reduction have been documented.[21,22] These systems obtain light energy from semiconducting electrode materials or external light-harvesters and couple the photoreaction with appropriate catalysts that bind and transfer electrons to CO_2.[15] Nevertheless, even among state-of-the-art CO_2 catalysts, selectivity for products other than CO or formic acid remains poor.[23] Additionally, faradaic efficiencies, a benchmark of catalyst selectivity, for C_{2+} chemicals are low. Natural organisms have evolved to rely on enzymes to convert CO_2 to upgradeable intermediates such as acetyl-CoA and pyruvic acid with exquisite selectivity.[24] Enzymes undertake conformational changes to create local hydrophobic environments and promote steric effects to aid in reaction selectivity.[25] Additionally, dangling amino acid residues mediate electron and proton transfers while stabilizing reactive intermediates.[26] Electron transfer between purified enzymes and electrodes has been studied for conversion of chemical energy to electricity,[27] CO_2 fixation,[28] water splitting[29] and chemical sensing[30]. This approach leverages the product specificity of enzymatic catalysts as well as circumvents product and energy losses due to secondary biomass accumulation. However, combining proteins *in vitro* within a PEC setup results in stability issues.[31] Enzymes inhabit unique protective environments and often operate synergistically with other proteins and organelles; therefore coupling purified enzymes with electrodes is nontrivial. Additionally, connecting enzymes to an electrode often requires technically advanced procedures.[32] In light of these complications, exploiting the enzymatic machinery within whole-cells could improve stability by preserving innate replication and healing mechanisms.[33] Pairing whole-cell biocatalysts with artificial light-capturing PEC systems could enhance product selectivity and lower energetic barriers of CO_2 activation.

At the outset, the integration of whole-cell biocatalysts with inorganic electrodes forged multiple avenues for powering microbial metabolism for the synthesis of desired chemicals from CO_2 and H_2O.[34,35] An early demonstration of microbial electrosynthesis consisted of pairing acetogen *Sporomusa ovata* (*S. ovata*) with a graphite cathode.[36] The electrons transferred to *S. ovata* facilitated the reduction of CO_2 into organic carbon compounds via the Wood-Ljungdahl pathway (WLP).[37] Conveniently, acetate is a byproduct of the WLP as CO_2 is converted to acetyl-CoA, which is oxidized to acetate in ATP phosphorylation. The faradaic efficiency of acetate, as calculated by accounting for the fraction of electrons passed through the cathode consumed to produce acetate, was found to be over 85%. After the initial demonstration of microbial electrosynthesis to produce multicarbon organic compounds from CO_2, different approaches have been undertaken to improve performance and product selection including optimization of electrode geometry[38], electrode surface engineering[39,40] as well as bacteria adaptation[41], enrichment[42] and genetic modification.[43]

Liu *et al*. realized solar-to-chemical microbial electrosynthesis by loading *S. ovata* into a light-harvesting semiconductor nanowire PEC cell (fig. 1.1a).[44] Si and TiO_2 photoactive nanowires captured simulated sunlight and provided *S. ovata* with electrons to drive CO_2 reduction. The Si nanowire substrate can accommodate higher loading of *S. ovata* than planar substrates. The high-surface-area nanowire platform allows for greater interface between the bacteria and cathode which enhances current density — a measure of the rate of CO_2 fixation. Additionally, the nanowire electrodes create a local anaerobic environment that maintains the viability of *S. ovata* even with oxygenic headspace gas. Significantly, the *S. ovata* – nanowire biohybrids were completely operated under simulated sunlight without an external bias achieving a peak CO_2-reducing photocurrent of -0.35 mA/cm^2 with circa 90% faradaic efficiency at an operating overpotential of 0.2V. The overall energy conversion efficiency under simulated sunlight was 0.38%. The bioproduced acetate was upgraded to value-added multicarbon products, such as *n*-butanol, polyhydroxybutyrate (PHB), and isoprenoid by genetically altered *Escherichia coli* (*E. coli*) (fig. 1 a). Altogether this study demonstrates the ability of semiconductor biohybrids to replicate photosynthesis by combining CO_2, sunlight and H_2O into fuels, polymers, and pharmaceuticals.

Autotrophic organisms may also consume H_2 as a form of reducing equivalent.[34,45,46] Therefore, H_2 can be considered as a charge mediator to facilitate microbial electrosynthesis. In this case the cathode may be used as an electrolyzer to reduce water (fig. 1 b). Accordingly, cathodic materials with appropriate H_2 catalytic activity at neutral pH need to be selected. Nichols et al. paired platinum and nickel based H_2 electrocatalysts with *Methanosarcina barkeri* to convert CO_2 to methane.[47] The faradaic efficiency of this device was tabulated at 81% over three days with a -0.29 mA/cm^2 current density. Additionally, the electrodes were substituted with an indium phosphide photocathode and a titanium dioxide photoanode to create an unassisted solar-driven system with 74% faradaic efficiency. Moreover, Liu et al. illustrated that cobalt-based H_2 catalysts can be used in conjunction with genetically engineered *Ralstonia eutropha* (later renamed *Cupriavidus necator*) to produce biomass, poly-β-hydroxybutyrate (PHB) and alcohols from CO_2.[48] The biocompatible cobalt phosphorous electrodes produce H_2 and O_2 under low driving voltage while minimizing reactive oxygen species (ROS) generation, which had previously inhibited microbial metabolism.[43,49] The authors report that their system could achieve 7.6% and 7.1% solar-to-chemical efficiencies for PHB and fusel alcohols respectively if paired with a

photovoltaic device. Notably, these cobalt-based electrodes were used in a following study with *Xanthobacter autotrophicus* (*X. autotrophicus*) to fix N_2 gas into NH_3 and nitrogenous biomass.[50] Nevertheless, the low solubility of H_2 in aqueous media as a mediator limits the throughput of microbial electrosynthesis. Recently, Rodrigues et al. employed a biocompatible perfluorocarbon nanoemulsion as an H_2 carrier thus increasing the solubility of H_2.[51] This strategy was successfully combined with *S. ovata* helping the model system achieve a current density of $2mA/cm^2$ with near 100% faradaic efficiency.

1.3 Charge Transfer

A fundamental question arises from the growing field of electricity driven CO_2 biofixation: how do cells use reducing equivalents? Fundamental charge transfer studies performed on bioelectrochemical systems provide a knowledge base. Although autotrophic bacteria can commonly use H_2 as a source of energy, many such organisms have also evolved the ability to establish direct electrical contact. Electroactive bacteria can transport electrons to and from a poised electrode.[52] The charge transfer mechanism in particular between an anode and charge donating bacteria has been investigated.[53,54] Membrane-bound proteins can shuttle electrons across the cell membrane.[55] Surface displayed cytochromes and flavins are commonly involved in this process but evolving research constantly yields new information on charge uptake pathways.[56] The oxidation of inorganic mineral oxides mediated by electrostatic interactions is carried out by surface-displayed hemoproteins. Exemplarily, Fukushima et al. report that extracellular electron transfer protein MtrF, a terminal protein in cytochrome c from *Shewanella oneidensis* MR-1 binds to mineral oxides by creating a three-dimensional positively charged pocket of specific residues.[57] Moreover, electrotrophic bacteria may also secrete proteins and small molecules that act as redox shuttles as well as extracellular polymers, coined as microbial nanowires.[58,59] Cryoelectron microscopy was used to discern the structure of microbial nanowires in *Geobacter sulfurreducens* responsible for long-range electron transport.[60] It was determined that the nanowires consist of hexaheme cytochrome OmcS with hemes assembled within 3-6Å of each other. Electron conduction occurs through the core of the filaments over the tightly packed metal-cluster hemes.

The platform established by cell-nanoparticle hybrids may serve to study the charge transfer between biotic-inorganic interfaces spectroscopically. Namely, the translucent and light-activated biohybrid samples facilitate their *in situ* observation by spectroscopic means. Transmittance-based transient absorption (TA) and time-resolved infrared spectroscopy (TRIR) were employed to elucidate charge carrier lifetimes in *M. thermoacetica* – CdS.[61] The photoexcited reducing equivalents may be taken up by hydrogenase or directly as electrons by membrane-bound proteins. Through appropriate experimental design, the biochemical activity of proteins involved with charge uptake was correlated with charge carrier lifetimes. *M. thermoacetica* – CdS constructs were incubated with hydrogen pre-photosynthesis for varying lengths of time to ramp up hydrogenase activity. The rate of acetate production was higher in the first three hours for those samples with no hydrogen incubation, but the average rate of acetate production was higher in the samples with the longest hydrogen incubation time. TA results showed that bare CdS had the slowest decay kinetics followed by *M. thermoacetica* – CdS with no hydrogen incubation while *M. thermoacetica* – CdS with hydrogen incubation exhibited the fastest decay. These observations

indicate that a CdS-to-hydrogenase electron transfer pathway may be established. Interestingly, the TRIR spectra highlight a change in vibrational range of CO and CN double and triple bonds corresponding to amino acid residues. These changes occur on the same time scale as the TA signal. While the spectral changes in the TRIR spectra occur in hydrogen and non-hydrogen incubated samples, slight differences point to two charge uptake mechanisms. Photoexcited electrons feed directly into proteins accelerating acetate production in samples with limited hydrogenase activity but cannot maintain long-term metabolic activity due to lack of high energy reducing equivalents. Whereas a CdS-to-hydrogenase electron transfer pathway is established in samples with sufficient hydrogenase activity to produce high energy reducing equivalents.

Kornienko et al. proposed photoinduced charge transfer mechanisms in photosensitized whole-cells based on spectroscopic differences between CdS-containing cells and a control group. Nevertheless, further investigation to identify and quantify the proteins involved during CdS-induced photosynthesis would provide crucial insights. Zhang and colleagues probed the proteome and metabolome of hybrid cells by high sensitivity mass spectrometry techniques.[62] Firstly, they found that membrane bound proteins ferredoxin, flavoprotein and NADH dehydrogenase are upregulated in *M. thermoacetica* – CdS indicating that these proteins are responsible for electron uptake. These electrons are further integrated into bacterial metabolism by shuttling menaquinones where they are used to reduce CO_2 to acetyl-CoA with CO dehydrogenase and acetyl synthase. It is worth remarking that upregulation of ATP synthase was observed adding an additional energy production pump. Proteins involved in the tricarboxylic acid (TCA) cycle and glycolysis were significantly upregulated in *M. thermoacetica* – CdS. Citrate and oxaloacetic acid stemming from acetyl-CoA are primary drivers of the TCA cycle. Finally a part of glycolysis important for cell growth functions was activated. Notably, reducing equivalents can be produced from glycolysis and TCA cycle thus contributing to a host of cell functions.

1.5 Outlook

The coupling of whole-cell biocatalysts and semiconducting nanomaterials has allowed for the light-driven conversion of CO_2, H_2O and N_2 into value-added products. Research has centered around the biotic-abiotic interface, namely to create a functional flux of reducing equivalents either by direct electron transfer or through a mediator like H_2. Although there have been significant developments in this field of research, there is room for improvement and challenges that need to be met.

Direct electron transfer to microorganisms is hindered by the change in pH of the microenvironment at the cathode and the relatively low extracellular electron transfer rate. The first limitation can be addressed by using a better buffering system and by designing an electrochemical cell with superior mass transport. Furthermore, upgrading from a primarily batch to a flow system could enhance biocompatibility. Flow-based microbial fuel cells with markedly improved performance have been reported.[63] With thorough understanding of extracellular electron transfer, bacteria could be genetically engineered to overexpress proteins responsible for charge uptake. This would greatly complement electrochemical adaptation studies. Non-electroactive workhorse bacteria with wide product arrays could even be engineered to accept charge. For instance, S. cerevisiae had not shown electroactivity but S. cerevisiae – InP hybrids successfully regenerated NADPH with light energy.[64] Moreover, microorganisms rarely exist in monocultures in nature. In fact, communities of organisms join forces to symbiotically exploit

available sources of energy. Co-cultured organisms demonstrate synergistic effects as higher resiliency to stresses and overall increase in biomass.[65,66] Employing a diverse community of organisms can enhance the rate of microbial electrosynthesis as has been demonstrated.[67] Furthermore, a study by Lu and colleagues shows that bacterial communities derive photoexcited reducing equivalents from illuminated Mn and Fe oxides. This report provides an account of light-induced bacterial electrotrophy in nature and indicates that there is the need for further investigation into the synergistic relationship between light, cells, and semiconducting materials. Furthermore, this research could provide the foundation for photoelectrochemical semiconductor biohybrids with earth abundant oxides and a larger variety of biocatalysts.

Some of the highest current densities of microbial CO_2 reduction have been achieved by using H_2 as a reducing equivalent.[51] Taking this into consideration, solar power could provide the necessary energy to drive HER to power biocatalysts by coupling HER catalysts with light-absorbing materials. However, HER catalysts at the solid/liquid interface may obscure the semiconductor and thus decrease light harvesting. An alternative strategy consists of pairing a conventional photovoltaic device with an electrolyzer. High (30%) solar-to-hydrogen efficiency has been attained by photovoltaic electrolysis systems.[68] Therefore it stands to reason that producing more hydrogen efficiently could increase the total throughput of solar-based CO_2 reduction. The challenge persists, however of maintaining a biocompatible environment. Fewer studies on N_2 assimilation by microbial electrosynthesis have surfaced. The reason for this might be that nitrogen-fixing bacteria quickly consume valuable NH_3. Liu et al were forced to inhibit protein biosynthesis in order draw extracellular NH_3. Therefore, nitrogenous biomass accumulation and NH_3 production could not be observed simultaneously. This points to a root challenge with microbial electrosynthesis — competition with biocatalysts for access to products may arise.[69]

Moreover, improvements on the biological aspect of semi-artificial photosynthesis are necessary to match advances on the bioinorganic interface. Electrochemical CO_2 reduction with inorganic catalysts can achieve CO_2 fixation with rates 10-50 times higher depending on the product.[15] The rate of carbon assimilation metabolism in autotrophic microbes needs to increase to compete with purely inorganic catalysts. This could be done through metabolic engineering of autotrophic organisms[70] or by constructing CO_2-fixing pathways in highly active organisms such as *E. coli.*[71] Although whole-cell biocatalysts possess unrivaled selectivity of many desirable natural products and biofuels[72], yield and generation rate of these products needs to be optimized. This may be addressed by redesigning metabolic pathways.[73]

Photosensitized microorganisms have achieved direct solar-to-chemical conversion. However, most of these systems rely on hole scavengers. TiO_2 nanoparticles have been used to regenerate cysteine, a common scavenger. But as TiO_2 is intrinsically cytotoxic[74] better approaches for scavenger regeneration are needed. Further in-depth study of the interaction between whole-cells and light-active nanoparticles could provide more insight into the molecular pathway of charge uptake. Spectroscopic analyses could be combined with biochemical assays such as transposon sequencing.[75] Moreover, the field of nanocarrier-based drug delivery has solidified the paramount of role of surface chemistry in nanomaterial-cell interaction.[76] More exploration on the effect of surface chemistry of light-absorbing nanomaterials for photosensitization could continue to yield similarly interesting results.

Altogether, the union of biology and nanomaterials has shown promise to fulfill the mission of artificial photosynthesis. The illustrated biohybrid approaches play to the strengths of each component: the replication, self-healing and specificity of whole organisms and solar energy capture of semiconducting nanomaterials. The advent of photosynthetic semiconductor biohybrids has begun to enable to conversion of sunlight into liquid fuels and value-added chemicals. With steady improvements, the prospect of engineered semiconductors nanomaterials enhancing the natural world may be realized.

1.6 Figures

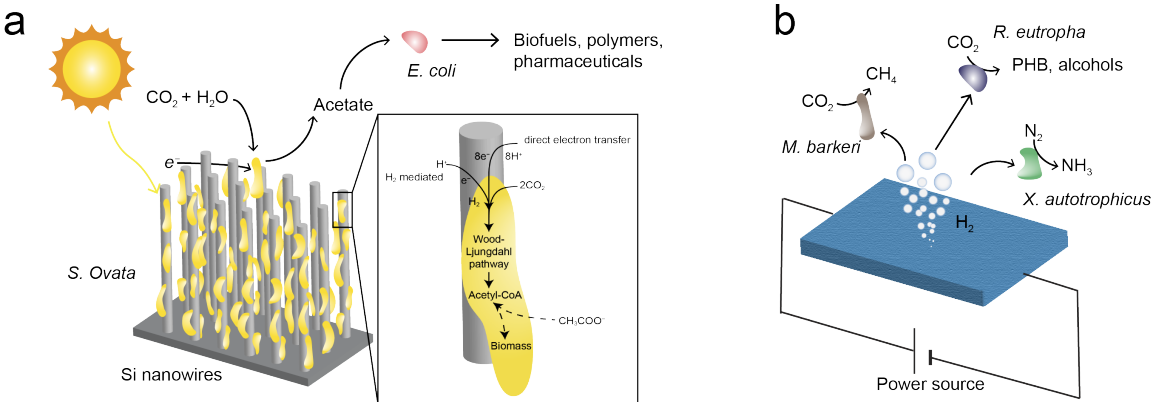


Figure 1.1 Photoelectrochemical semiconductor biohybrids. a. *S. ovata* loaded on light-harvesting nanowires arrays undertake CO_2 to acetate conversion. Genetically engineered *E. coli* upgrades acetate to value-added products. Inset shows the Wood-Ljungdahl pathway leading to acetogenesis. **b.** A contrasting strategy consists of water electrolysis producing H_2. Microbes utilize H_2 as a feedstock to generate CH_4, NH_3, biofuels and polyhydroxybutyrate (PHB).

Chapter 2: Overcoming limiting factors affecting the cathode-bacteria interface to boost solar-driven biohybrid CO_2 fixation

Reproduced[77] in part with permission from:
Su, Y.*, Cestellos-Blanco, S.*, Kim, J.M., Shen, Y.-X., Kong, Q., Lu, D., Liu, C., Zhang, H., Cao, Y., Yang, P. Close-Packed Nanowire-Bacteria Hybrids for Efficient Solar-Driven CO_2 Fixation. *Joule* **4**, 800–811 (2020).
Copyright 2020, Cell Press

2.1 Preface

Liu and coworkers reported the first coupling of a light-active semiconductor silicon nanowires with an electroautotrophic bacterium *S. ovata* in 2015 for the solar-driven conversion of CO_2 to a multi-carbon product. This proof-of-concept demonstrated the ability to sustain living microbes with light. While this represented a laudable advancement in the field, the CO_2 fixing rate was not optimized and the solar-to-chemical conversion efficiency was on the order of a fraction of a percent. This first chapter on original research details the work that went into improving the CO_2 fixation rate and the solar-to-chemical conversion efficiency of the biohybrid platform. An obstacle consisted of the fact that the environment near a cathode will become biologically inhospitable as the pH increases due to the quick consumption of protons. We found that when we accounted for this change by starting with a lower pH electrolyte with a stronger buffer, we could operate the nanowire-bacteria biohybrid at a higher applied bias with a higher current density for CO_2 reduction. This allowed us to drive CO_2 reduction to acetate with light energy at a 3.6% solar-to-chemical conversion efficiency.

2.2 Introduction

Interfacing living cells and inorganic materials has enabled the development of diverse technologies including but not limited to gene editing[78,79] biosensing[80,81] and microbial fuel cells.[82,83] Notably, microorganisms have been introduced as "living" catalysts to the field of catalytic CO_2 fixation.[36,84–89] These microorganisms, principally chemoautotrophic bacteria, have metabolic pathways that can fix CO_2 into multi-carbon products.[90] Biohybrid CO_2-fixing systems, particularly those driven by renewable solar energy, represent a promising strategy for sustainable CO_2-to-chemical conversion.[91] The use of time-evolved living biocatalysts allows for high product selectivity, catalyst regeneration and long-term operation.[42] Remarkably, several of these microorganisms accept extracellular charge transfer and can be directly interfaced with a cathode to carry out CO_2 fixation.[36,88,89] Different strategies have been employed to improve the performance of these hybrid systems, such as optimization of electrode geometry,[92] electrode surface engineering,[93] bacteria adaptation[41,94] and enrichment.[95] Particularly, our group has developed a photoactive and high-surface-area silicon (Si) nanowire electrode that allows for unassisted solar-to-chemical production when paired with acetogen *Sporomusa ovata* (*S. ovata*).[89] The high surface area of the Si nanowire electrode[96] allows for greater bacteria-electrode interface and thus enhanced change transfer rate. However, the CO_2-reducing current of biohybrid systems mediated by direct charge transfer is typically lower than that of electrochemical systems composed of purely inorganic catalysts.[15,97]

Previous work has proposed that the bioinorganic interface is a key determinant of the CO_2-reducing rate.[93] Nevertheless, the dependence of the bioinorganic interface on electrochemical operational parameters including applied overpotential (η), biocatalyst loading and electrolyte pH is poorly understood. Here, we boosted the CO_2-reducing rate of our model Si nanowire/*S. ovata* platform by establishing a robust bacteria-nanowire interface (fig. 2.1). We firstly found that the CO_2-reducing rate at high η was limited by poor bacteria-nanowire interface resulting from an inhospitable alkaline local environment. Tuning the bulk electrolyte pH mitigated the increase in local pH which strengthened the bioinorganic interface. Additionally, this supported higher biocatalyst loading on the nanowire electrode, forming a close-packed nanowire-bacteria cathode. The resulting close-packed biohybrid operated with CO_2-reducing current density ($J_{acetate}$) of 0.65 ± 0.11 mA cm^{-2} at ~-1.2 V *vs.* standard hydrogen electrode (SHE), with a faradaic efficiency of acetate ($FE_{aceatate}$) of ~80%. When coupled with a photovoltaic device, our system enabled solar-powered CO_2 fixation with solar-to-acetate efficiency of ~3.6% and an average daily acetate production rate of 44.3 g m^{-2} or 0.3 g L^{-1} over one week.

2.3 Materials and Methods

2.3.1 Preparation of p^+ Si nanowire array electrode

p^+ Si nanowire arrays were fabricated using reactive-ion etching of patterned single-crystalline Si wafers. The 6-inch p^+-Si (boron) wafers (ρ ~0.001-0.005 Ω. cm) were obtained from Addison Engineering, Inc. After thoroughly cleaning in piranha and buffered hydrofluoric acid (BHF), the wafers were patterned with a photoresist dot array using a standard photolithography stepper. Then the wafers underwent inductive-coupled plasma deep reactive-ion etching (Surface Technology Systems. Inc) to yield uniform nanowire arrays (~20 μm long and ~900 nm in diameter). The Si nanowire arrays were thermally oxidized at 1,000 ºC for 3 hours, followed by etching in BHF for at least 5 minutes. The resulting thinned-down Si nanowires (700-800 nm in diameter) were subsequently coated with 5 nm of TiO_2 protective layer by atomic layer deposition (Picosun ALD), in order to maintain stable performance in a near neutral pH electrolyte for a long period of time. To facilitate the electron transfer from the cathode to the bacterium *S. ovata*, ~10 nm nickel (Ni) were sputtered at the surface of the resulting Si nanowire arrays (Edwards Inc.). For the electrode fabrication, ohmic contact to the device chip was made by rubbing Ga-In eutectic on its back side. Then the chip was fixed on Ti foil with conductive silver paint and carbon tape, resulting in good electrical connections. After that, the Si nanowire array samples were sealed using the nail polish, and the electrodes were ready for electrochemical characterizations.

2.3.2 Electrochemical characterization

S. ovata (DSM 2662) was originally obtained from the American Type Culture Collection (ATCC). An inoculum of *S. ovata* was grown in DSMZ 311 medium (betaine, casitone and resazurin omitted) under strict anaerobic conditions with hydrogen as the electron donor (80% H_2 and 20% CO_2). After 6 days of growth, the OD_{545} would reach 0.372 ± 0.012 (Fig. S1), and such hydrogen-grown bacteria were ready for the subsequent electrochemical CO_2 fixation. All electrochemical measurements were carried out using a home-built electrochemical setup. The setup is a two-chamber cell, with the working electrode and reference electrode (Ag/AgCl, 1M KCl, CH Instruments, Inc) in one chamber and a Pt wire as counter electrode in the other chamber. The two chambers were separated by a proton-exchange membrane (Nafion 212, FuelCellStore)

when standard medium[12, 18] was used as the electrolyte. The nafion membrane was replaced by an anion-exchange membrane (AMI-7001S, kindly provided by Membranes International) when phosphate enhanced medium was used as the electrolyte, to facilitate the mass transport of the negatively-charged phosphate buffer ions and bicarbonate ions. The electrochemical characterization was performed using Gamry Interface 1000 potentiostats. Because of the change of the local pH over the entire experiment, $FE_{acetate}$ and $J_{acetate}$ were both characterized *vs.* SHE defined as following:

$$\text{V } \textit{vs.}\text{ SHE (V)} = \text{V } \textit{vs.}\text{ Ag/AgCl (V)} + 0.209\text{ (V)}$$

The overpotential η for CO_2 reduction is defined as the voltage difference between the applied electrochemical potential and the standard potential for CO_2 reduction into acetic acid:

$$\eta\text{ (V)} = \text{V } \textit{vs.}\text{ RHE (V)} - 0.143\text{ (V)}$$

Here RHE is the reversible hydrogen electrode potential defined as:

$$\text{V } \textit{vs.}\text{ RHE (V)} = \text{V } \textit{vs.}\text{ SHE (V)} + 0.059 \times \text{pH}$$

The nanowire-bacteria hybrids were realized in the cathode chamber using an organic-free minimal medium. Standard medium and phosphate-enhanced medium were both used as the electrolytes, to obtain different levels of proton mass transport, as mentioned above. For the phosphate-enhanced electrolyte, the initial pH value of the electrolyte was systematically tuned from 7.2 to 6.7 and finally 6.4, by adding certain amount of hydrochloric acid. The electrolyte was introduced to the electrochemical cell until its pH value was completely stabilized. We first ran abiotic chronoamperometry (-0.8 V *vs.* SHE) for 24 hours before bacteria inoculation, in order to allow the inert gas bubbling to remove O_2 residue in the cathode chamber. The hydrogen-grown *S. ovata* cells were then inoculated into the cathode chamber (4% v/v at OD_{545} of 0.38 for unoptimized system, and 20% v/v at OD_{545} of 0.38 for optimized system). The inoculation v/v ratio was adjusted accordingly if the OD_{545} slightly differed from 0.38. After bacteria inoculation, the electrochemical bias was kept at -0.8 V *vs.* SHE, and the dispersion was cultured under $80\%N_2/10\%H_2/10\%CO_2$ gas environment for 24 hours. At this stage, the electrolyte in the cathode chamber was turbid due to suspended bacteria. The bubbling gas was then switched to $80\%N_2/20\%CO_2$. At this stage the electrochemical bias (-0.8 V *vs.* SHE) was maintained, and the Si nanowire electrode served as the sole electron source for the bacteria metabolism. The current density was maintained at ~0.15 mA cm^{-2} in order to provide a mild electrochemical environment for the bacteria to become accustomed to. After 24-hour incubation under $80\%N_2/20\%CO_2$, 1/2 of the electrolyte in the cathode chamber was carefully replaced with fresh medium. After one more cycle of such medium exchange, the electrolyte in the cathode chamber became clear as most bacteria settled within the nanowire arrays and stable bacteria-nanowire interface was achieved. Next, the hybrids were ready for electrochemical acetate production as follows.

2.3.3 Analysis of acetate production

Starting from less negative η, chronoamperometry was run for at least 12 hours at each electrochemical bias. After one chronoamperometry cycle was complete, an aliquot of the medium was sampled and a same amount of fresh medium was injected into the electrochemical cell. When nafion membrane was used, aliquots were only sampled from the cathode chamber for acetate analysis. On the other hand, aliquots were sampled from both the cathode chamber and anode chamber for acetate analysis when anion exchange membrane was used. Acetate concentration of the sample was quantified by proton nuclear magnetic resonance (^{1}H-qNMR) spectroscopy with sodium 3-(trimethylsilyl)-2,2',3,3'-tetradeuteropropionate (TMSP-d4) as the internal standard. For the isotope labeling experiment, ^{13}C-labeled bicarbonate was used, and the same protocol was

applied (Fig. S13). After obtaining the acetate concentration of each sample, $FE_{acetate}$ is calculated based on following equation:

$$FE_{acetate} = \frac{96485 \times 8 \times \text{incremental mole of acetic acid}}{\int \mathrm{I}\,\mathrm{dt}}$$

And the specific CO_2-reducing current density $J_{acetate}$ is defined as:

$$J_{acetate} = FE_{acetate} \times J_{total}$$

where J_{total} is the stabilized total current density during chronoamperometry (Fig. S3). In addition to acetate production, the electrons can be also used to produce biomass and H_2. As a result, $FE_{acetate} + FE_{biomass} + FE_{H_2} = 1$

2.3.4 Scanning electron microscopy (SEM) characterization

After the electrochemical characterizations were complete, the nanowire-bacteria hybrids were subjected to SEM characterization. First, an overnight bacteria fixation was performed by adding 2.5% glutaraldehyde directly to the medium in the cathode chamber[40]. Then the electrodes were washed with DI water followed by dehydration in increasing concentrations of ethanol (12.5%, 25%, 37.5%, 50%, 62.5%, 75%, 87.5%, 100%, 15 minutes each). Critical point drying (Tousimis, Inc.) was used to dry the nanowire-bacteria samples, in order to minimize the effect of the capillary force. Prior to imaging, the electrodes were cleaved along the middle and then sputtered with ~5 nm of Au (Denton Vacuum, LLC). The nanowire-bacteria hybrids were imaged at 5 keV/12 μA by field emission SEM (JEOL FSM6430). The density of *S. ovata* could be precisely estimated for the SEM image that showed clear bio-inorganic interface. For the sparsely populated hybrids (Fig. 2a), the cell density was calculated by counting the number of cells within given areas of SEM images (Fig. S2). For the close-packed hybrids, the cell density was estimated by multiplying the density along the z-axis by the density over the x-y plane, as shown in Fig. S8.

2.3.5 Numerical simulation

The local pH within the nanowire arrays was simulated using the Electrochemical Module (steady state) of the COMSOL Multiphysics finite-element-analysis software package. In the 2-dimensional simulations, the nanowire's geometry (20 μm long, 0.8 μm in diameter and 2 μm pitch) is consistent with the experiment. To simplify the model geometry, we use five nanowires to represent the whole nanowire arrays (Figure 3a). Both phosphate buffer (H_3PO_4, $H_2PO_4^-$, HPO_4^{2-} and $PO4^{3-}$) and bicarbonate buffer (H_2CO_3, HCO_3^- and CO_3^{2-}) were accounted in the simulation. In the simulation, the mass transport is governed by the diffusion of ion species. At the nanowire's surface, the proton consumption rate is governed by Tafel equation[41] as following:

$$i = i_0 e^{\frac{-\alpha F \eta}{RT}}$$

where i_0 (exchange current density) and α (transfer coefficient) were both extracted from the experimental Tafel plot. Transfer of one electron corresponds to consumption of one proton. As high-concentration supporting ions were present in the actual electrolyte, the ion migration was not considered in this simulation. The stirring-induced convection was simplified into a diffusion layer model, and the diffusion layer thickness (δ) was assumed to be 50 μm for all the involved ions. Beyond the diffusion layer, the concentrations of all the ions were constant determined by the boundary conditions. The boundary pH value was determined by the experimentally measured bulk pH value in the cathode chamber. Within the diffusion layer, the ion mass transport was governed by the Fick's law. The diffusion coefficients of all ion species were obtained from literature. The equilibrium equations of the buffer systems applied to all the domains. All

equilibrium constants were obtained from literature[41]. The minimum domain mesh size in the simulation is set to be 0.05 μm.

2.3.6 Solar-driven acetate production

For the solar-driven acetate production, a two-electrode configuration was used, where the nanowire-bacteria hybrids worked as the cathode and a Pt wire acted as the anode, respectively. Phosphate-enhanced medium (organic free, initial pH of 6.4) was used as the electrolyte. With the applied electrochemical bias maintained at -3.2 V, the hydrogen-grown *S. ovata* cells (20% v/v inoculum at OD_{545} of 0.38) were introduced into the cathode chamber, where the dispersion was first purged with 80%H_2/10%H_2/20%CO_2 gas mixture for 24 hours. The gas environment was then switched to 80%N_2/20%CO_2, and 1/2 of the electrolyte was replaced with fresh medium every 24 hours (repeated twice), similar to the electrochemical measurements mentioned above. After such medium exchange process, the established nanowire-bacteria hybrids were ready for the solar-driven acetate production. A commercial single-crystalline Si solar cell (KXOB22-01X8F) was obtained from Digi-key Corporation. A 300W Xenon arc lamp (Newport Corporation) with an AM1.5G filter was used for illumination. And the light intensity (25 mW cm^{-2}) was calibrated using a Si photodiode referenced to a NREL calibrated Si photodiode. Once the solar cell was connected to the electrodes, an aliquot of the medium was sampled every 24 hours for acetate quantification, and a same amount of fresh medium was injected into the electrochemical cell. The solar acetate production lasted for 7 days. The daily solar-to-acetate efficiency (ξ) was calculated based on the following equation:

$$\xi = \frac{8 \times 1.09(V) \times N_{acetate}(mol) \times 96485(C\ mol^{-1})}{I(mW\ cm^{-2}) \times A_{sc}(cm^2) \times 24 \times 3600(s)} \times 100\%$$

where 8 represents the number of electrons needed to produce one acetate molecule, 1.09 V is the thermodynamic potential needed to reduce CO_2 into acetate[13], $N_{acetate}$ is the amount of acetate produced in one day, I is the light intensity (25 mW cm^{-2}) and A_{sc} is the projected area of the Si solar cell (0.96 cm^2). Alternatively, ξ can also be expressed based on the calculated averaging $J_{acetate}$ as following:

$$\xi = \frac{1.09(V) \times Averaging\ J_{acetate}(mA\ cm^{-2}) \times A_{electrode}}{I(mW\ cm^{-2}) \times A_{sc}(cm^2)} \times 100\%$$

Where $A_{electrode}$ is the projected area of our Si nanowire electrode (1.2 cm^2).

2.4 Results and Discussion

2.4.1 Factors affecting the formation of a close interface between *S. ovata* and Si nanowire cathode

Liu *et al.* previously demonstrated that Si nanowire arrays with a large surface area could be used to accommodate electrotrophic *S. ovata*.[89] Reducing equivalents generated from the light-harvesting electrodes powered *S. ovata* acetogenesis and thus enabled the conversion of CO_2 into extracellular acetate. In order to focus our scope on the bioinorganic interface and separate it from limitations of the semiconductor-based light harvesting process, we used highly doped conductive p^+ Si nanowire arrays as the cathode material and Pt wire as the counter electrode in lieu of a TiO_2 photoanode. Initially, established inorganic phosphate buffered media[36,93] was used as the

electrolyte (initial pH 7.2), and an *S. ovata* suspension (4% v/v at OD_{545} of 0.38, fig. S2.1) was inoculated into the cathodic chamber of the electrochemical cell (see methods). With this set-up, we investigated the influence of the applied η on acetate production. At the onset of the electrochemical operation, we observed that *S. ovata* was sparsely distributed within the nanowire arrays (fig. 2.2a) as each wire holds an average of ~2.6 cells (fig. S2.2). This system was then subjected to sequentially elevated η from -0.71 V to -1.21 V *vs.* SHE. At low η from -0.71 V to -0.81 V *vs.* SHE, $FE_{aceatate}$ was close to 100% (fig. 2.2b), indicating that the loaded bacteria could efficiently utilize a small flux of reducing equivalents to produce acetate. For example, at -0.81 V *vs.* SHE, the system achieved $FE_{aceatate}$ of 91 ± 19%, and $J_{acetate}$ of ~0.1 mA cm^{-2} that corresponds to an acetate turnover rate (TOR) of ~1.2×10^6 acetate molecules per second per cell (s^{-1} $cell^{-1}$). Our calculation is consistent with previous reported TOR of $(1.0 \pm 0.3) \times 10^6$ acetate molecules s^{-1} $cell^{-1}$.[89] However, simply applying a more negative η did not correspondingly increase the acetate production rate. As we further increased the potential and thus the total current, $FE_{aceatate}$ dramatically decreased and $J_{acetate}$ plateaued at ~0.3 mA cm^{-2} (fig. 2.2b). Specifically, only a 20% $FE_{aceatate}$ could be achieved when the total current density (J_{total}) reached ~1.2 mA cm^{-2}. This suggests that most electrons were lost to H_2 evolution (see fig. 2.1) instead of being directly taken up by the *S. ovata*. In addition, despite a high J_{total}, the peak $J_{acetate}$ of ~0.3 mA cm^{-2} is only comparable with the previously reported value.[89] This CO_2-fixation rate limit motivated our efforts to investigate the cause of the mismatched electron flux at the bioinorganic interface. Through thorough scanning electron microscopy (SEM) imaging, we found that the bacteria-electrode interface was deteriorated after electrochemical operation at -1.21 V *vs.* SHE. We observed large precipitates on the electrode surface (fig. S2.4a and b) possibly stemming from the inorganic compounds in the electrolyte. Energy-dispersive X-ray spectroscopy (EDS) confirmed that the precipitates were mainly composed of calcium phosphate and magnesium phosphate (fig. S2.4c). This is triggered by high pH near the cathode surface due to accelerated proton consumption and inadequate mass transport at high current densities. Increases in local pH have been reported in bioelectrosynthesis as a driving factor for low production rates.[98–100] Methods to inspect pH microenvironments such as colorimetric dyes[101] have been investigated. However, as our nanostructured electrode complicates common pH measurements, we employed numerical 2-D simulations which reveal that the pH around nanowires increases to ~9.3 (fig. S2.5). The alkaline environment not only brought about the formation of bulky precipitates but also created an incompatible environment for the biocatalysts.[100,102] Altogether, this prevented the attachment of *S. ovata* to the electrode (fig. S2.4), and thus impeded direct extracellular electron transfer (fig. 2.1) lowering the overall CO_2-conversion rate.[93] In addition, the negatively charged electrode surface under alkaline condition[103] could further deter adhesion of gram-negative *S. ovata*.[104,105] Based on these findings, we increased the buffer capacity (5X phosphate concentration, initial pH 7.2, denoted as phosphate enhanced media) to mitigate the pH increase around the nanowire cathode. However, enhancing the buffer capacity insignificantly improved the system's performance compared to that of the original electrolyte (fig. S2.6a). At this point we observed that the *S. ovata* persistently escaped from the nanowire array and formed a biofilm on top after operation at -1.21 V *vs.* SHE (fig. S2.6b and c). This observation implies that the local pH environment at high bias is still biologically unfavorable. Furthermore, evolved H_2 may delaminate *S. ovata* from the nanowire electrode.[106] Conclusively, these factors contribute to an obstinately poor bacteria-nanowire interface unable to maintain direct charge uptake at high η.

The formation of a biofilm suggests that the total amount of bacteria increased over the duration of the electrochemical experiment with the phosphate enhanced electrolyte (fig. S2.6b and c), in contradistinction to the sparsely populated initial electrode. Chadwick and Jiménez Otero *et al.* previously verified that the most metabolically active bacteria in current-producing biofilms are those directly interfacing the electrode.[107] This could explain that although a biofilm forms, only those cells closely contacting the nanowires are robustly undertaking acetogenesis. In addition, Zhang *et al.* proposed that a close microbe-electrode interaction can increase the microbial CO_2-reducing rate.[93] Therefore, it is imperative to devise of a strategy to allow the bacteria to inhabit the nanowire array to fully take advantage of the large electrode surface area. Based on our simulation results, we found that the electrolyte with initial pH of 7.2 leads to a slightly basic environment (pH >9, at ~−1.2 V *vs.* SHE) at the electrode interface. Whereas an electrolyte with initial pH of 6.4 could more effectively mitigate the local pH change at a potential of ~−1.2 V *vs.* SHE (fig. 2.3a). Therefore, we hypothesized that a combination of increased buffering capacity and initial lower electrolyte pH could support a robust bacteria-nanowire interface.

2.4.2 Formation of a close-packed *S. ovata* and Si nanowire biohybrid and its electrochemical operation

We monitored the development of *S. ovata* within the nanowire arrays over time (fig. S2.7) employing an enhanced electrolyte with initial pH of 6.4. In order to facilitate the formation of a fully-embedded nanowire-bacteria system and thus allow more bacteria to contribute to acetate production, we inoculated the cathodic chamber with a higher concentration of bacteria initially (20% v/v at OD_{545} of 0.38, Fig. S1). After inoculation, the system was set at −0.8 V *vs.* SHE and the current density was maintained at 0.1 to 0.2 mA cm^{-2}, in order to provide a mild electrochemical environment that the bacteria can become accustomed to. Consequently, a close-packed nanowire-bacteria electrode was formed after a 3-day ramp-up stage with a bacteria density of ~13 cells per nanowire (fig. S2.8). Acetate production from CO_2 on this fully-embedded nanowire-bacteria system was evaluated at a series of sequentially increasing η. Phosphate enhanced electrolytes with three different initial pH values (6.4, 6.7 and 7.2) were used to systematically ascertain the influence of local pH at the electrode interface. The optimized hybrid system with different electrolyte pH all exhibited significantly enhanced $J_{acetate}$ (fig. 2.3b) and $FE_{aceatate}$ (fig. 2.3c) at high η compared to the initial results (fig. 2.2b). The improvement was due to increased electron uptake by the densely packed biocatalysts around the nanowire electrodes. For all three electrolytes, $FE_{aceatate}$ is maintained around 60%~80% at potentials from −1.0 to −1.2 V *vs.* SHE. These results are considerably higher than those of the unoptimized system (Fig. 2b, 20~50%) where initially *S. ovata* was only sparsely distributed around the electrodes. Correspondingly, the peak $J_{acetate}$ was also increased from ~0.3 mA cm^{-2} to >0.45 mA cm^{-2}. For potentials ranging from -0.7 V to -1.1 V *vs.* SHE, the enhanced electrolyte with an initial pH of 6.7 supports the consistently greatest rate of CO_2-to-acetate conversion while the performance of the electrolytes with initial pH of 6.4 and 7.2 is similar. These results suggest that the electrolyte with initial pH 6.7 can sustain an optimal local microenvironment (including pH and preservation of Ni catalyst (Fig. S10)) for *S. ovata* during operating conditions up to -1.1 V *vs.* SHE. Furthermore, the electrolyte with initial pH of 6.4 has a more compelling effect at ~−1.2 V *vs.* SHE allowing for the greatest $J_{acetate}$. SEM inspection after electrochemical operation at ~-1.2 V *vs.* SHE revealed that the bacteria resided on top of electrodes, partially inside the nanowire arrays and densely embedded within the nanowire arrays for electrolytes with initial pH values of 7.2, 6.7 and 6.4,

respectively (fig. 2.3d to f). The different bacteria-nanowire associations are consistent with our simulation results (fig. 2.3a) and indicate that the microbes migrate to their favorable environment under different electrochemical conditions. Correspondingly, the peak $J_{acetate}$ at ~-1.2 V *vs.* SHE was boosted from 0.45 ± 0.05 mA cm^{-2} to 0.57 ± 0.02 mA cm^{-2} and finally up to 0.65 ± 0.11 mA cm^{-2} for electrolytes with initial pH values of 7.2, 6.7 and 6.4, respectively (fig. 2.3b). The improved peak $J_{acetate}$ for initial pH 6.4 suggests that the close-packed bacteria-nanowire interface enhanced electron uptake, as evidenced by the $FE_{aceatate}$ at ~-1.2 V *vs.* SHE (fig 2.3c). pH lower than 6.2 may dissolve the nickel coating on the electrode and therefore the electrolyte pH was not further lowered (fig. S2.10).

The well-preserved bacteria-nanowire interface (fig. 2.3f) allowed us to precisely estimate the bacteria density and thus calculate the TOR per bacterium at high η. At a CO_2-reducing rate of 0.65 ± 0.11 mA cm^{-2} with potential of −1.19 V *vs.* SHE, the TOR of *S. ovata* was (1.7 ± 0.5) × 10^6 acetate molecules s^{-1} cell^{-1}. For potentials higher than -1.2 V *vs.* SHE, we observed more hydrogen formation leading to a much reduced $FE_{aceatate}$ (fig. S2.11). Altogether these results indicate that a potential of ~−1.2 V *vs.* SHE yielded a maximum CO_2-reducing current density of 0.65 ± 0.11 mA cm^{-2} under an optimized system with enhanced bacteria loading and a more bio-compatible local pH.

2.4.3 Solar-driven operation of the close-packed biohybrid

Following the optimization of our microbial electrochemical system we investigated whether our improvements would allow for efficient and sustained solar-to-chemical production.[31,84–89,108] We coupled our close-packed nanowire-bacteria system with a photovoltaic device, as shown in the schematic diagram (fig. 2.4a) and assessed long-term solar-driven CO_2-to-acetate production. The two-electrode electrochemical measurement with the close-packed hybrid system showed an onset voltage of ~1.8 V, and a ~3.2 V operating voltage was needed to reach a current density of ~1 mA cm^{-2} (fig. 2.4b). Therefore, we employed a low-cost multi-junction Si solar cell (V_{oc} 4.7 V, I_{sc} 4.4 mA under one sun illumination) to provide enough voltage to drive the overall reaction. The expected operating current density of the integrated platform was determined by the intersection of the *J-V* curves of both the solar cell (25 mW cm^{-2}, AM 1.5G illumination) and the hybrid system in a two-electrode configuration (fig. 2.4b). The resulting value of ~0.82 mA cm^{-2} matches the optimal total current density found in the electrochemical experiments (fig. S2.12).

The system was found to steadily produce acetate over one week, with daily solar-to-acetate efficiencies between 3~4% and an average acetate production rate of 44.3 g m^{-2} day^{-1} or 0.3 g L^{-1} day^{-1} (fig. 2.4c). Control ^{13}C experiments confirmed the carbon source (fig. S2.13) and a dark control experiment showed negligible acetate production (fig. S2.14). The average 3.6% solar-to-acetate efficiency over seven days corresponds to an average CO_2-reducing current of 0.65 mA cm^{-2}, which is consistent with electrochemical measurements (fig. 2.3b and fig. S2.15). Overall, our results demonstrate a general route to improve the efficiency of bioelectrochemical CO_2 fixation by optimizing the bioinorganic interface. We namely show that a close bioinorganic interface plays a critical role in direct electron uptake in our model system. The insights obtained from this work can be combined with complementary approaches such as bacteria adaptation,[41,94] to further improve the CO_2 conversion rate and solar-to-chemical efficiency.

2.5 Figures

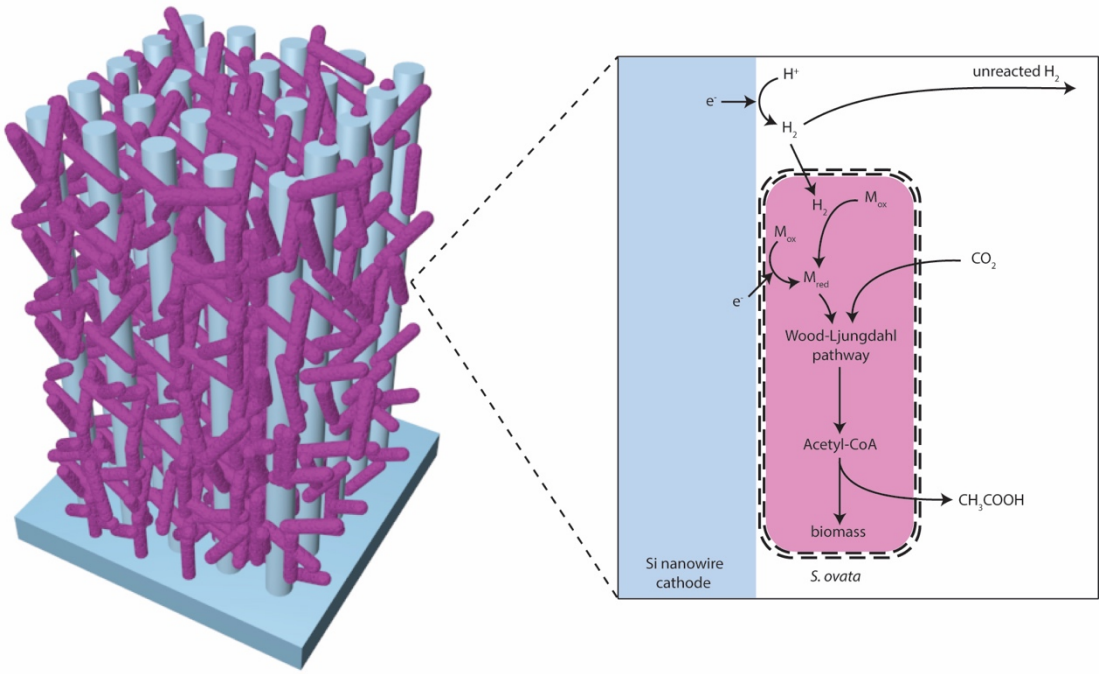


Figure 2.1 Schematics of the close-packed nanowire-bacteria hybrid system (left) and the reaction pathway (right). The electrons are transferred (via either direct pathway[14, 25, 26] or H_2-mediated pathway)[7, 9, 10] from the Si nanowire cathode to *S. ovata* to generate the intracellular reducing equivalents (M_{red}). The reducing equivalents are finally passed on to the Wood-Ljungdahl pathway to produce acetate and biomass.

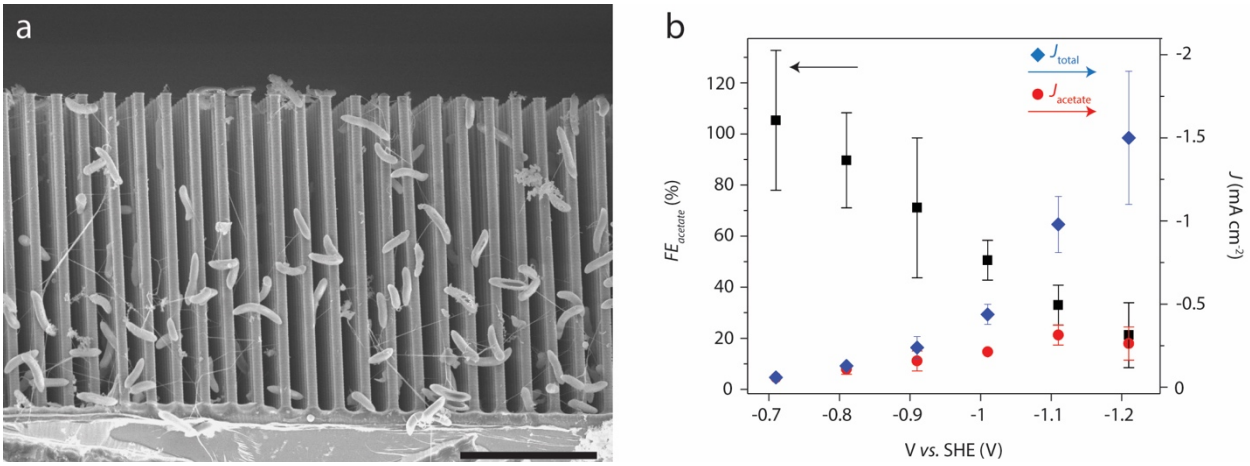


Figure 2.2 The imaging and electrochemical characterizations of nanowire-bacteria hybrids before optimization. a, SEM image of the nanowire-bacteria hybrids (fixed at -0.81 V *vs.* SHE) with standard electrolyte (initial pH value of 7.2) and 4% v/v bacteria inoculation. **b,** The electrochemical performance of the nanowire-bacteria hybrids at different η (starting from less negative η, n=3). $J_{acetate}$ is defined as J_{total} (Fig. S3) multiplied by $FE_{aceatate}$. The scale bar is 10 μm.

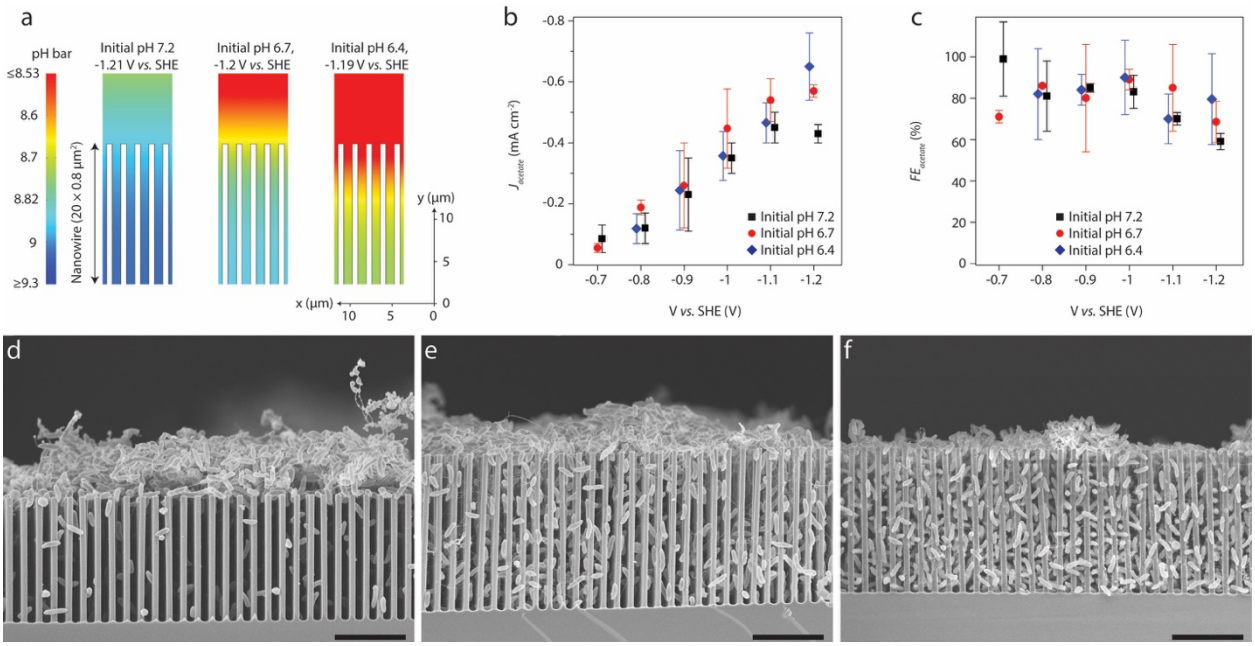


Figure 2.3 The electrochemical performance and SEM images of nanowire-bacteria hybrids with optimized bacteria loading and electrolyte composition. a, Numerical simulations demonstrate that the transition of initial pH values of phosphate enhanced electrolytes from 7.2, 6.7 to 6.4 gradually lowered the pH around the nanowires from >9 to <8.7. The boundary pH values in the simulations were determined by the experimentally measured bulk pH values in the cathode chamber (Fig S9). **b-c,** Bias-dependent $J_{acetate}$ (**b**) and $FE_{aceatate}$ (**c**) of the fully embedded nanowire-bacteria hybrids using phosphate enhanced electrolytes with different initial pH values (n=3 for each case). **d-f,** The SEM images of the fully embedded nanowire-bacteria hybrids after operation at ~-1.2 V vs. SHE using electrolytes with different initial pH values. A clear transition from a top aggregation of bacteria (initial pH value of 7.2, panel d) to a semi-close-packed structure (initial pH value of 6.7, panel e), and finally to a close-packed structure (initial pH value of 6.4, panel f) was observed. The scale bar is 10 μm.

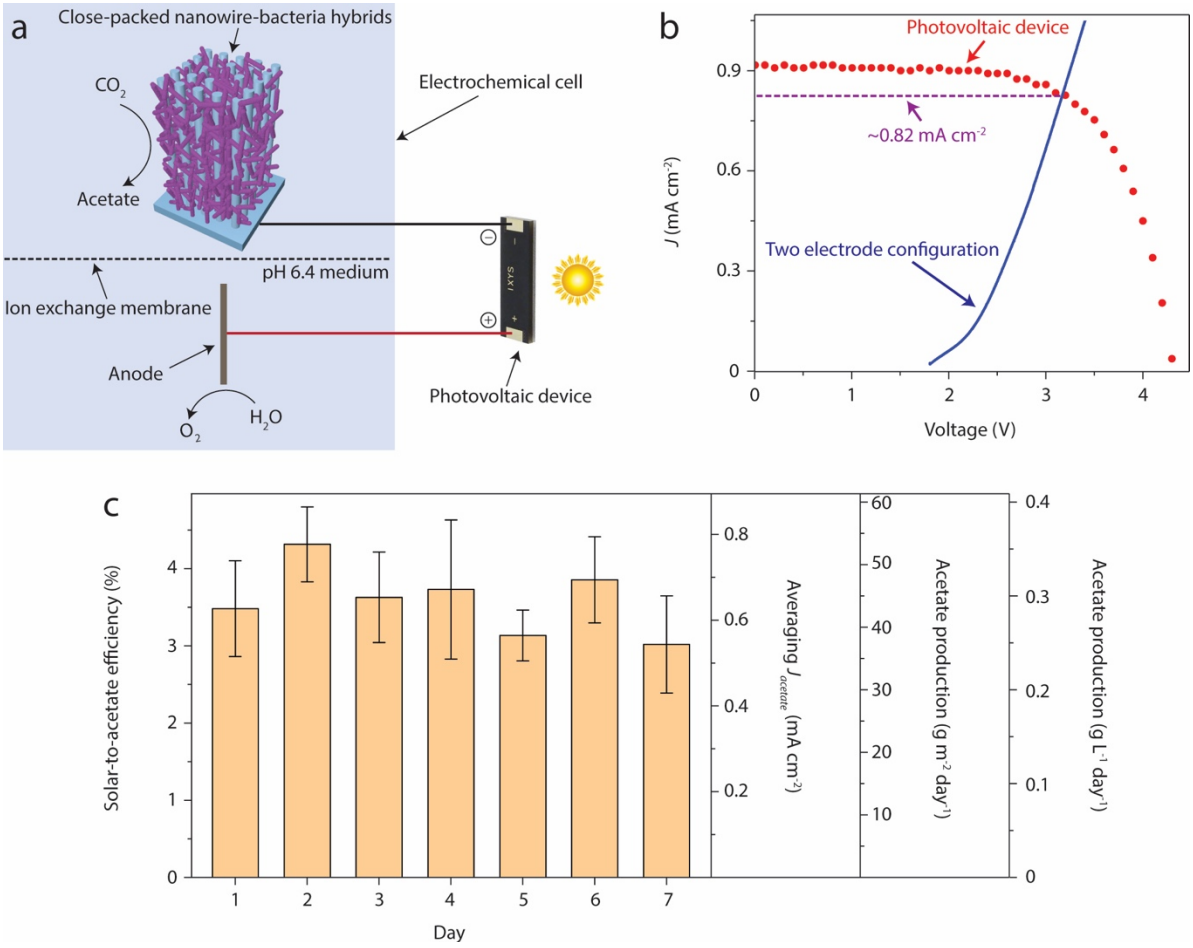


Figure 2.4 Integrating close-packed nanowire-bacteria hybrids with Si solar cell for solar-driven acetate production. a, Schematic illustration of the integrated device mimicking photosynthesis. **b,** *J-V* curves of a multi-junction Si solar cell under 25 mW/cm^2, AM1.5G illumination, and the close-packed nanowire-bacteria hybrids in a two-electrode configuration. **c,** The acetate production and solar efficiency of the device over one week (n=3). The four y axes represent (from left to right) the solar-to-acetate energy conversion efficiency, the calculated daily averaging $J_{acetate}$, the daily acetate production based on electrode projected area and the daily acetate production per unit volume, respectively.

Chapter 3: Conversion of acetate from CO_2 to a biopolyester via a tandem biocatalytic process and its potential for space biomanufacturing

Reproduced[109] in part with permission from:
Cestellos-Blanco, S.*, Friedline, S.*, Sander, K.B., Abel, A.J., Kim, J.M., Clark, D.S., Arkin, A.P., Yang, P. Production of PHB from CO2-derived acetate with minimal processing assessed for space biomanufacturing. *Frontiers in Microbiology* **12**, 2126 (2021).
Copyright 2021, Cestellos-Blanco, Friedline, Sander, Abel, Kim, Clark, Arkin and Yang.

3.1 Preface

The previous chapter dealt with an approach to increase the CO_2 fixation rate in a nanowire-bacteria biohybrid platform by enhancing the biological compatibility of the cathode-cell interface. An advantage to bioelectrochemical CO_2 fixation to acetate is that acetate is an organic acid that is readily consumed by a variety of microorganisms. Though initially it might seem disadvantageous to allow another bacteriun to consume our hard-fought product, we can exploit this by employing a secondary bacterium that makes a more valuable product from the acetate. In this chapter, I detail the use of *Cupriavidus basilensis* which consumes acetate as a primary feedstock and synthesizes a biopolyester that is generally used as a form of energy storage. We can extract the biopolyester which may be used for additive manufacturing. During my graduate studies, my research was largely funded by NASA, with the directive to explore technologies to sustain a crewed deep-space mission to, for instance, Mars. For this reason, this chapter assesses the conversion of CO_2 to the biopolyester through the acetate intermediate for space missions. We developed this process in a way that would minimize the supporting chemicals and equipment and found that by employing our approach the weight requirements could be decreased by up to 98%. We also develop a model to interrogate how to scale this bench scale technology and what bottlenecks need to be overcome to enable its scaling.

3.2 Introduction

Space exploration remains a key aspect of technical and scientific programs of multiple nations.[110] For instance, the National Aeronautics and Space Administration (NASA) has received increased federal funding in the United States as strategic investments call for expansion of crewed space exploration capabilities.[111,112] These efforts are highlighted by the newly established Artemis Program which aims to land women and men on the Moon and Mars, as well as various directorates to fund research into systems enabling human-led deep space exploration.[113–115]

However, the exorbitant costs to transport goods into space represent a major roadblock for space exploration.[116,117] Notably, as human-based mission lengths increase so does the demand for consumables.[118] Additionally, tenuous re-supply lines to faraway locations like Mars could be easily disrupted.[119] Therefore, it is pivotal to transition from missions that solely rely on re-

supplied or pre-deployed stores of single-use consumables to those that sustainably produce and recycle consumables.

In situ resource utilization (ISRU) is the practice to generate products in space from local materials and chemicals. The purpose of ISRU is mainly to support astronauts on long expeditions and could provide products and materials for life support, construction, propellants and energy harvesting.[120] This would also allow for the transport of more goods that would be prohibitively difficult to generate in space (e.g. photovoltaics, experimental equipment) and allow for production flexibility given a change of mission demand. Successful implementation of ISRU will require the harmonious integration of new technological platforms interfacing biotechnology, systems engineering, solar energy harvesting, agriculture, remediation and manufacturing.[121]

There has been heightened interest and research into microorganisms as the core platform to generate consumables and life-support materials in space.[122,123] Autotrophic and diazotrophic microorganisms fix CO_2 and N_2, both of which are present in the Martian atmosphere.[37,124] Single-celled organisms replicate and self-repair; thus, only dried inocula would need to be transported. Bacteria have been reported to produce value-added products including bioplastics, biofuels and pharmaceuticals from CO_2, fix N_2 to fertilizer and aid in waste remediation.[48,50,77,89,125,126] Many strains may be powered directly by solar-generated electricity or by electrochemically produced reducing equivalents such as H_2.[33,127] Here, we present a bacteria-based bioprocess to renewably produce a biopolymer poly(3-hydroxybutyrate) (PHB) from CO_2 while optimizing for ISRU specific requirements.

PHB is a type of polyhydroxyalkanoate (PHA) belonging to a class of bio-polyesters.[128] It accumulates in different bacterial cells and archaea intracellularly triggered by physiological stress when lacking certain nutrients.[129,130] Bacteria employ the biopolymer resulting from carbon assimilation of glucose, starch and organic acids as a form of carbon and energy storage as well as a protectant against stressors.[131–133] PHB is synthesized by the reduction of two condensed acetyl-CoA molecules to produce the hydroxybutyryl-CoA monomer. PHB is biodegradable and has material properties resembling those of polyethylene.[134,135] Additive manufacturing techniques such as 3D-printing can employ PHB that has been extracted from cells and pelletized.[136–138] Altogether, PHB represents a viable pathway for biomanufacturing of material products in space.

Acetogenic bacteria fix CO_2 to acetate and biomass through anaerobic respiration. The Wood-Ljungdhal pathway in acetogens undertakes the reduction of CO_2 to acetyl-CoA which is then used in biosynthesis or converted to acetate gaining ATP. Other minor products of the pathway may include ethanol, 2,3-butanediol and hexanoic acid depending on growth conditions.[139] Acetogens obtain electrons directly from the reduction of minerals, or through the oxidation of electron shuttles or reducing equivalents. Certain acetogens like *Sporomusa ovata* (*S. ovata*) have been found to directly obtain electrons from a poised cathode or from electrochemically generated reducing equivalents like H_2.[51,140] This enables CO_2 bioelectrosynthesis to acetate with high selectivity and long-term stability.

We have employed *S. ovata* as a self-replicating and self-regenerating biocatalyst to fix CO_2 to acetate. We then selected *Cupriavidus basilensis* (*C. basilensis*) for its ability to consume acetate as a primary carbon feedstock (fig. 3.1).[141,142] In addition, *C. basilensis* produces PHB with high

carbon efficiency, and as a significant proportion of biomass. Few accounts have been reported of PHB/PHA production starting from CO_2 as a carbon source.[89,143] And several components of these accounts do not translate well to ISRU-based space production including the low rate of CO_2 fixation and the requirement to purify and concentrate the intermediate carbon molecule before its use in PHA bioproduction. *S. ovata* can directly take up electrons from a cathode for CO_2 to acetate conversion but this approach is limited by the alkaline pH change at the cathode and the bacteria/electrode interface.[52] Therefore, we employ H_2 generated efficiently in separate module to circumvent these challenges. Direct CO_2 bioelectrosynthesis to PHB has also been reported.[48] However, the segmented approach (CO_2 to acetate, acetate to PHB) prevents incompatibilities that arise from combining electrochemistry and biological catalysts such as the requirement to maintain neutral pH. Additionally, a segmented process flow allows for individual unit optimization and overall biomanufacturing modularity.[144,145] For these reasons, we have designed our bioprocess to include a base medium used for both bioreactions - acetate and PHB generation. The ability to directly recycle media circumvents the need for acetate purification and concentration steps which require significant non-ISRU resources (Supplementary Table 3.4). Altogether, we demonstrate peak acetate production from CO_2 of 10.4 mmol acetate L^{-1} day^{-1} which translates to a titer of acetate of 25mM in 2.5 days. This is sufficient for the generation of 12.54 mg PHB L^{-1} $hour^{-1}$. Through modeling this process, we have determined that we can reduce the time to generate 25mM of acetate by 75%. This can be accomplished by increasing the gas to liquid mass transfer of H_2 through improving on bioreactor design.

3.3 Methods and Materials

3.3.1 Cultivation of *Sporomusa ovata*

S. ovata was obtained from the American Type Culture Collection (ATCC 35899) and rehydrated as indicated. It was then grown in DSMZ 311 medium and aliquoted with DMSO as a cryoprotectant at -80°C. Frozen cells were inoculated in DSMZ 311 medium and cultured for two cycles before inoculating in yeast medium (DSMZ 311 medium, casitone, betaine and resazurin omitted). *S. ovata* from yeast medium were inoculated at 5% (v/v) in autotrophic *S. ovata* medium (DSMZ 311 medium, casitone, betaine, resazurin and yeast omitted) with H_2/CO_2 80/20% headspace at 30 PSI. *S. ovata* was consistently incubated at 35 °C in starting pH 7.2 and an orbital shaker was employed for autotrophic growths. Acetate concentration was monitored by ^{1}H-qNMR spectroscopy, with sodium 3- (trimethylsilyl)-2,2',3,3'-tetradeuteropropionate as the internal standard. *S. ovata* from yeast cultures were also inoculated in deoxygenated DM9 (Supplementary Table 3.1) at 10% (v/v) with H_2/CO_2 80/20% headspace at 30 PSI. Balch-type anaerobic culture tubes with butyl stoppers were employed to maintain anaerobicity throughout.

3.3.2 Cultivation of Cupriavidus basilensis 4G11

C. basilensis 4G11 was retrieved from a previously isolated culture from the Oak Ridge Field Research Center Site by Ray and coworkers.[146] To recover the strain from frozen glycerol stocks, it was initially plated on R2A medium agar plates and incubated overnight until colonies formed. A single colony was used to inoculate a starter culture (5mL) of DM9 (Supplementary Table 3.2) media containing 25 mM sodium acetate at pH 7.2 incubated at 30 °C. After incubation overnight,

this culture was centrifuged and washed twice with sterile water to remove residual media before a final resuspension in PBS. Washed cells were used to inoculate experimental conditions at 1% v/v. Optical density of *C. basilensis* cultures was measured at a wavelength of 600 nm using a spectrophotometer (Genesys 30 visible spectrophotometer, thermofisher scientific part number 76308-728).

3.3.3 PHB cell biomass preparation and HPLC analysis

Bacterial culture samples were centrifuged and dried before digestion in 99.99% sulfuric acid (Sigma) for 30 minutes at 90°C; vortexing briefly at 10 minute intervals, according to the protocol of Tyo *et al.* with variations mentioned herein.[147] The acid-digested samples were then allowed to cool to room temperature for 30 minutes prior to filtering the samples through a 0.2 μm PVDF syringe filter. PHB standards were prepared by quantitatively dissolving PHB powder (sigma aldrich 363502-10G) in chloroform and aliquoting requisite amounts, after which the chloroform was allowed to evaporate overnight. The dried PHB standards were then processed alongside the dried cell biomass samples and analyzed as described below.

PHB content was measured in processed samples using a Shimadzu Prominence HPLC system equipped with a Reactive Index Detector. Processed samples were eluted and separated using an Aminex HPX 87H column (BioRad 1250140) equipped with a micro-guard cation H guard column (BioRad part number 1250129) heated to 40C and using 5mM H_2SO_4 as the mobile phase flowing at 0.6 mL/min. PHB was enumerated as crotonic acid monomers (products of the concentrated acid digestion protocol mentioned above) at 206 nm. Pure crotonic acid (Sigma Aldrich 113018), diluted in 5 mM H_2SO_4, was also analyzed to verify accurate crotonic acid retention time.

3.3.4 Dilution and Aeration of Media

The spent and acetate-containing *S. ovata* medium was depressurized and exposed to air prior to *C. basilensis* inoculation. The bottle was loosely covered with a sterile cap and shaken gently for 12 hours to aerate. If necessary, the medium was diluted with sterile water to a final acetate concentration of 25 mM. Cultures of the aerated medium (400mL) were inoculated at 1% v/v with washed *C. basilensis* culture.

3.3.5 Calculation of carbon yield and PHB productivity

PHB productivity was calculated by considering the peak rate of PHB synthesis during the 32-hour growth period. The net mass of PHB was divided by the window of time within which it was produced to give units of g PHB L^{-1} hr^{-1}. Carbon yield from acetate to PHB was derived from the ratio of acetate-carbon consumed to PHB-carbon produced within the window of peak PHB production rate. The units for this metric are reported as % and reflect the fraction of carbon atoms from acetate that were used for PHB synthesis.

3.3.6 SEM imaging

Culture aliquots were taken from the *S. ovata* / *C. basilensis* mixed culture at specific time points. These aliquots were supplemented with glutaraldehyde at 2.5% (v/v) and kept at room temperature

overnight. The samples were washed and consecutively dehydrated with 10% 25% 50% 75% 90% and 100% ethanol each for 10 minutes. 50 μL of dehydrated samples were dropcasted on a 1x1 cm silicon substrate, allowed to dry and imaged with a Quanta 3D field-emission gun SEM (FEI) operated at 10 kV accelerating voltage after gold sputtering.

3.3.7 Modeling of *S. ovata* growth and acetate production with periodic replenishment of H_2/CO_2

Liquid phase mass/mole balances

Growth of cells can be modeled according to the standard design equation for a well-mixed batch bioreactor,[148]

$$\frac{d(c_{\mathrm{X}}V_{\mathrm{L}})}{dt} = \mu V_{\mathrm{L}} c_{\mathrm{X}} \tag{1}$$

where c_{X} is the concentration of cells, V_{L} is the liquid volume of the reactor, and μ is the specific growth rate (hr^{-1}). We assume that acetate is a purely growth-associated product, resulting in

$$\frac{d(c_{\mathrm{Ac}}V_{\mathrm{L}})}{dt} = \alpha\mu V_{\mathrm{L}} c_{\mathrm{X}} \tag{2}$$

where α is the molar ratio of growth-associated product formed to cells produced. Solubilized (in the liquid phase) H_2 and CO_2 are consumed during the production of biomass and acetate, and mass transfer from the gas phase occurs simultaneously. For H_2 in the liquid phase, the resulting balance is

$$\frac{d\left(c_{\mathrm{H_2}}V_{\mathrm{L}}\right)}{dt} = V_L\left(-\frac{1}{Y'_{\mathrm{X/H_2}}}\mu c_{\mathrm{X}} - \frac{1}{Y'_{\mathrm{Ac/H_2}}}\alpha\mu c_{\mathrm{X}}\right) + V_{\mathrm{L}}k_{\mathrm{L}}a(c_{\mathrm{sat,H_2}} - c_{\mathrm{H_2}}) \tag{3}$$

where $Y'_{\mathrm{X/H_2}}$ is the molar biomass yield on H_2, $Y'_{\mathrm{Ac/H_2}}$ is the acetate yield on H_2, $k_{\mathrm{L}}a$ is the gas-liquid mass transfer rate (hr^{-1}) and $c_{\mathrm{sat,H_2}}$ is the saturation concentration of H_2. The saturation concentration is given, to a reasonable approximation, by

$$c_{\mathrm{sat,H_2}} = H_{\mathrm{H_2}}p_{\mathrm{H_2}} \tag{4}$$

where $H_{\mathrm{H_2}}$ is Henry's constant for H_2 in water and $p_{\mathrm{H_2}}$ is the partial pressure of H_2 in the gas phase. Equations (3) and (4) are also valid for CO_2:

$$\frac{d\left(c_{\mathrm{CO_2}}V_{\mathrm{L}}\right)}{dt} = V_L\left(-\frac{1}{Y'_{\mathrm{X/CO_2}}}\mu c_{\mathrm{X}} - \frac{1}{Y'_{\mathrm{Ac/CO_2}}}\alpha\mu c_{\mathrm{X}}\right) + V_{\mathrm{L}}k_{\mathrm{L}}a(c_{\mathrm{sat,CO_2}} - c_{\mathrm{CO_2}}) \tag{5}$$

$$c_{\mathrm{sat,CO_2}} = H_{\mathrm{CO_2}}p_{\mathrm{CO_2}} \tag{6}$$

Gas phase mole balances
In the gas phase, H_2 and CO_2 are consumed by mass transfer into the liquid phase according to:

$$\frac{d\left(p_{\mathrm{H_2}} V_{\mathrm{G}}\right)}{dt} = -V_{\mathrm{L}} k_{\mathrm{L}} a(c_{\mathrm{sat,H_2}} - c_{\mathrm{H_2}})RT \tag{7}$$

and

$$\frac{d\left(p_{\mathrm{CO_2}} V_{\mathrm{G}}\right)}{dt} = -V_{\mathrm{L}} k_{\mathrm{L}} a(c_{\mathrm{sat,CO_2}} - c_{\mathrm{CO_2}})RT \tag{8}$$

Note that these equations assume the gas follows ideal behavior.

Equation coupling and Monod growth kinetics
We assume that the specific growth rate follows Monod kinetics. In this case, μ can be written as

$$\mu = \mu_{\max}\left(\frac{c_{\mathrm{H_2}}}{K_{\mathrm{S,H_2}} + c_{\mathrm{H_2}}}\right)\left(\frac{c_{\mathrm{CO_2}}}{K_{\mathrm{S,CO_2}} + c_{\mathrm{CO_2}}}\right) \tag{9}$$

Because both V_{L} and V_{G} are constant, the liquid phase mass/mole balances are:

$$\frac{dc_{\mathrm{X}}}{dt} = \mu_{\max} c_{\mathrm{X}}\left(\frac{c_{\mathrm{H_2}}}{K_{\mathrm{S,H_2}} + c_{\mathrm{H_2}}}\right)\left(\frac{c_{\mathrm{CO_2}}}{K_{\mathrm{S,CO_2}} + c_{\mathrm{CO_2}}}\right) \tag{10}$$

$$\frac{dc_{\mathrm{Ac}}}{dt} = \alpha\mu_{\max} c_{\mathrm{X}}\left(\frac{c_{\mathrm{H_2}}}{K_{\mathrm{S,H_2}} + c_{\mathrm{H_2}}}\right)\left(\frac{c_{\mathrm{CO_2}}}{K_{\mathrm{S,CO_2}} + c_{\mathrm{CO_2}}}\right) \tag{11}$$

$$\frac{dc_{\mathrm{H_2}}}{dt} = \left(-\frac{1}{Y_{\mathrm{X/H_2}}}\mu c_{\mathrm{X}} - \frac{1}{Y_{\mathrm{Ac/H_2}}}\alpha\mu c_{\mathrm{X}}\right) + k_{\mathrm{L}} a(c_{\mathrm{sat,H_2}} - c_{\mathrm{H_2}}) \tag{12}$$

$$\frac{dc_{\mathrm{CO_2}}}{dt} = \left(-\frac{1}{Y_{\mathrm{X/CO_2}}}\mu c_{\mathrm{X}} - \frac{1}{Y_{\mathrm{Ac/CO_2}}}\alpha\mu c_{\mathrm{X}}\right) + k_{\mathrm{L}} a(c_{\mathrm{sat,CO_2}} - c_{\mathrm{CO_2}}) \tag{13}$$

Mole balances in the gas phase result in

$$\frac{dp_{\mathrm{H_2}}}{dt} = -\frac{V_{\mathrm{L}}}{V_{\mathrm{G}}} k_{\mathrm{L}} a(c_{\mathrm{sat,H_2}} - c_{\mathrm{H_2}})RT \tag{14}$$

and

$$\frac{dp_{\mathrm{CO_2}}}{dt} = -\frac{V_\mathrm{L}}{V_\mathrm{G}} k_\mathrm{L} a (c_{\mathrm{sat,CO_2}} - c_{\mathrm{CO_2}}) RT \tag{15}$$

Periodic gas phase replenishment
To describe the periodic (24-hr) replacement of the gas phase, we generalize the initial conditions for H_2 and CO_2 pressure as

$$\begin{aligned} p_{\mathrm{H_2}}(t = 24n) &= p_{\mathrm{H_2},0} \\ p_{\mathrm{CO_2}}(t = 24n) &= p_{\mathrm{CO_2},0} \end{aligned} \tag{16}$$

where $n \in \mathbb{N}$ and t has units of hrs.

3.3.8 Modeling of C. basiliensis growth and PHB accumulation fed by *S. ovata* spent medium

Liquid phase mole balances
We again use the standard bioreactor design equation,

$$\frac{d(c_\mathrm{X} V_\mathrm{L})}{dt} = \mu_\mathrm{X} V_\mathrm{L} c_\mathrm{X} \tag{17}$$

to describe the accumulation of *C. basiliensis* cells in the liquid volume. Following Mozumder *et al.*[149] the accumulation of PHB is given as

$$\frac{d(c_\mathrm{PHB} V_\mathrm{L})}{dt} = \mu_\mathrm{PHB} V_\mathrm{L} c_\mathrm{X} \tag{18}$$

Acetate is consumed both by biomass and PHB accumulation, resulting in

$$\frac{d(c_\mathrm{Ac} V_\mathrm{L})}{dt} = -\frac{1}{Y'_\mathrm{X/Ac}} \mu_\mathrm{X} V_\mathrm{L} c_\mathrm{X} - \frac{1}{Y'_\mathrm{PHB/Ac}} \mu_\mathrm{PHB} V_\mathrm{L} c_\mathrm{X} \tag{19}$$

Nitrogen is also consumed by biomass accumulation, described as

$$\frac{d(c_\mathrm{N} V_\mathrm{L})}{dt} = -\frac{1}{Y'_\mathrm{X/N}} \mu_\mathrm{X} V_\mathrm{L} c_\mathrm{X} \tag{20}$$

As above, the liquid volume is approximately constant throughout the duration of the experiment.

Growth and PHB Accumulation Kinetics
We use acetate and nitrogen inhibition-modified Monod (Andrews-Haldane) kinetics to describe the kinetics of cell growth:

$$\mu_{\mathrm{X}} = \mu_{\max,\mathrm{X}} \left(\frac{c_{\mathrm{Ac}}}{c_{\mathrm{Ac}} + K_{\mathrm{S,Ac}} + \frac{c_{\mathrm{Ac}}^2}{K_{\mathrm{I,Ac}}}} \right) \left(\frac{c_{\mathrm{N}}}{c_{\mathrm{N}} + K_{\mathrm{S,N}} + \frac{c_{\mathrm{N}}^2}{K_{\mathrm{I,N}}}} \right) \quad (21)$$

where $K_{\mathrm{I},i}$ are inhibition constants. We modify Mozumder *et al.*[149] to describe PHB accumulation:

$$\mu_{\mathrm{PHB}} = \mu_{\max,\mathrm{PHB}} \left(\frac{c_{\mathrm{Ac}}}{c_{\mathrm{Ac}} + K_{\mathrm{S,Ac}} + \frac{c_{\mathrm{Ac}}^2}{K_{\mathrm{I,Ac}}}} \right) \left[1 - \left(\frac{f_{\mathrm{PHB}}}{f_{\mathrm{PHB,max}}} \right)^{\beta} \right] \left(\frac{K_{\mathrm{S,N}}}{c_{\mathrm{N}} + K_{\mathrm{S,N}}} \right) \quad (22)$$

where $f_{\mathrm{PHB,max}}$ is the maximum PHB-to-biomass ratio. In this model we neglect O_2 because O_2 was fully saturated throughout the duration of the experiment. We also neglect the potential PHB consumption due to cell growth once the acetate source is exhausted because PHB is the intended product, so careful process design, *e.g.*, whereby cells are harvested before PHB consumption occurs, can avoid this parasitic impact on PHB accumulation. All model parameters are compiled in supplementary tables 3.2 and 3.3.

3.4 Results and Discussion

3.4.1 Optimization of base medium for bioprocess

We firstly cultured *S. ovata* autotrophically in balch-type 25mL culture tubes with an 80/20% H_2/CO_2 headspace. In these conditions acetate generation rate amounts to 10.4 mmol $L^{-1}day^{-}$, a rate modestly higher than previous reports.[106] We selected 25mM acetate as the feedstock concentration for *C. basilensis*. This titer of acetate was achieved within the first 48-72 hours of the autotrophic *S. ovata* culture. However, the *S. ovata* culture could reach a concentration of 50-60mM acetate in 5-7 days without adjusting for pH which decreases due to acetate accumulation. The *S. ovata* cultures were stopped at 25mM acetate and aerated which rendered the *S. ovata* inactive. *C. basilensis* was then inoculated in the spent *S. ovata* cultures (fig. 3.2a). The increase in biomass as detected by OD_{600} was used to monitor the ability of *C. basilensis* to grow and use the CO_2-derived acetate. The baseline OD resulting from the presence of *S. ovata* biomass in the spent medium was deducted. As compared to *C. basilensis* grown in fresh DM9, which is the recommended *C. basilensis* culture medium, with synthetic acetate the biomass yield in the spent *S. ovata* medium was only 50% within the timeframe of the experiment. We employed a second control with cultured *C. basilensis* in fresh *S. ovata* medium (no prior *S. ovata*) with synthetic acetate. This culture achieved the same biomass yield as the one in the spent *S. ovata* medium indicating that acetate is not incompatible with *C. basilensis* but rather that a component in the *S. ovata* medium inhibits *C. basilensis* growth. In a second medium optimization experiment, we again cultured *S. ovata* autotrophically until the acetate concentration reached 25mM. The spent *S. ovata* medium was diluted twofold with fresh DM9 containing synthetic acetate at 35mM, 25mM and 0mM. Thus the mixed media which were inoculated with *C. basilensis* contained total acetate concentrations of 30mM, 25mM and 12.5mM respectively (fig. 3.2b). The biomass yield in the 25mM culture equaled that of C. basilensis in fresh DM9 in the prior experiments. The

biomass yields in the 30mM and 12.5mM were congruent with the available acetate. While adding fresh DM9 clearly enhanced *C. basilensis* growth, the cultures containing spent *S. ovata* medium had a 20 hour longer lag phase. The peak optical densities were only reached in twice the length of time. Furthermore, it is burdensome to formulate two sets of media. Therefore, we attempted to grow *S. ovata* directly in deoxygenated DM9. We found that a 10% (v/v) inoculum is necessary when culturing *S. ovata* in DM9 whereas normally only a 5% (v/v) would be required. Next, we employed culturing controls in which we added the recommended *S. ovata* medium components to a DM9 base including reducing reagent, vitamins and carbonate (fig. 3.2c and d). Favorably *S. ovata* not only grows well in DM9 but also generates a similar amount of acetate as in the recommended *S. ovata* medium. Significant decreased growth and acetate generation is only detected in the carbonate containing DM9 which could be a result of the increased osmotic pressure of the saline medium.[150]

3.4.2 Process integration for PHB production

Based on the results from the previous experiments we concluded to use DM9 as the base medium for our bioprocess. Before inoculating with *S. ovata*, we deoxygenated the DM9 medium. To gauge PHB productivity, we scaled up our process from 25mL tubes to 1L balch-type bottles each with 270mL of culture medium (fig. 3.3a). There was a significant scale-up associated loss in acetate productivity with the cultures reaching 25mM only after eight days. The *S. ovata* cultures were grown for 14 days and the acetate concentration reached 42mM. We proceeded to culture *C. basilensis* in the aerated spent DM9 which was diluted to 25mM (fig. 3.3b). As expected, the acetate concentration decreases as biomass accumulates. The biomass yield achieved in this experiment was decidedly greater than that obtained in fresh DM9 in fig 3.2a. Additionally, there is no protracted lag phase with the use of 100% DM9 as the base medium. Next, we determined that PHB correlates well with biomass production and we calculated a PHB generation rate of 12.6mg L^{-1} $hour^{-1}$ with an overall 11.06% carbon yield from acetate. After 24 hours there is a decrease in the PHB concentration which correlates with the complete consumption of acetate. This could be due to the cells depleting PHB reserves to acquire carbon and energy.

3.4.3 Qualitative cell population analysis

Scanning electron microscopy has been established as a standard method to elucidate bacterial cell morphology. *S. ovata* is rod-shaped circa 4 μm long and 1 μm wide whereas *C. basilensis* is spherical to oval shaped and circa 2 μm in diameter. These differences in morphology allowed us to qualitatively determine the changing cell populations and establish that *C. basilensis* can grow in spent medium containing inactive *S. ovata*. We fixed culture samples at the 0 hour time point just after inoculating the spent DM9 with *C. basilensis*. As *S. ovata* had achieved approximately 0.12 OD_{545}, we expected to mostly detect *S. ovata*. On the SEM micrographs rod-shaped *S. ovata* is abundantly visible with very few *C. basilensis* cells (fig. 3.4a and b). Additionally, we fixed culture samples at the 24 hour time point after the exponential growth of *C. basilensis*. At this stage, *C. basilensis* cells clearly dominate the landscape (fig. 3.4c and d). *C. basilensis* closely co-exist with inactive *S. ovata* cells, evidently pointing to the fact that *S. ovata* cells are at least innocuous to *C. basilensis* and underscoring the ability to use spent *S. ovata* medium directly with minimal processing.

3.4.4 Bioprocess modeling

To determine process parameters that limit the production rate of PHB, we developed simple models of each step in the bioprocess: H_2-driven acetate production with *S. ovata* and acetate-driven PHB production with *C. basiliensis*. Experimental data of acetogenesis with *S. ovata* was fit well by adjusting the ratio of carbon diverted to acetate or biomass (α) and the gas-liquid mass transfer coefficient (k_La) (fig. 3.5a, b). Because CO_2 solubility (~33 mM/bar) is much greater than H_2 solubility (~0.78 mM/bar), this indicates that H_2 transfer from the gas phase to the liquid phase limits the acetate production rate. Modeled partial pressures in the gas phase (fig. 3.5c) and concentrations in the liquid phase (fig. 3.5d) support this conclusion: daily replenishment of the headspace maintains partial pressures of both substrate gasses at >85% of their initial value. Liquid-phase CO_2 is similarly maintained at >~80% of its initial value. However, H_2 is nearly completely consumed in the liquid phase within ~24 hrs and the concentration does not recover as the gas headspace is replenished, indicating that microbial growth and acetate production consumes H_2 nearly immediately as it is transferred into the liquid phase.

Experimental PHB production is similarly fit well to a simple Monod-like model of biomass growth and PHB accumulation (fig. 3.6a-c). Because specific biomass and PHB accumulation rates are determinant of the PHB production and acetate consumption rates, and acetate consumption is complete within ~24 hrs, this portion of the integrated biomass does not limit overall productivity. Hence, H_2 gas-liquid mass transfer is the central bottleneck in the full process.

3.4.5 Advantages of minimal processing between bioprocesses

Previous works have described the production of acetate from CO_2 by *S. ovata* and the production of PHB by closely related *Cupriavidus* strains from acetate.[151,152] The traditional manufacturing approach to linking two such processes would be to purify the acetate intermediate between synthesis steps. This process is costly in the terrestrial industry and that cost would be prohibitively magnified in the context of space travel. Here, we have demonstrated the viability of serial biocatalyst culturing in a single media batch without processing of intermediate compounds.

Toward this goal, we sought to formulate a minimal media that would support growth of both bacterial strains. It was determined that DM9 medium was suited for this task as it was already the preferred medium for *C. basilensis* growth and we observed only a minimal reduction of productivity for *S. ovata* when grown in DM9 compared to the traditional media for this strain. DM9 is an excellent media for space applications due to its extremely simple composition. The media as used here is primarily composed of phosphate buffer which serves to maintain a stable pH throughout bacterial growth. While pH regulation through buffering is common practice for bench-scale, batch reactors, it is highly uncommon and inefficient for large scale industrial settings. The alternative is continuous pH monitoring of the reaction and automated adjustment as needed with concentrated acids and/or bases.[153] Therefore, our process in an industrial or space setting would require even fewer components.

Another component of the DM9 medium is the ammonium salt used as a nitrogen source for both strains. Fixed nitrogen could potentially be sourced from the Martian atmosphere as a nitrogen source is likely still required for *S. ovata* growth.[50] However, it could also likely be favorable to reduce the nitrogen available to *C. basilensis*. It has been shown elsewhere that nutrient starvation,

and especially nitrogen, is key to triggering the PHB accumulation mechanisms in *C. basilensis* strains.[149] Therefore, sequestering a high density of active, PHB-poor cells into a nitrogen limited environment might improve the productivity and carbon-flux from acetate to PHB substantially.

3.4.6 Identification of process bottleneck

We produced bio-acetate to a final concentration of ~42mM over the course of 14 days. By modelling this process, we can predict that the rate limiting step of acetogenesis is the gas to liquid transfer rate of H_2. As this experiment was only performed in shaken balch-type cell cultures bottles with pressurized headspace, there is significant opportunity for operational optimization to increase the gas-to-liquid transfer of H_2 from the headspace and thus the k_La value representing this process. Such improvements may include agitation of the gas-liquid interface by stirring or bubbling. If the k_La was increased even modestly to a value of 10, the time required to produce the equivalent mass of acetate would decrease by 75% (supplementary discussion 3.1). Productivity in this stage of the process could be at least doubled in a flow-through, chemostat reactor setting, as opposed to batch, in which bio-acetate laden media is removed continually as it is diluted with fresh media. This approach increases efficiency by keeping the active cell number high and decreasing the need for a time-consuming lag phase in cell growth (supplementary discussion 3.1).

Next, the spent medium containing 42mM acetate was diluted down to a final concentration of 25mM acetate. The aeration of the medium at this step was done as a precaution against oxygen limiting conditions but optimization at this phase could prove this unnecessary, especially with the nearly two-fold dilution of the medium in presumably-oxygenated fresh liquid. This minimal processing is the key operational cost reduction uncovered by this study.

It was demonstrated clearly that acetate is consumed proportionally to the PHB produced as it is presumed to be the only available carbon source for *C. basilensis*. This assumption is further enforced by the degradation of PHB which occurs after the acetate has been exhausted. In a biomanufacturing setting, acetate levels would need to be monitored so that the PHB could be harvested before it was repurposed as a fuel for biomass accumulation.

3.4.7 Process consideration for space biomanufacturing

The productivity of *C. basilensis* in this study of 12.54 mg PHB L^{-1} hr^{-1} falls below demand of 1.55 g PHB L^{-1} hr^{-1} required for 3D printing an extraterrestrial habitat structure of 12 m^3 within a reasonable time frame.[154] In this demonstration experiment, optimization was not undertaken to improve this metric. The maximal PHB production rate of *Cupriavidus* species when grown in optimized conditions has been reported as high as 1.85 g L^{-1} hr^{-1} .[155] We hypothesize that, with additional strain and process optimization, productivity values for our media recycling approach should far exceed its present performance.[152,156,157]

Removal of the intermediate purification step between acetate production and PHB production offers both decreased system mass requirements and increased operational simplicity. Purification of acetate from aqueous solution is a delicate and energy intensive task most often performed either by expensive column separation or liquid-liquid extraction followed by distillation. These conventional industrial approaches would prove inefficient and inflexible for continued operation in the context of space travel and may increase the system mass of biological PHB production

above the threshold mass of simply bringing pre-made PHB. The method presented here allows for nearly "straight-pipe" integration of the bioprocesses and considerably decreases the complexity of this system.

Even with an increased productivity to 0.04 g PHB L^{-1} hr^{-1}, the mass of media components required for generation of 1 kg of PHB would exceed that of simply bringing 1 kg of PHB from Earth. It was estimated that with our current media formulation, 12 kg of media components (primarily phosphate buffer) would be required to produce 1 kg PHB in one day (supplementary table 3.4). However, without the straight spent media utilization as presented, the process would require either a distillation column or nearly 1 ton of ethyl acetate for liquid extraction, assuming 1:1 solvent to media extraction. Altogether, our process affords nearly 98% weight savings as compared to a process involving liquid extraction of acetate. An attractive and thematically aligned approach would be subsequent reuse of media batches for further rounds of acetate and PHB production. While this method was not tested here, studies which determine the rate of nutrient depletion of the media so that it may be supplemented or assigned a maximum life cycle could decrease mass requirements for media significantly. An additional benefit of ISRU as it pertains to producing biopolymer for additive manufacturing is that astronauts would be able to alter the material on demand. A PHA with different material properties could be produced instead of relying on further deployments of goods to fulfill a pressing need.

In all, we have presented an approach for serial biomanufacturing with limited intermediate purification and processing steps. This streamlined approach reduces the need for costly materials that would need to be transported into space in order to support a biomanufacturing facility. Further optimizations of each biocatalyst step should be undertaken to maximize the cost-savings benefit of this process for production of PHB from CO_2. Lastly, there are additionally considerations for microbial production of chemicals and materials in space that are currently under investigation including the effect of cosmic radiation on single-cell organisms, the effect of low gravity environments on CO_2 conversion and *in situ* resource utilization of Martian water for electrochemical processes.

3.5 Figures

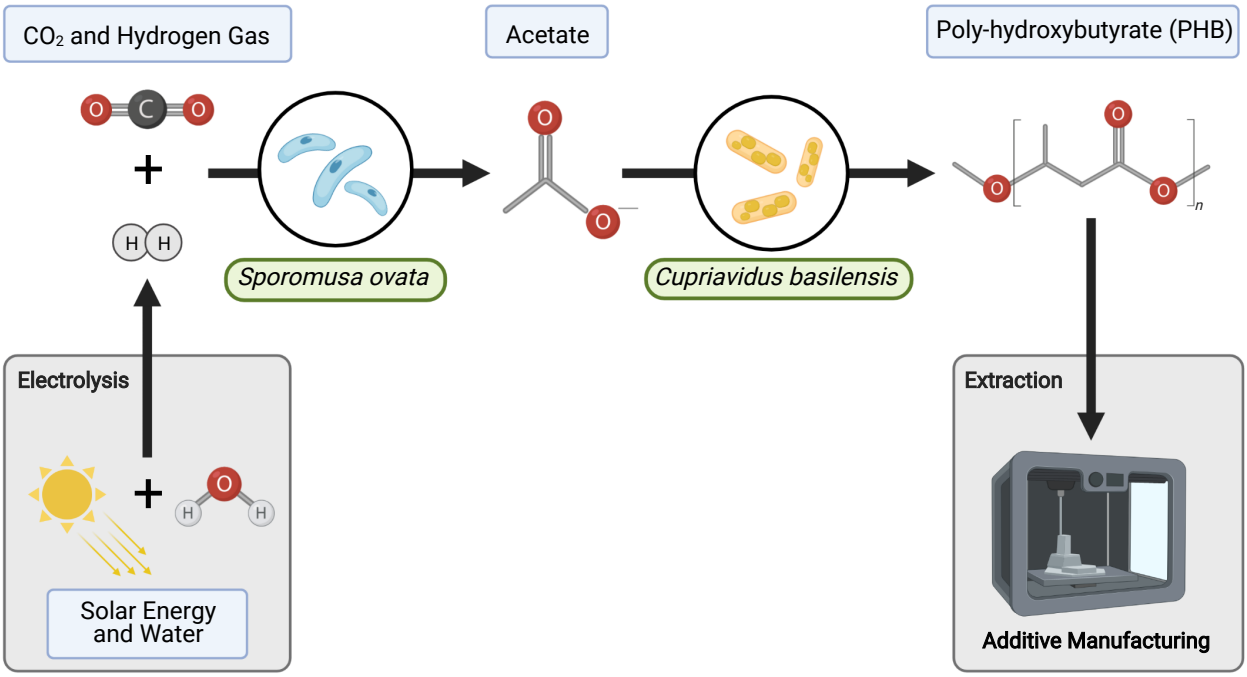


Figure 3.1. Process diagram for two-stage bioprocess with media recycle. *Sporomusa ovata* oxidizes H_2 to fix CO_2 into acetate. *C. basilensis* grown in the unprocessed spent medium converts acetate to PHB. Modules to be tested for end-to-end biomanufacturing including H_2O reduction and PHB extraction to 3D printing in grey.

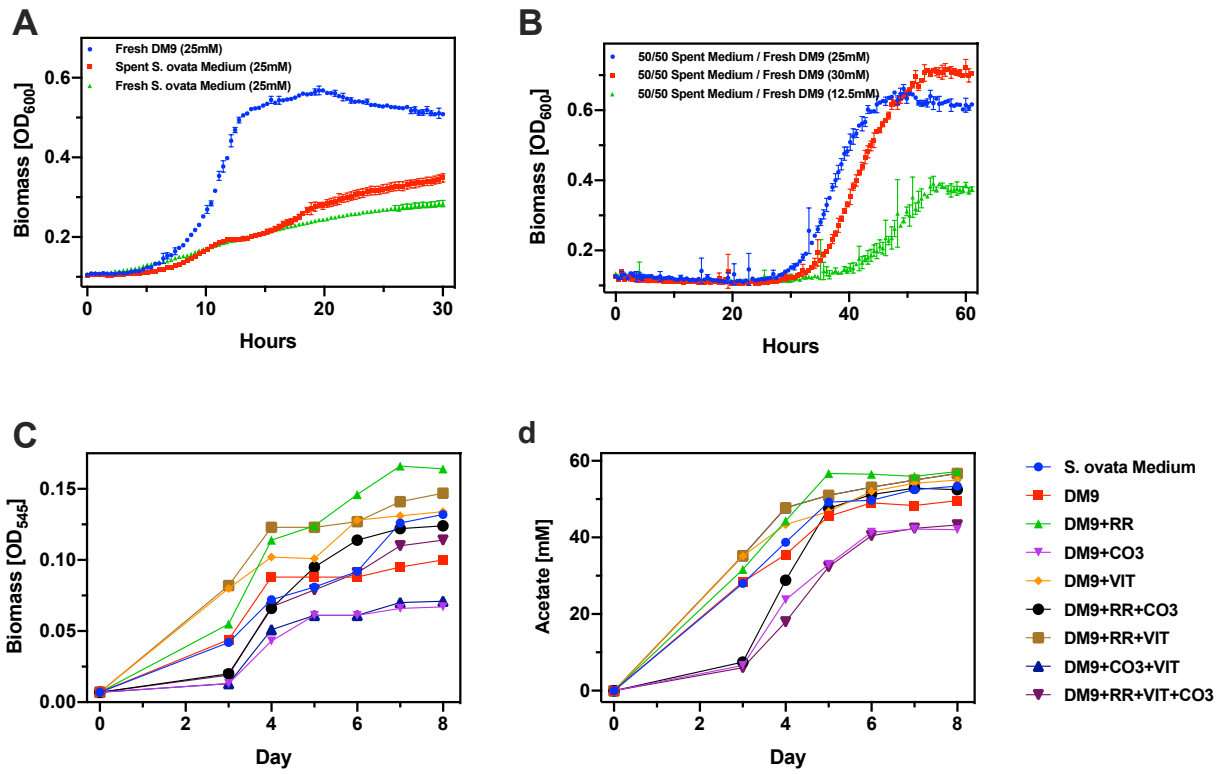


Figure 3.2 Optimization of media compatibility (A) Biomass yield of *C. basilensis* in DM9, and in spent and fresh *S. ovata* medium. (B) Biomass yield of *C. basilensis* in spent *S. ovata* medium diluted with fresh DM9 to a range of acetate concentrations. (C) Biomass and (D) acetate yield of *S. ovata* in DM9 with additional components (RR reducing reagent; VIT vitamins; CO_3 sodium carbonate) compared to those in S. ovata medium.

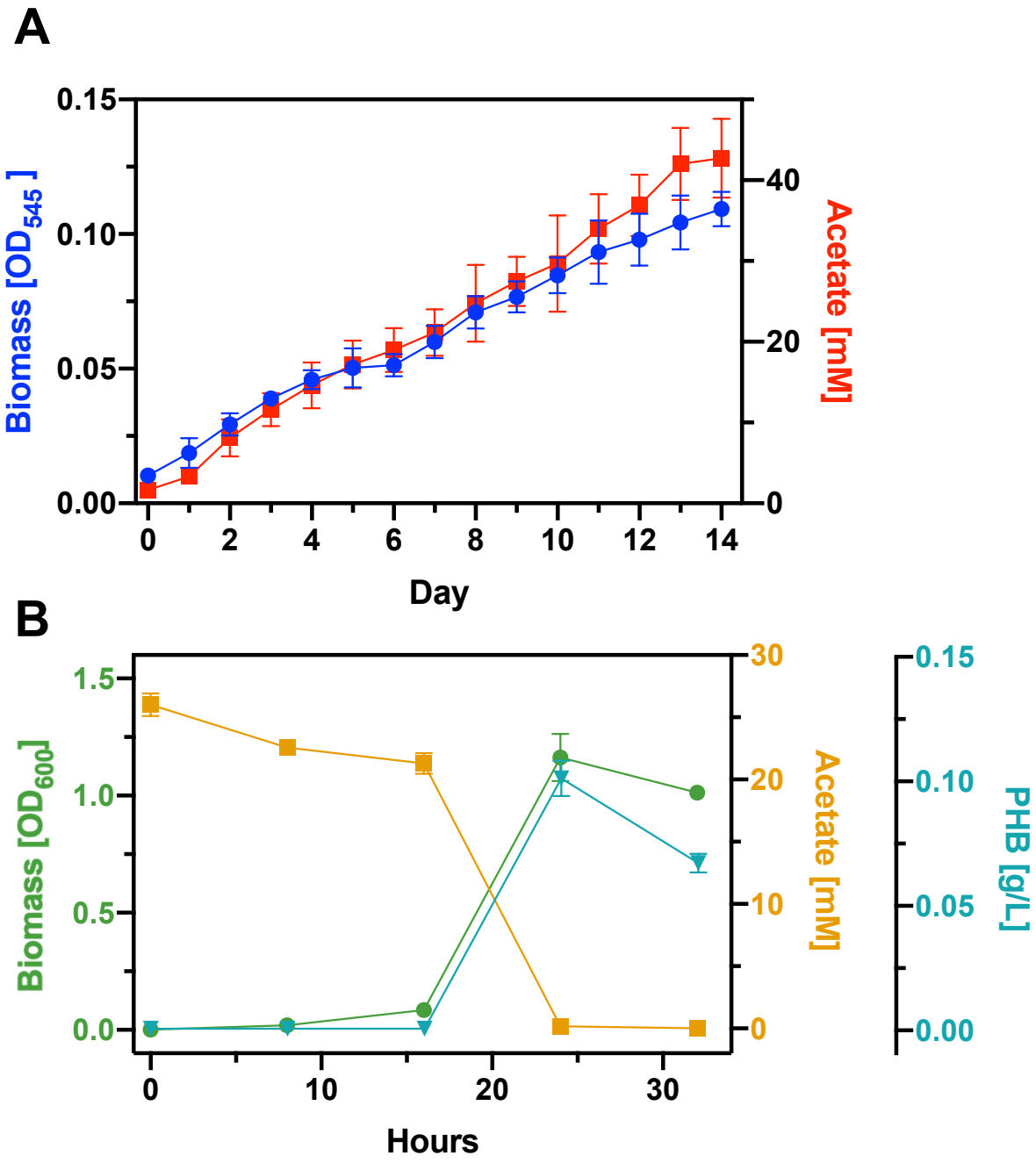


Figure 3.3 Full bioprocess integration. (A) Cell growth and acetate generation by *S. ovata* in DM9 (B) Biomass yield, acetate consumption, and PHB accumulation by *C. basilensis* acetate rich spent DM9.

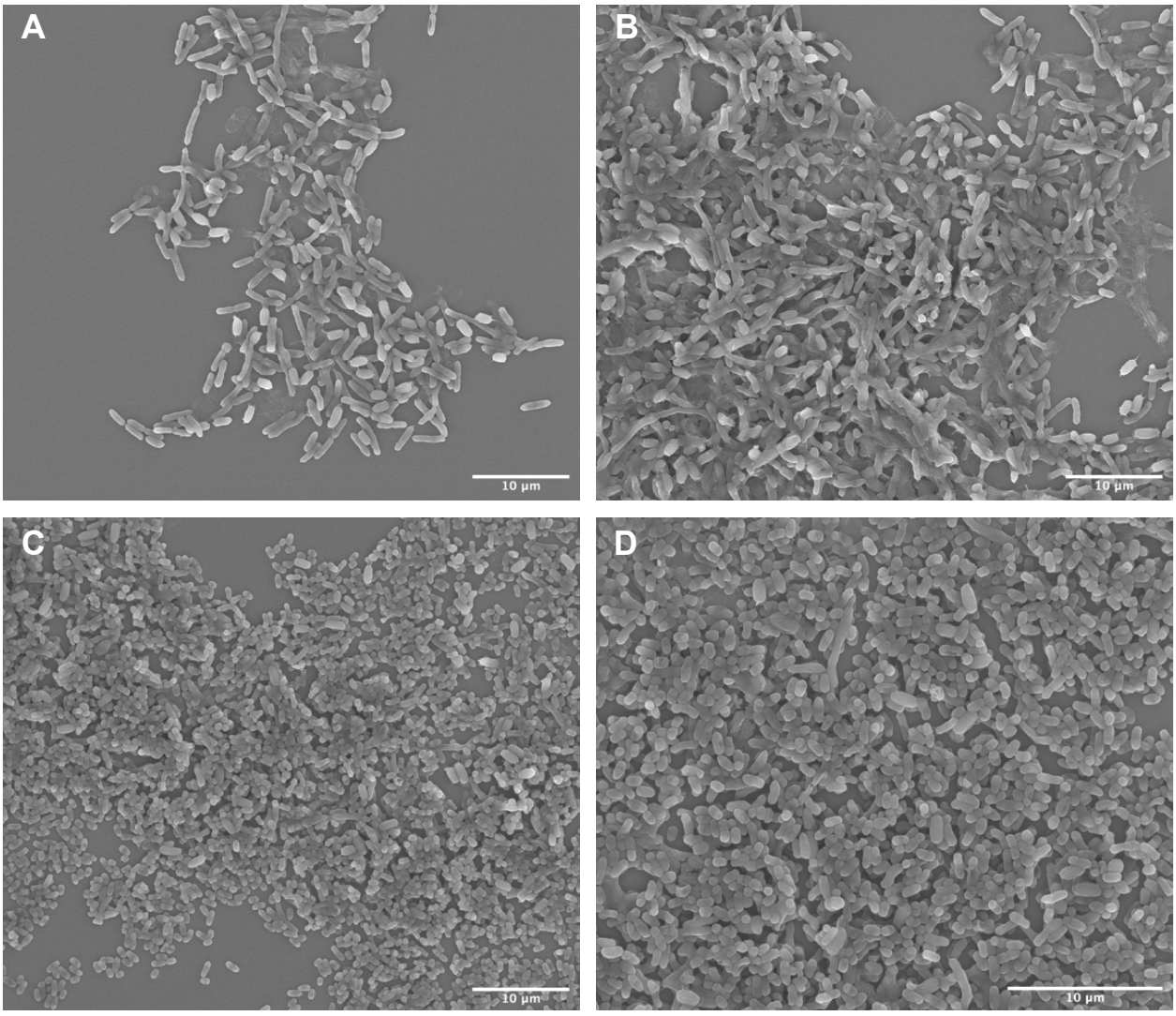


Figure 3.4 Scanning electron micrographs of bioprocess. (A) and (B) 0 hour time point post *C. basilensis* inoculation in *S. ovata* containing spent DM9. (D) and (C) 24 hour time point after *C. basilensis* exponential growth.

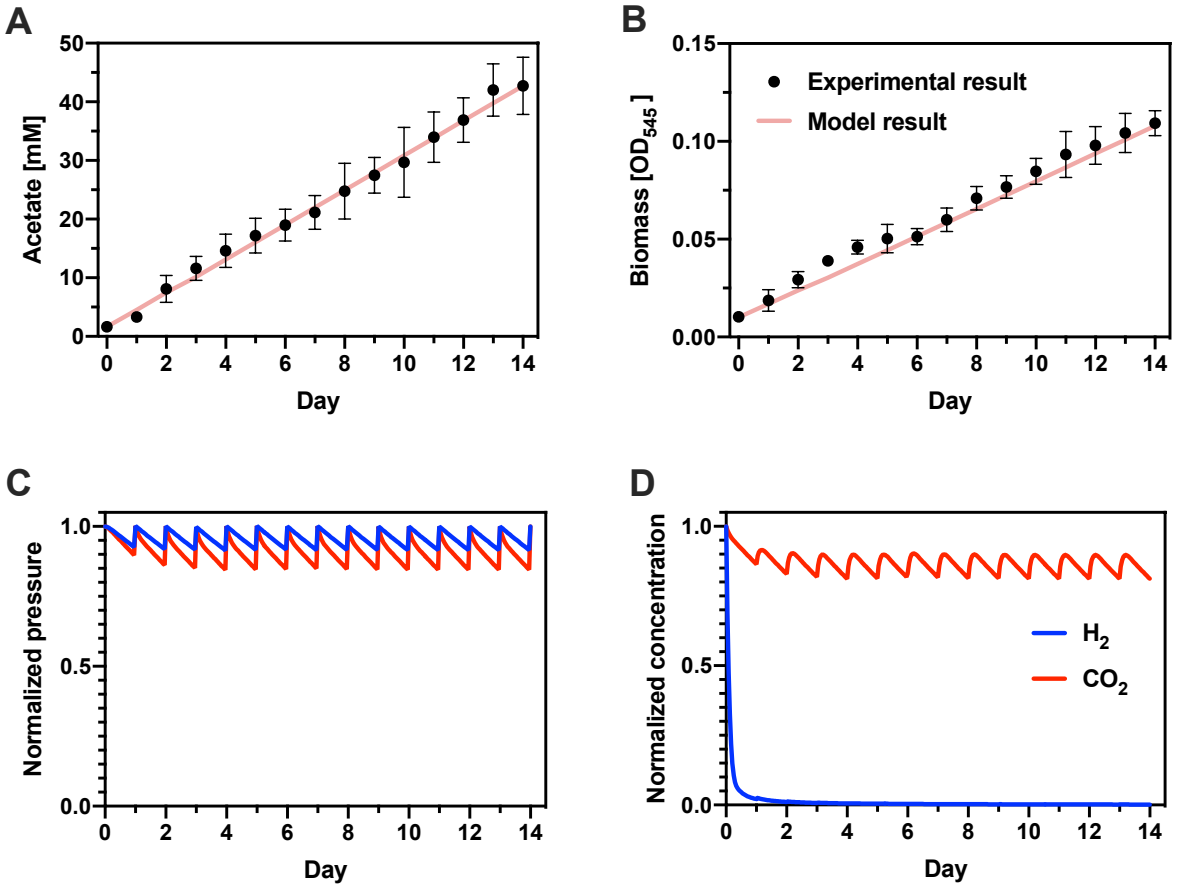


Figure 3.5 Acetogenesis model. Comparison of experimental data and modeling results for (A) acetate and (B) biomass accumulation. (C) Calculated normalized H_2 and CO_2 partial pressures in the headspace of the bioreactor. (D) Calculated normalized dissolved concentrations of H_2 and CO_2 in the liquid phase of the acetogenesis bioreactor.

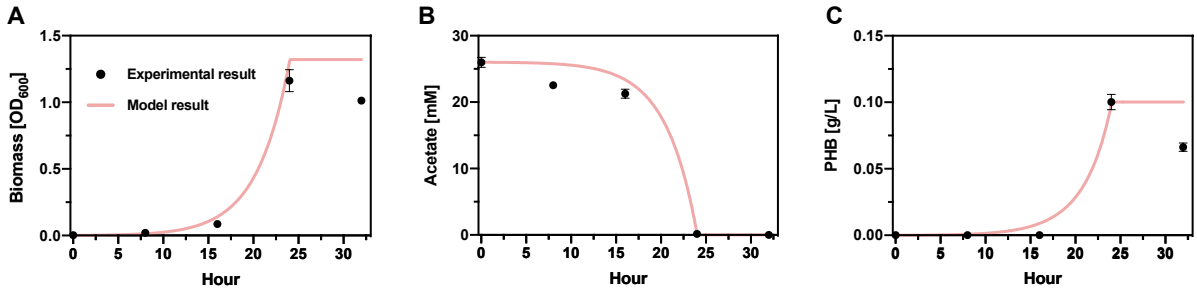


Figure 3.6 *C. basilensis* bioreactor model. Comparison of experimental and model results for (A) biomass yield, (B) acetate consumption and (C) PHB accumulation.

Chapter 4: Biohybrid co-culture for tandem and tunable CO_2 and N_2 fixation

Reproduced in part with permission of collaborators:
Cestellos-Blanco, S., Chan, R.R., Shen, Y.-X., Kim, J.M., Tacken, T.A., Ledbetter, R., Yu, S., Seefeldt, L.C., Yang, P.

4.1 Preface

The previous chapter laid out a staged approach to upgrade the acetate obtained from CO_2 to a value-added bioplastic. This chapter demonstrates that two bacterial species can be co-cultured synergistically in a single bioreactor to cut down on processing steps. The primary autotroph is *Sporomusa ovata* (*S. ovata*) which obtains reducing equivalents either from H_2 or from electricity to convert CO_2 to acetate. The secreted acetate is consumed by a N_2-fixing photoheterotroph in *Rhodopseudomonas palustris* (*R. palustris*) to fuel cell functions. We identified an *R. palustris* mutant that expresses nitrogenase constitutively and thus secretes free NH_3. The free NH_3 either feeds *S. ovata* or can be sequestered. Thus, we created a co-culture that an subside on CO_2 and N_2 and a source of reducing equivalents. Furthermore, we found that by altering the co-culture conditions we could manipulate the product stream of either acetate, free NH_3, nitrogenous biomass or a bioplastic. *R. palustris* has versatile metabolic modes and can be further engineered to produce a variety of carbon products. For this reason, we envision that this co-culture approach could provide a suite of value-added products on demand from CO_2 and N_2.

4.2 Introduction

Society at large has benefitted from industrial chemical processes that rely heavily on hydrocarbon fossil fuels as both a source of energy and a feedstock. For example, steam methane reforming from natural gas is a key step to produce syngas consequently reacted with N_2 during the Haber-Bosch process to produce NH_3 commonly used as a fertilizer.[158] However, as complications of exploiting nonrenewable hydrocarbon fuels exemplified by climate change and environmental pollution become more salient, we are pressed to find renewable alternatives that also close the carbon cycle by utilizing CO_2.[159] Efforts to reduce CO_2 through biological and electrochemical means are flourishing in both academia and industry.[15,160,161] Microbial electrosynthesis in particular marries the advantages of electrochemistry and biology by electrifying microbial "living" catalysts to form chemicals from CO_2, N_2 and H_2O building blocks.[31,162] Microbes offer high product selectivity, low substrate activation barriers, and self-construction and regeneration.[163] Meanwhile, electrochemistry often involves modular and light activated nanocatalysts and can be easily powered by renewable solar energy.[12,164] Photosynthetic biohybrid systems (PBS) driven by solar energy represent a promising strategy for sustainable chemical production.[1]

Autotrophic bacteria, commonly *Sporomusa ovata* (*S. ovata*), accept reducing equivalents in the form of hydrogen or electrons from a poised cathode in an electrochemical cell.[140] *S. ovata* in particular routinely converts CO_2 to acetate with over 80% faradaic efficiency using photo- and electrochemical reducing equivalents.[36] Advances of this concept have broadly been achieved through genetic engineering[87,165], adaptation of biocatalysts[41] and refinement of the

electrochemical environment to increase biocompatibility.[77] Our group previously established a solar-driven Si nanowire platform that allows for high loading capacity of *S. ovata*.[89] When close-packed with *S. ovata*, this platform enables a current density of 0.65 mA/cm^2 and a solar-to-chemical conversion efficiency of 3.6%.[77] Despite steady improvements, the rate of CO_2-to-acetate bioelectrosynthesis still lags behind those achieved by purely inorganic metal-based electrocatalysts by an order of magnitude due in part to the sluggish autotrophic metabolism of CO_2-fixing bacteria.[166,167] Therefore, we must emphasize and build upon inherent advantages of the biocatalyst-based system, i.e. its high product selectivity and low substrate activation barrier, in order to continue moving the field forward in an impactful manner.

Long-term stability is customarily achieved by bioelectrosynthetic systems, which is particularly critical when their products are required as feedstocks for downstream processes. Their durability also facilitates productive long-term solar-to-chemical conversion.[77] Furthermore, another pivotal advantage lies in the ability of microorganisms to produce higher value carbon products through tandem biocatalysis. Liu *et al*. used acetate from a PBS as a feedstock for genetically engineered *Escherichia coli* (*E. coli*) to produce biofuels, a bioplastic and a pharmaceutical that are not attainable via inorganic CO_2 electrocatalysis.[89] Their research establishes acetate as an upgradeable carbon intermediate that can be easily passed on to a second more specialized biocatalyst. The concept of using a bacterial community for tandem biocatalysis has been advanced to expand the suite of CO_2 carbon products[109,168–170], to enhance CO_2 fixation rates[42,171] and even to increase the rate of current production in electrogenesis.[172] Altogether, the co-culturing of bacterial catalysts has centered on CO_2 fixation and carbon-based upgrading. As a progression, we hypothesize that: 1) acetate can not only be used as an upgradeable carbon intermediate but also as an energy-rich substrate to power N_2 biocatalysis, and 2) that we can exercise electrochemical control on a bacterial co-culture.

Industrial N_2 fixation occurs primarily through the Haber-Bosch process to produce NH_3, commonly used as fertilizer to match the agricultural needs of an expanding global population. Ammonia has also been proposed as a carbon free energy-carrier that is less volatile than H_2.[173] However, the Haber-Bosch process accounts for 1% of the world's energy use, releases harmful greenhouse gases and pollutes the local environment.[158] Additionally, transporting ammonia products from a centralized plant adds cost and generates carbon emissions particularly to unindustrialized locales.[174] N_2 electrocatalysis attempts to overcome the aforementioned issues by electrochemically reducing N_2 to NH_3 mediated by inorganic nanostructured catalysts to be powered with renewably solar energy at a decentralized scale.[175] While significant strides have recently been reported,[176,177] these efforts are hampered by the non-specificity of catalysts as evidenced by competing H_2 evolution,[178] low overall yields,[179] short durability,[180] and complicated nanocatalyst synthesis often with precious metals.[181,182]

To overcome some of these challenges, diazotrophic whole-cell bacteria have been harnessed for bioelectrochemical N_2 fixation.[50,125] More recent advances detail the tuning of the O_2 microenvironment to enhance bioelectrochemical N_2 fixation by a perfluorocarbon nanoemulsion or through a silicon-based microwire array. [183,184] Additionally, Dong *et al.* reported an engineered cyanobacterium that directly uptakes electrons from a cathode for N_2 to NH_3 conversion.[185] Nevertheless, certain obstacles may still hinder the efficiency and productivity of bioelectrochemical N_2 fixation: N_2 fixation is paired with sluggish autotrophic metabolism in a single bacterial species which limits the rate of nitrogen fixation and any generated ammonia is immediately consumed by the bacteria, resulting in nitrogenous cell biomass whose refinement is non-trivial if the desired product is ammonia. Furthermore, bioelectrochemical N_2 fixation systems

employing single bacterial species commonly employ evolved H_2 as a charge mediator, but H_2 has been reported to attenuate nitrogenase activity.[186,187]

We surmounted these challenges by co-culturing of individual, specialized CO_2- and N_2-fixing microorganisms. We identified *Rhodopseudomonas palustris* (*R. palustris*), a purple non-sulfur bacterium capable of engaging versatile metabolic modes.[188] *R. palustris* rapidly proliferated diazotrophically using acetate provided by *S. ovata* while also producing poly(3-hydroxybutyrate) (PHB), a biopolymer directly employed in additive manufacturing.[136] Furthermore, we employed a mutant strain of *R. palustris* which constitutively expressed nitrogenase through a manipulation of the NifA protein responsible for transcriptional regulation of nitrogenase genes. This modification allowed for extracellular secretion of ammonia and higher resistance to H_2 nitrogenase inhibition. We establish that *S. ovata* and *R. palustris nif*A* can be co-cultured synergistically to form a robust consortium incubated for longer than one month. The co-culture products and dynamics were directed by the substrate gas composition. Furthermore, we employed our model silicon nanowire (SiNW) platform to provide *S. ovata* with reducing equivalents for the reduction of CO_2 to acetate. Subsequent introduction of *R. palustris nif*A* to our electrochemical biohybrid system enabled N_2 fixation to ammonia and nitrogenous biomass concurrently. Additionally, *R. palustris nif*A* was able to produce PHB from acetate. Finally, our design can be fully sustained with solar energy establishing a photosynthetic biohybrid system converting H_2O, CO_2 and N_2 renewably in tandem to value-added products.

4.3 Materials and Methods

4.3.1 Cell culture

Balch-type anaerobic culture tubes with butyl stoppers were employed to separate the culture from the environment and maintain desired headspace pressure. A COY vinyl anaerobic chamber was used to conduct experiments anaerobically. *S. ovata* was purchased from the American Type Culture Collection (ATCC 35899) and rehydrated as indicated. It was then grown in betaine medium and aliquoted with DMSO as a cryoprotectant to be stored at -80°C. Frozen cells were revived in betaine medium and cultured for two cycles before inoculating in yeast medium. *S. ovata* from yeast medium were inoculated at 5% (v/v) in autotrophic medium with H_2/CO_2 80/20% headspace at 175kPA. *S. ovata* was incubated at 35 °C in starting pH 7.2 Frozen stocks of *R. palustris* strains TIE-1[189] and *nif*A* as prepared in Mckinlay *et al*.[190] provided by the Harwood group were inoculated in PM medium supplemented with 20mM acetate for two cycles. The cells were washed 3 times anaerobically before inoculating in diazotrophic photoheterotrophic medium (N_2 100% headspace) or diazotrophic autotrophic medium ($H_2/CO_2/N_2$ 40/20/40% headspace). *R. palustris* was incubated at 30 °C in starting pH 6.8 with a 20W CFL light bulb. *S. ovata / R. palustris* co-cultures were cultivated in co-culture medium. *S. ovata* was typically inoculated first from an autotrophic culture after 3 anaerobic washes to remove nitrogen. *R. palustris* was added thereafter also after 3 anaerobic washes. The co-culture was maintained at 30 °C with a 20W CFL light bulb with headspace as indicated in the experiment.

4.3.2 Analysis of acetate, ammonia, total nitrogen and hydrogen

Acetate concentration was assessed by ^{1}H-qNMR spectroscopy (Bruker 400MHz) with sodium 3-(trimethylsilyl)-2,2',3,3'-tetradeuteropropionate as the internal standard. ^{13}C-labeled experiment was conducted as previously reported.[89] Ammonia was determined by the o-Phthalaldehyde (OPA) method as previously reported with slight modifcations.[191] 100 mg OPA was dissolved in 3.125mL pure ethanol. 50mL 0.2M sodium tetraborate buffer was prepared with 1.3mM sodium sulfite. The two solutions were mixed quickly avoiding light exposure. These reagents were prepared fresh before experiments. Cell culture samples were ultracentrifuged and filtered in order to separate the cell material from the supernatant. The supernatant and reagent solution were combined in 1:10 ratio and assayed with a fluorescence equipped plate reader (SpectraMax i3x, λ_{ex}=410nm λ_{em}=470nm). Ammonia was also routinely verified with a commercial testing kit (HACH TNT830) as per the manufacturer's instruction. Ammonia and ^{15}N-labeled experiments were assayed by ^{1}H-qNMR spectroscopy (Bruker 500MHz) with water suppression. Cell culture media was degassed with Ar and the cell culture vessel headspace was evacuated after sealing under Ar atmosphere. Total fixed nitrogen was determined as per a previous report[50] using a commercial persulfate nitrogen digestion kit (Hach Company 2672245). The samples were ultracentrifuged to separate the supernatant from the cell material. The cell material was washed before using the nitrogen digestion kit. Total nitrogen as a function of optical density calibration curves were established spectrophotometrically for each experimental set. Hydrogen production in diazotrophic cultures was quantified by gas chromatography after 24 hours (Agilent 7890B GC system). PHB content was quantified as per Wang *et al.*[192] First cell PHB content was hydrolyzed with NaOH under heating and then a β-Hydroxybutyrate Assay Kit (Sigma Aldrich MAK041) was used for spectrophotometric quantification.

4.3.3 Electrochemical and solar-driven experiments

p^+ Si nanowire array electrodes were prepared as previously described.[77] Briefly, the Si nanowire arrays were etched from 6-inch p^+-Si (boron) wafers (ρ ~0.001-0.005 Ω. cm) after patterning with a photoresist dot array using a standard photolithography stepper. They were then coated with 5 nm of TiO_2 as a protective layer by atomic layer deposition (Picosun ALD). Finally, they were sputtered with ~10 nm nickel (Edwards Inc.). The Si nanowire wafer was cut to 2.25cm^2 pieces and placed on a Ti foil with Ga-In eutectic, silver glue and carbon tape to maintain electrical contact. A water-resistant rubber resin (Gardner Bender) was used to seal the backside and sides of the Si electrode. A homemade closed chamber H-cell type electrochemical cell equipped with mechanical clamps to maintain pressure was filled with 160mL of co-culture electrolyte (80mL in each cathodic and anodic chambers) and a 175 kPa CO_2/N_2 headspace. Fresh Nafion 117 membranes were pretreated with 5% H_2O_2 and rinsed with ultrapure water directly before each experiment. The H-cell was sonicated in dilute HCl to sterilize. *S. ovata* was cultured in autotrophic medium with a H_2/CO_2 headspace and 36 hours prior to the electrochemical experiment the headspace was exchanged to CO_2/N_2. Typically, electrochemical bias was started 24 hours before introducing *S. ovata* to the H-cell with a Ag/AgCl (1M KCl) reference and Pt wire as a counter and conducted with Gamry Interface 1000 potentiostats. The *S. ovata* in autotrophic medium was washed 3 times and introduced into the cathodic chamber. The electrochemical bias (typically -0.29V vs. RHE, medium pH 6.8). was maintained until a specified amount of charge was passed. Afterward, 3 time washed *R. palustris nif*A* was inoculated into the cathodic chamber. For the solar-driven experiments, a two-electrode configuration was used as per previous experiments, where the silicon nanowire electrode served as the cathode and the Pt wire served as the anode.[77] A commercial single-crystalline 0.96cm^2 Si solar cell (KXOB22-01X8F) was purchased from

Digi-key Corporation and a 300W Xenon arc lamp (Newport Corporation) with an AM1.5G filter was used for illumination. A Si photodiode referenced to an NREL calibrated photodiode was employed to calibrate the light intensity to 25 mW/cm^2. Samples were evaluated for acetate, ammonia, total nitrogen in biomass and PHB as described.

$FE_{acetate}$ was calculated based on the following equation:

$$FE_{acetate} = \frac{96485\ \frac{C}{mol} \times 8\ (e^-) \times \text{moles}}{\text{charge passed (C)}} \times 100\%$$

And the specific CO_2-reducing current density (per electrode area) $J_{acetate}$ is defined as: $J_{acetate} = FE_{acetate} \times J_{total}$ where J_{total} is the average stabilized current during chronoamperometry.

$FE_{nitrogen\ in\ biomass}$ and $FE_{nitrogen\ in\ biomass}$were calculated based on the following equations (assuming no H_2 recycling as *R. palustris nif*A* is incapable of metabolizing H_2).

$$FE_{nitrogen\ in\ biomass} = \frac{96485\ \frac{C}{mol} \times 4\ (e^-) \times [N_{final}\frac{g}{L} - N_{initial}\frac{g}{L}] \times \text{V(L)}}{14\frac{g}{mol} \times \text{charge passed (C)}} \times 100\%$$

And the specific N_2-reducing current density (per electrode area) $J_{nitrogen\ in\ biomass}$ is defined as: $J_{nitrogen\ in\ biomass} = FE_{nitrogen\ in\ biomass} \times J_{total}$

$$FE_{ammonia} = \frac{96485\ \frac{C}{mol} \times 4\ (e^-) \times \text{moles}}{\text{charge passed (C)}} \times 100\%$$

And the specific N_2-reducing current density (per electrode area) $J_{ammonia}$ is defined as: $J_{ammonia} = FE_{ammonia} \times J_{total}$

Total solar-to-chemical efficiencies were calculated as follows for C and N products, where 1.09V and 1.14V are the respective thermodynamic potentials needed to microbially reduce CO_2 and N_2 to acetate and ammonia.[50,89,193]

$$\eta_{acetate} = \frac{1.09\text{V} \times J_{acetate}\ \frac{mA}{cm^2}\ \times\ A_{electrode}\ cm^2}{\text{I}\ \frac{mW}{cm^2} \times A_{solar\ cell}\ cm^2} \times 100\%$$

$$\eta_N = \frac{1.14\text{V} \times J_N \frac{mA}{cm^2} \times A_{electrode}\, cm^2}{\text{I}\, \frac{mW}{cm^2} \times A_{solar\ cell}\, cm^2} \times 100\%$$

4.3.4 SEM characterization

Bacterial cultures were supplemented with glutaraldehyde at 2.5% (v/v) and kept at room temperature overnight. The cells embedded in the silicon nanowire substrates were washed and consecutively dehydrated with 10% 25% 50% 75% 90% and 100% ethanol each for 10 minutes. The ensembles were immersed in hexamethyldisilazide (HMDS) for 2 hours and thereafter allowed to dry overnight. The ensembles were cut in half, sputtered with gold (Denton Vacuum, LLC) and finally imaged at 5 keV/12 μA by field emission SEM (JEOL FSM6430).

4.4 Results and Discussion

In nature, a symbiosis exists between legume plants and nitrogen-fixing Rhizobia (fig. 4.1a).[194] Legumes provide an anerobic microenvironment in their root nodules and supply rhizobia with organics such as malate.[195] Rhizobia metabolize the organic substrates and in turn fix sufficient N_2 for themselves and the host plant. Taking inspiration from nature, we identified the bacterium *R. palustris* capable of assimilating acetate to fuel cell functions including N_2 fixation.[196] As demonstrated in supplemental figure 4.1, *R. palustris* initiates acetate metabolism by activating acetate to acetyl-CoA which feeds into the tricarboxylic acid (TCA) cycle with a glyoxylate shunt. Acetyl-CoA is combined with oxaloacetate to form citrate. After recombining citrate to isocitrate, it is divided into succinate and glyoxylate. Succinate is oxidized to malate yielding ubiquinol while glyoxylate is joined with acetyl-CoA to form malate. Malate is then oxidized to oxaloacetate generating NADH and ubiquinol. Oxaloacetate is either incorporated back into the TCA cycle or decarboxylated to phosphoenolpyruvate to be used in biosynthesis. Nitrogenase-mediated N_2 reduction not only provides necessary ammonia but is also an important metabolic electron sink in *R. palustris* aiding to oxidize the redox molecular shuttles generated through the TCA cycle.[197] Therefore, acetate is directly responsible for providing reductive energy to nitrogenase. Concurrently, *R. palustris* could also condense two acetyl-CoA molecules to hydroxybutyryl-CoA, the monomer for PHB.

As a result of the adept acetate metabolism in *R. palustris*, we posit that we could integrate *R. palustris* into our SiNW – *S. ovata* biohybrid system thus mimicking the plant/bacteria symbiosis fixing both CO_2 and N_2 to value-added products (fig. 4.1b). Overall, (photo)electrochemical reducing equivalents power *S. ovata* mediated CO_2 to acetate conversion; this acetate is then consumed by *R. palustris* to enable N_2 fixation for both bacteria and PHB production.

4.4.1 Characterization of individual S. ovata and R. palustris nifA* cultures

Before combining *S. ovata* and *R. palustris*, we characterized each strain's growth and product outputs in separate cultures. We inoculated *S. ovata* in autotrophic medium (pH 6.8, 35 °C) at three sequential starting optical densities, I (starting OD_{545} of 0.15), II (starting OD_{545} of 0.225) and III (starting OD_{545} of 0.6) with a H_2/CO_2 headspace (fig. 4.2a). Over the first 24 hours, III reached an acetate concentration of 34 mM while I and II reached 25 mM and 15 mM respectively (fig. 4.2b). These results indicated that over the first day acetate production was proportional to culture density. All cultures achieved a similar acetate concentration on the second day (~52 mM) and a maximum of ~60 mM on the third day regardless of optical density. At this point the pH of the cultures was 5.2, which is lower than the optimal pH range for *S. ovata* (fig. S4.2).[102] The production of acetate presented a self-inhibitive problem: the accumulated acetate became toxic to cells as it acidified the pH of the media to an intolerable level. Each culture set grew by OD_{545} ~0.2 and the stationary stage coincided with media acidification indicating that metabolic activity is paused in a low pH environment. Therefore, a mechanism for acetate sequestration could maintain a neutral pH and thus enable sustained growth and metabolic activity of *S. ovata* cultures over a longer period.

Next, we characterized the photoheterotrophic growth of the *R. palustris nif*A* mutant under diazotrophic conditions providing synthetic acetate as a carbon substrate with a pure N_2 headspace. As previously noted, *R. palustris nif*A* expresses nitrogenase genes constitutively. This is a result of a mutation in the Q-linker region between the NifA N-terminal GAF and AAA^+ domains.[197] The *R. palustris nif*A* mutant was first identified by Rey *et al*. following adaptative evolution to isolate *R. palustris* mutants with enhanced biohydrogen production, as H_2 is produced obligatorily along with NH_3 by nitrogenase.[198] Importantly, the *R. palustris nif*A* mutant does not metabolize H_2 which prevents any competition with *S. ovata* for H_2.[199] Secretion of NH_3 into the culture medium by *R. palustris nif*A* under N_2-fixing conditions has been previously detected.[200] Genetic engineering of the NifA gene has also been undertaken in different N_2-fixing bacteria strains to obtain extracellular NH_3.[201]

We plotted the growth curves of *R. palustris nif*A* under diazotrophic conditions provided with increasing acetate concentrations from 2.5 to 15 mM (fig. 4.2c). The greatest culture density was achieved in the culture with the highest initial acetate concentration; thus, the biomass production was dictated by acetate. As a comparison, we cultured *R. palustris* wild type (WT TIE-1) under diazotrophic and autotrophic conditions ($N_2/CO_2/H_2$).[189] *R. palustris* WT TIE-1 failed to reach a comparable density as the photoheterotrophic cultures within the same experimental timeframe. Afterward, using a Kjeldahl-type nitrogen digestion assay, we were able to quantify the total fixed nitrogen in each culture set (fig. 4.2b,d). The amount of fixed nitrogen directly correlated with the density of each culture; thus, the concentration of acetate prescribed the overall quantity of nitrogen that was fixed. We tracked the acetate concentration in an *R. palustris nif*A* culture and found that the acetate was categorically consumed by the mid-exponential phase (fig. S4.3). Furthermore, we determined that even if the growth of an *R. palustris nif*A* culture plateaus and the initial acetate is completely consumed, we can induce further growth by adding more acetate (fig. S4.4). This establishes that *R. palustris nif*A* culture activity can be extended by continuous addition of acetate.

Finally, we investigated the ability of *R. palustris nif*A* to generate extracellular NH_3. We utilized an established fluorescence-based assay to detect NH_3 coupled with ^{1}H-NMR

confirmation.[191] In order to maximize the amount of NH_3 recovery, we performed a short selection experiment. *R. palustris nif*A* was divided into cultures grown photoheterotrophically under diazotrophic conditions, and the culture with the highest concentration of extracellular NH_3 was re-inoculated successively over at least five generations (fig. S4.5). This boosted the NH_3 recovery by an order of magnitude. We found that the amount of extracellular NH_3 produced by *R. palustris nif*A* was inversely proportional to the initially available acetate, i.e., the cultures with 2.5 mM acetate had the highest concentration of extracellular NH_3 (fig. 4.2e). This observation may be explained by the fact that cultures with higher acetate concentration have access to more carbon for protein biosynthesis through which NH_3 is depleted rapidly. As previously noted, the acetate was fully consumed before the culture reached its maximum optical density, pointing to a metabolic stage during which all the acetate has been converted to carbon intermediates. The amount of NH_3 consumed by protein biosynthesis depends on the abundance of carbon intermediates. Therefore, the amount of extracellularly secreted NH_3 decreases with a larger pool of carbon intermediates which stem from acetate. Nonetheless, more focused study is required to fully elucidate this observation. Favorably, we can conclude that the initial acetate input can be used to direct nitrogen products, either nitrogenous biomass or NH_3. We also conducted an experiment consisting of growing *R. palustris nif*A* under varying N_2 headspace pressures (Fig. S4.6). We confirmed that N_2 pressurization did not have an outsize effect on cell concentration below 175 kPa. The cell concentration at 200 kPa was slightly increased, though experiments at higher pressures could not be safely conducted. The concentration of extracellular NH_3 demonstrated an increasing trend up to 175 kPa. Moreover, we noted H_2 co-production (247±26 ppm) in N_2-fixing cultures of *R. palustris nif*A* as H_2 is an obligatory byproduct of nitrogenase-mediated N_2 hydrogenation. We investigated monocultures of *S. ovata* and *R. palustris* nifA* to characterize the behavior of each strain under different culturing conditions and to understand how to set up a symbiotic co-culture. *R. palustris* nifA* could consume acetate generated from CO_2 and H_2 by *S. ovata* and thus prevent culture acidification, whereas *S. ovata* could benefit by obtaining free NH_3 and H_2 from *R. palustris* nifA*-mediated N_2 fixation.

4.4.2 Characterization and manipulation of S. ovata and R. palustris nifA* co-cultures

Co-cultures involving at least one N_2-fixing bacterium have been demonstrated. These consortia have shown the ability of the N_2-fixing strain to provide its partner strain with necessary ammonia. LaSarre and colleagues established a cross-feeding mutualism wherein *R. palustris* consumed fermentative products from *E. coli* and subsequently released ammonia promptly taken up by the *E. coli*.[202] Smith *et al*. conceived of a co-culture in which a genetically engineered photosynthetic cyanobacterium fixed CO_2 and provided a N_2-fixing organism with fixed carbon products.[65] Here, we construct a co-culture between *S. ovata* and *R. palustris nif*A*. The advantages of our design comprise of the inclusion of *S. ovata*, capable of fixing CO_2 to acetate innately with reducing equivalents sourced from H_2 or from a (photo)electrochemical process. This lends the ability to direct the co-culture products by managing the available substrate gases and the magnitude and duration of the photo-electrochemical process.

We formulated a fixed carbon and nitrogen free minimal medium amenable for both *S. ovata* and *R. palustris nif*A* (fig. S4.7). Our first approach involved inoculating *S. ovata* and *R. palustris nif*A* concurrently in four sets of culture tubes (at OD_{660} of ~0.4) (fig. 3 a,c). The initial cell ratio of *S. ovata* to *R. palustris nif*A* was ~6:1 (determined by correlating OD to cell counts) and the headspace was pressurized to 175 kPa with a $H_2/CO_2/N_2$ (40/20/40%) gas mixture. We

tracked OD, acetate, total fixed nitrogen, and ammonia concentrations during the experimental period. Over the course of the experiment, the original headspace gas mixture was exchanged to pure N_2 at different time points in each of the four co-culture sets to observe co-culture growth dynamics under different headspace conditions. The four co-culture sets exhibited similar optical density growth over the first 3 days. At this time point less than 1.25 mM acetate was measured in all respective co-cultures and no ammonia was detected, which pointed to successful cross feeding. The headspace gas mixture was exchanged to pure N_2 in the first co-culture set after 3 days (fig. 4.3 a,c blue curve, bar). By day 10, the remaining three co-cultures with $H_2/CO_2/N_2$ headspace continued to exhibit growth more than doubling the initial OD, while the co-culture with a pure N_2 headspace showed markedly lower growth rate. Only trace concentrations of acetate and ammonia were detected in all the co-cultures. On day 10 the headspace gas mixture in a second co-culture was exchanged to pure N_2 (fig. 4.3a,c red curve, bar). By day 19 the two remaining co-cultures with $H_2/CO_2/N_2$ headspace had continued their linear growth trend while the two co-culture sets with N_2 headspaces had nearly plateaued. Following this observation, circa 0.5mM acetate was measured in the co-cultures with $H_2/CO_2/N_2$ headspaces, while no acetate could be detected in the co-cultures with pure N_2 headspaces pointing to *S. ovata* inactivity due to lack of H_2. On day 19 considerable amounts of NH_3 were detected in both co-cultures with pure N_2 headspaces illustrating that NH_3 cross feeding ceased as *S. ovata* became inactive. The headspace of one of the two remaining co-cultures with $H_2/CO_2/N_2$ headspaces was exchanged to pure N_2 on day 19 (fig. 4.3a,c green curve, bar). Final sampling was conducted on day 33 and demonstrated that the co-culture with $H_2/CO_2/N_2$ headspace grew to surpass OD_{660} 2.0 while cell densities in the cultures with pure N_2 headspaces plateaued (fig. 4.3a,c purple curve, bar). The co-culture with the $H_2/CO_2/N_2$ headspace proliferated past the densities achieved by either strain in a monoculture. The media did not become acidic as acetate was not allowed to accumulate, which sustained growth of the co-culture. Critically, the *S. ovata* in the co-culture remained active over the entire 33-day long experiment if H_2 was available, exhibited by a detectable amount of acetate on the final sampling day and an increase in total fixed nitrogen in the co-culture which was fueled by acetate. Continued co-culture growth over >1 month can be taken as proof of cross feeding between each species with *R. palustris nif*A* taking up acetate and *S. ovata* consuming ammonia. No significant amount of ammonia could be measured in the co-culture with $H_2/CO_2/N_2$ headspace whereas concentrations in the hundreds of μM were measured in the co-cultures after they were switched to N_2 headspaces.

While a successful *S. ovata* and *R. palustris nif*A* co-culture was realized, we sought to accelerate the culturing time with a modified approach. As evidenced by the lack of a typical exponential growth phase in the first co-cultures, acetate could be a limiting factor. Therefore, we inoculated *S. ovata* first with a H_2/CO_2 (80/20%) headspace for 24 hours to produce an initial acetate reservoir. Since acetate production for *S. ovata* is a growth-linked process, the pure *S. ovata* cultures were initially provided with 100 μM NH_3 to ensure high acetate production. This supplement was completely consumed within the first 24 hours. *R. palustris nif*A* is responsible for most of the co-culture growth as it grows photoheterotrophically on acetate and *S. ovata* grows autotrophically with limited ammonia. We determined that *S. ovata* has very meager growth when only supplemented with limited NH_3 (fig. S4.7b). Corroborating this point, LaSarre *et al*. found that the N_2-fixing organism dominates in a NH_3 deficient co-culture which in their study was demonstrated as *R. palustris* dominated growth when co-cultured with *E. coli*.[202] Therefore, our 24-hour pre-inoculation of *S. ovata* ensured a high acetate concentration (~ 15 mM) and no extra ammonia upon the introduction of *R. palustris nif*A* to accelerate co-culture growth (fig. 4.3b,d).

The growth in these co-cultures over the first 6 days was exponential in contrast to first co-cultures. Similar to the first co-culture experiments, the headspace was exchanged in one co-culture on day 2 (fig. 4.3b,d blue curve, bar), but the growth continued a similar trajectory as in the others. By day 6 the acetate reservoir had been depleted, and the co-culture growth rates slowed down significantly. On days 6 and 9, the second (fig. 4.3b,d red curve, bar) and third (fig. 4.3b,d green curve, bar) co-cultures had their headspaces exchanged for N_2 respectively. By the final sampling on day 14, the co-cultures with a N_2 headspace had plateaued while the remaining co-culture with $H_2/CO_2/N_2$ headspace maintained steady growth, albeit slowed from its initial phase (fig. 4.3b,d purple curve, bar). Extracellular ammonia was present in all the co-cultures with a N_2 headspace. The 24-hour *S. ovata* incubation strategy allowed the co-culture to reach an OD_{660} of 2.0 in half the time (14 vs 28 days). We plotted the densities when the headspaces were exchanged to pure N_2 and performed a regression analysis (fig. S4.9). Notably, the slope of both curves is similar though the y-intercept is greater for the curve belonging to the 24-hour *S. ovata* pre-incubation co-cultures. This points to comparable steady-state growth dynamics, though prior incubation of *S. ovata* for 24 hours grants the co-culture much faster initial growth (2X faster biomass accumulation).

Altogether these results indicate that *S. ovata* and *R. palustris nif*A* developed a robust consortium with cross-fed acetate and ammonia. Secondly, co-culture dynamics can be directed as evidenced by the changes that occurred post headspace exchange. When reducing equivalents such as H_2 exist, *S. ovata* supported *R. palustris nif*A* with sufficient acetate, resulting in quick consumption of acetate, biomass accumulation and no free ammonia in the culture. After losing access to H_2, *S. ovata* activity became minimal and free ammonia by *R. palustris nif*A* accumulated due to limited carbon sources.

4.4.3 Electrochemically- and solar-powered S. ovata and R. palustris nifA* based CO_2 and N_2 fixation

We employed a custom-made H-cell type electrochemical reactor which we reconditioned with metal clamps and supporting silicone o-rings to withstand pressurization. The total volume of each chamber was 160 mL. A TiO_2 and Ni-coated degenerate SiNW 2.25 cm^2 cathode was fabricated as previously described.[77] Pt wire and Ag/AgCl were used as counter and reference electrodes respectively. The electrolyte was composed as previously noted with some modifications (supplementary information). *S. ovata* was cultured as previously reported, except that the cells were washed 3 times anaerobically in fresh electrolyte after culturing autotrophically in minimal medium and thereafter introduced into the cathodic chamber of the electrochemical cell with 100 μM NH_3 mimicking the previous co-culture experiment.

We undertook the bioelectrochemical experiments in two stages: Firstly, we generated reducing equivalents on the cathode to power *S. ovata* acetogenesis and produce acetate. Thereafter, we ceased electrochemical inputs and introduced *R. palustris nif*A*, which consumed acetate for energy to fix N_2 and produce PHB. We undertook this staged approach to determine productivity and efficiency metrics for each co-culture product. For example, if we had inoculated *S. ovata* and *R. palustris nif*A* at the same time, we would not have been able to detect acetate, as it would have been instantly consumed by *R. palustris nif*A*. Accurately determining the concentration of acetate is paramount in this initial demonstration, as the co-culture behaves according to its culturing conditions with acetate concentration directing the make-up of N_2 products, namely NH_3 or nitrogenous biomass.

We allowed for three increasing amounts of charge to pass through the electrodes, as these would translate to increasing acetate outputs respectively (fig. 4.4a,b). For acetate, the lowest charge (99 ± 12 coulombs) resulted in a faradaic efficiency (FE) of 103% with a current density of 0.29 mA/cm^2. Similarly, a charge of 166 ± 20 coulombs translated to an FE of 93% and a current density of 0.35 mA/cm^2 while the experiment with the highest charge of 235 ± 15 coulombs rendered an FE and current density of 91% and 0.35mA/cm^2 respectively. After *R. palustris nif*A* was introduced, the FE's for nitrogen in biomass increase proportionally with charge from 13.7 to 17.4 and to 19.1%. The corresponding current densities demonstrate a similar trend increasing from 0.049 to 0.058 and to 0.067 mA/cm^2. Whereas nitrogenous biomass scaled with charge, NH_3 production revealed a dissimilar trend with the highest FE and current density peaking at 6.3% and 0.023 mA/cm^2 respectively for 166 ± 20 coulombs. The efficiency of ammonia production fell off with increasing charge. This trend mirrored that of the *R. palustris nif*A* monoculture experiment which exhibited an inverse proportionality between the starting amount of acetate and the concentration of extracellular NH_3 (fig. 4.2e). Therefore, the nitrogen products can be regarded as tunable because the amount of electrochemical charge passed to the culture dictated their composition. Mckinlay *et al*. determined an optimum production yield of 21±3 mol H_2 per 100 mol of acetate fed to *R. palustris nif*A*.[203] As H_2 is obligately generated alongside N_2 reduction by nitrogenase, we can stoichiometrically deduce that their nitrogen fixation yield was 42 mol fixed nitrogen per 100 mol acetate. Our *R. palustris nif*A* monoculture yielded 31.4±10.5 mol fixed nitrogen per 100 mol acetate, while electrochemically induction results in 28.6±6.8 mol fixed nitrogen per 100 mol acetate. When benchmarking our production metrics with those obtained by Mckinlay *et al.*, it is apparent that there is an opportunity for improvement which could increase the average electricity-to-fixed-nitrogen efficiency by at least 1.5-fold.

Importantly, *R. palustris* also synthesized PHB as a form of carbon and energy storage. We measured 1.04±0.04 mg/L PHB (0.8% carbon yield) which was commensurate with previous accounts.[204] PHB production could be maximized to up to 30% of the dry cell weight by limiting access to N_2.[196] Therefore, switching to a pure CO_2 headspace (instead of N_2) during co-culturing could direct PHB synthesis from acetate offering more tunable products for this co-culture platform. Though not verified in this study *R. palustris* has been reported to produce CH_4 simultaneously with NH_3 thus possibly positioning the co-culture platform to offer another carbon product.[205] Additionally, other forms of exploitable carbon storage products have also been observed for *R. palustris*, including glycogen and trehalose.[196] Moreover, isotope-labeled ^{13}C control experiments were employed (fig. S4.10). To further confirm N_2 fixation, we inoculated *R. palustris nif*A* into liquid cultures with argon (Ar) degassed medium. We then filled the headspaces with $^{15}N_2$, and Ar and provided acetate to each. Notably, the culture with Ar exhibited negligible growth and while the culture with $^{15}N_2$ accumulated biomass through $^{15}N_2$ fixation (fig. S4.11a). ^{1}H-qNMR results confirm no $^{14}NH_3$ in the Ar culture and $^{15}NH_3$ in the $^{15}N_2$ culture (fig. S4.11b). The absence of $^{14}NH_3$ in cultures with Ar and $^{15}N_2$ headspaces and the lack of growth in the Ar culture point to curtailed external contaminations.

Following the confirmation of an electrochemically supported platform, we investigated whether our system would allow for solar-driven CO_2 and N_2 fixation. We connected our electrochemical cell housing the bacterial co-culture to a photovoltaic device, as shown in diagram in figure 4.4c, and followed a process analogous to the electrochemical experiments. Similarly to our previous report, we used a commercially available multi-junction Si solar cell (V_{oc} 4.7 V, I_{sc} 4.4 mA under one sun illumination) to drive the reaction.[77] The light intensity was set at 25 mWcm^{-2} using an NREL calibrated Si photodiode. The system produced acetate with a solar-to-chemical

efficiency of 1.78±0.13% over two days and upon introduction of *R. palustris nif*A*, it was able to fix N_2 into nitrogenous biomass and ammonia with efficiencies of 0.51±0.05% and 0.08±0.007% correspondingly. To the best of our knowledge, no other platform has been reported for full solar-driven CO_2 and N_2 fixation.

Finally, we assessed the SiNW array used to support the bacterial culture by scanning electron microscopy (SEM). We noticed the presence of two distinct bacterial morphologies. One was bulbous, and the other was more tubular in appearance. We proceeded to culture *R. palustris nif*A* and *S. ovata* individually on SiNWs and examined them by SEM (Fig. S4.12a,b). We observed that the bulbous morphology can be attributed to *S. ovata* while *R. palustris nif*A* presents longer and thinner. These observations of the individual strain morphologies agree with the literature.[189,206] Next, we centrifuged down a mature co-culture at 12,000 rpm and found layering with the longer, heavier, and pink *R. palustris nif*A* underneath the shorter, lighter, and beige *S. ovata*, as evident by the distinct colors of each strain (Fig. S4.12c). A qualitative approximation of the final cell ratio is 2:3 *S. ovata* to *R. palustris nif*A*, having been seeded at an initial 6:1 *S. ovata* to *R. palustris nif*A* cell ratio. This result corroborates that most the co-culture growth stems from the N_2-fixing heterotrophic *R. palustris*, as has previously been claimed.[202] Finally, we were able to qualitatively identify each bacterial strain on the frontmost plane of an SEM micrograph as highlighted by false coloring in figure 4.4d. Fluorescence-activated cell sorting (FACS) or a fluorescence *in situ* hybridization (FISH) assay need to be performed to quantitatively report individual bacterial populations in future work.

Overall, we demonstrate a biohybrid co-culture capable of fixing CO_2 and N_2 to value-added products. We namely show that bio-produced acetate from CO_2 could be used to power N_2 fixation in a separate whole-cell catalyst. By assigning CO_2 and N_2 fixation to two separate biocatalysts, we are able maximize efficiency and rate. However, not only is acetate a fuel for N_2 fixation but it also provides a substrate for bioplastic synthesis and potentially manifold other carbon products owing to the metabolic versatility of *R. palustris*. Moreover, employing two separate biocatalysts in synergy allowed us to direct product outputs through electrochemistry and headspace inputs. We strongly believe that advances in bioelectrochemistry will arise from studying and engaging bacterial communities. Organisms in nature cooperate to thrive, and we must emulate these associations in biohybrid systems to tackle environmental challenges.

4.5 Figures

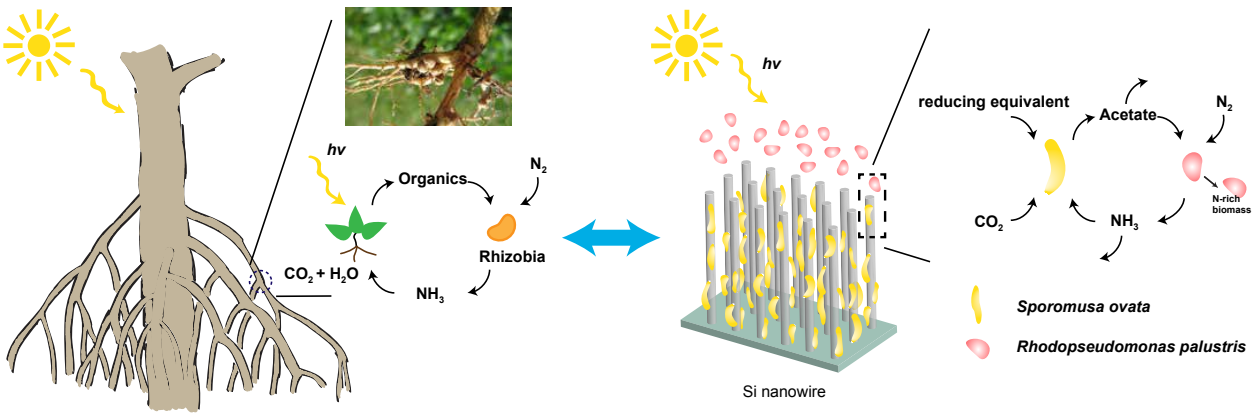


Figure 4.1 Bioinspired biohybrid co-culture design. Rhizobia inhabit the anoxic root nodules of legumes where they are provided with organics (e.g., malate) by the legume. The rhizobia in turn fix N_2 to nitrogenous compounds that the legume uses for growth. In our design, a SiNW/*S. ovata* ensemble generates acetate from CO_2 taking the place of the legume. And similar to rhizobia, *R. palustris* uses the acetate as a feedstock to convert N_2 to NH_3.

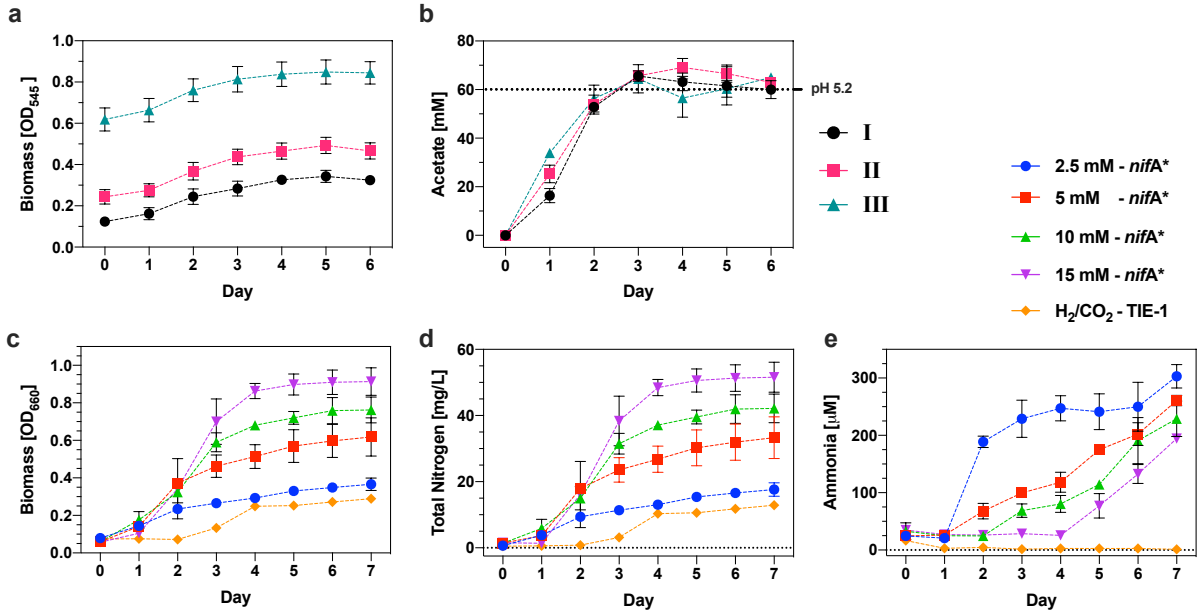


Figure 4.2 Monoculture characterization of *S. ovata* and *R. palustris*. a) Biomass and b) acetate tracking of autotrophic *S. ovata* monocultures I, II and III inoculated at sequentially increasing starting optical densities of OD_{545}=0.15, OD_{545} =0.225 and OD_{545} 0.6 respectively. Diazotrophic, photoheterotrophic *R. palustris nif*A * provided with synthetic acetate (2.5-15mM) and photoautotrophic *R. palustris* TIE-1 wild type monocultures supplied with a $H_2/CO_2/N_2$ headspace. Daily measurements of c) biomass, d) total nitrogen and e) ammonia. Error bars represent one standard deviation of three independent measurements.

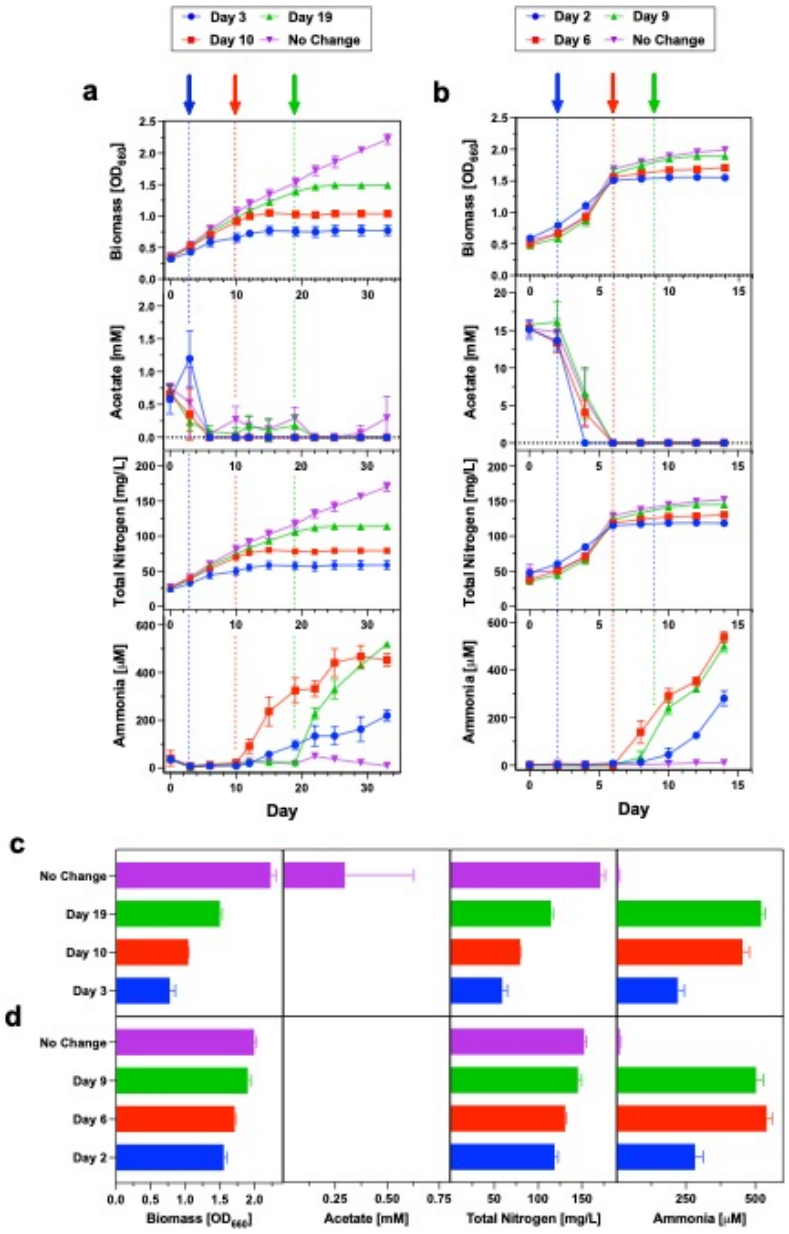


Figure 4.3 *S. ovata* and *R. palustris nif*A* co-culture characterization. a) *S. ovata* and *R. palustris nif*A* inoculated concurrently. b) *S. ovata* inoculated 24 hours before *R. palustris nif*A* is introduced into the culture. Legend signifies the day on which the headspace was exchanged from $H_2/CO_2/N_2$ to pure N_2 for each condition. Color matching dotted lines and arrows illustrate the day of headspace exchange on each individual plot. Bottom plots depict the summary of the results on the last sampling day for c) concurrent *S. ovata* and *R. palustris nif*A* inoculation and for d) 24-hour *S. ovata* incubation prior to *R. palustris nif*A* introduction. Error bars represent one standard deviation of three independent measurements.

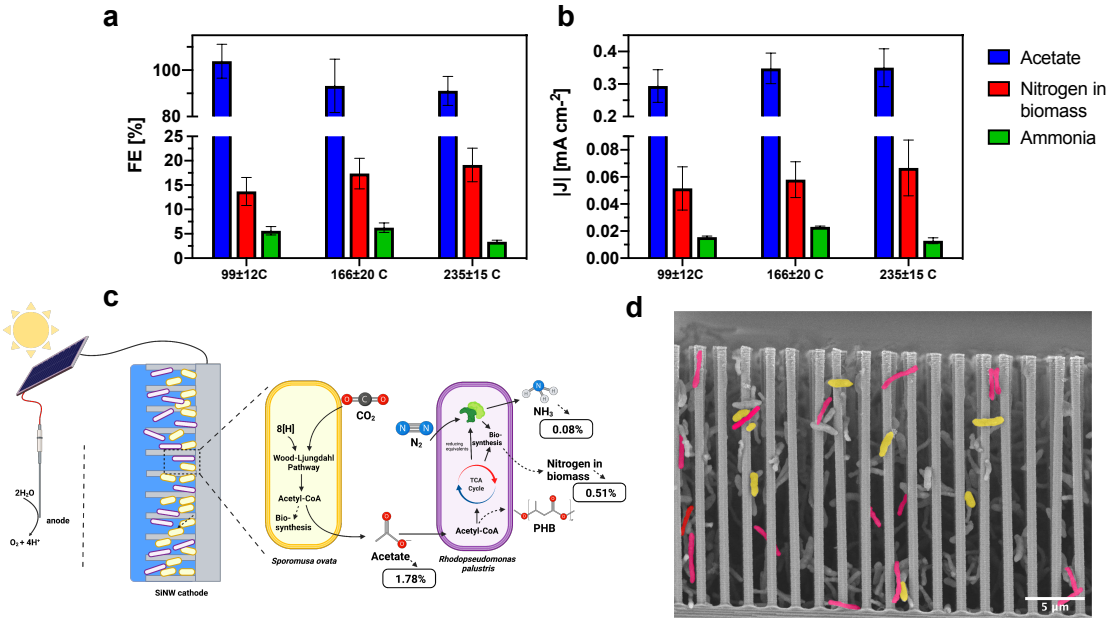


Figure 4.4 Electrochemically supported *S. ovata* and *R. palustris nif*A*. a), b) Faradaic efficiencies and current densities for co-culture products acetate, nitrogenous biomass, and ammonia respectively. c) Fully solar-powered co-culture via an external photovoltaic device with solar-to-chemical efficiencies. d) SEM micrograph of SiNW array with *S. ovata* and *R. palustris nif*A*. Individual bacteria on the frontmost plane identified and false colored based on morphology (*S. ovata* is yellow, and *R. palustris* pink). Error bars represent one standard deviation of three independent measurements.

Chapter 5: Abiotic sugar synthesis autocatalyzed by CO_2 electrolysis products

Reproduced in part with permission of collaborators:
Cestellos-Blanco, S.*, Louisia, S.*, Ross, M.B., Li, Y., Detomasi, T.C., Cestellos Spradlin, J.N., Nomura D.K., Yang, P.

5.1 Preface

This chapter marks a bit of a departure from the previous bioelectrochemical approach. It was inspired by our team's entry into NASA's Centennial CO_2 Conversion Challenge which called on scientists to convert CO_2 to glucose via a high-rate inorganic catalysis method. The intention was for the glucose to be used as a feedstock for genetically modifiable, fast-growing heterotrophic bacteria like *Escherichia coli* (*E. coli*). This would essentially enable the conversion of CO_2 through high-rate inorganic catalysis to a wide variety of products to be biomanufactured by a workhorse microorganism. This chapter lays out the roadmap for converting CO_2 to sugars and demonstrates that these sugars can sustain an *E. coli* culture. We firstly generated reactive aldehydes such as glycolaldehyde and formaldehyde electrochemically from CO_2. These aldehyde intermediates are reacted together catalyzed by a divalent metal cation such as Ca^{2+} through the formose reaction to form a soup of sugars. Through very minimal processing, we showcase how our sugar product can be used to sustain *E. coli*. There are many challenges to overcome, chiefly the low efficiency for the electroproduction of formaldehyde, which are highlighted in this chapter. Though certainly at the proof-of-concept stage, we envision that this new method can inspire further advancements for the conversion of CO_2 to complex products.

5.2 Introduction

As an abundant and inexpensive waste product, CO_2 is an attractive feedstock to produce functional chemicals and materials.[207–209] CO_2 is also a prime target for *in situ* resource utilization on Mars to enable crewed deep space exploration.[210–212] Various inorganic CO_2 catalysts operated either thermo- or electro-chemically have been developed but products have categorically been limited to C_{1-3} products with low selectvity.[213] Thermocatalytic platforms usually have high capital costs and require elevated temperature and pressure reactors to produce carbon products mostly through CO_2 hydrogenation and methanation.[214] Electrochemical CO_2 reduction platforms can be powered modularly by any electricity source and thus be sustained by renewable solar or wind energy sources, offering a promising way to close the loop of the carbon cycle.[215] Although catalytic optimization has been successful for the generation of the main 2 e^- reduction products, CO and $HCOO^-$, the formation of higher-order products has remained a challenge.[216–218] Cu remains the only element that displays a high turnover rate towards multi-carbon (C_{2+}) products.[219,220] However, limited progress has been made to boost its selectivity towards C_{2+} molecules due to the complexity of favoring one out of the many possible reaction pathways. Additionally, CO_2 has rarely been converted into molecules larger than three carbons due to the difficulty for one surface to successively facilitate multiple steps with distinct energy requirements.[15,221–224] CO_2 bioelectrosynthesis employing autotrophic bacteria as biocatalysts is a

complementary approach to the purely inorganic catalyst-mediated electrochemical CO_2RR affording high selectivity to C_{2+} products. [127,225] However, CO_2 turnover rates for autotrophic bacteria are orders of magnitude lower than those from heterogeneous electrochemical CO_2 reduction due to their sluggish autotrophic metabolism, and the requirement to maintain biocompatible conditions within the electrochemical set-up.

The ability to leverage the independent strengths of inorganically catalyzed CO_2 reduction and biocatalysis would be transformative, enabling scalable CO_2 reduction with selective production of multi-carbon products. Recently, the National Aeronautics and Space Administration (NASA) launched a Centennial Challenge focused on converting CO_2 to carbohydrate sugars.[226] These are to be employed as a high energy feedstock for fast growing and genetically modifiable bacteria like *Escherichia coli* (*E. coli*) enabling large scale chemical and material biomanufacturing. Therefore, the conversion of CO_2 to sugars would enable the selective biogeneration of a vast array of products.

On Earth, phototrophs convert CO_2 to polycarbohydrates establishing the first link in the food chain. However, to date, the abiotic conversion of CO_2 to sugars has not been reported. Here we demonstrate the initial roadmap for upgrading CO_2 electrolysis products to sugars (fig 5.1). We show that, by combining electrochemical CO_2 reduction with formose chemistry, we can use CO_2-derived glycolaldehyde as a key autocatalyst to synthesize sugars in sufficient quantities to sustain a living heterotrophic organism. We used a Cu nanoparticle (NP) ensemble electrocatalyst well-suited for the CO_2 electroconversion to glycolaldehyde.[227,228] Other than Cu-based CO_2RR, there is no clear one-pot CO_2 to glycolaldehyde conversion process.[229,230] Formaldehyde constitutes the primary carbon precursor for the formose reaction. While we demonstrate formaldehyde electroproduction from CO_2 on a boron-doped diamond (BDD) electrode, its productivity is too low to feasibly sustain the formaldehyde requirement of the formose reaction. Herein we point to avenues for potential improvement in electrochemical formaldehyde production to promote higher interest in this valuable product by the CO_2 electrochemistry community. As formaldehyde can be obtained from CO_2 by a thermochemical approach[231], we focus on establishing and optimizing the concept of combining glycolaldehyde-containing electrolyte with formaldehyde under formose reaction conditions to synthesize C_4-C_8 sugars, including glucose. These sugars were then employed as a feedstock for an *E. coli* culture. Altogether, we demonstrate a synthetic route to incorporate CO_2 electrolysis products into the production of life-sustaining sugars and indicate what more needs to be done to fulfill a complete abiotic CO_2-to-sugar conversion.

5.3 Materials and Methods

5.3.1 Electrochemical CO_2 reduction

7 nm Cu nanoparticles were synthesized as previously reported.[227] Boron-doped diamond (BDD) electrode (Electrode Kit Boron Doped Diamond, IKA) was rinsed with 20% HNO_3 and sonicated in DI water before use. All electrochemical measurements were carried in a custom-made H-cell consisting of two main compartments separated by a Selemion AMV anion exchange membrane (AEM). Ag/AgCl (WPI, 3 M KCl) was used as a reference electrode and a platinum wire was used as a counter electrode.

For glycolaldehyde production, 0.1 M $KHCO_3$ electrolyte was prepared by purging a 0.05 M K_2CO_3 (99.997% trace metal basis) solution with CO_2 overnight. Both the working and counter chambers were filled with 17 mL of the electrolyte and vigorous stirring was maintained in the working chamber. The input stream of CO_2 was humidified by being bubbled through DI water before being introduced into the cell. Before each measurement, the 17 mL catholyte was purged with 20 sccm CO_2 for 15-20 min until saturated.

Formaldehyde production was carried in various electrolytes including 0.1 M NaCl, 0.1 M $KHCO_3$, and 0.1 M $HClO_4$. The same procedure as for the CO_2-to-glycolaldehyde reaction described above was executed.

All electrode potentials measured against 3 M KCl Ag/AgCl reference were converted to the RHE scale using E (vs RHE) = E (vs Ag/AgCl) + 0.210 V + 0.0591 × pH. For all electrochemical experiments, 84% of ohmic loss was compensated by the potentiostat (Biologic) in real-time and the remaining 16% was manually post-corrected. Glycolaldehyde concentration was determined using quantitative NMR (qNMR) (Bruker AV-600) following. Dimethyl sulfoxide is used as an internal standard and an aliquot of the solution of interest prepared in D_2O. Solvent presaturation technique is implemented to suppress the water peak.

The concentration of gases produced throughout electrolysis was measured using a gas chromatograph (SRI GC) connected at the outlet of the cell. Gas chromatograph is equipped with a molecular sieve 13X (1/8" × 6') and hayesep D (1/8" × 6') column with Ar flowing as a carrier gas. Sample for gas chromatography was collected at 20-minute intervals and the separated gas products were analyzed by a thermal conductivity detector (for H_2) and a flame ionization detector (for CO and hydrocarbons). Quantification of the products was performed with conversion factors derived from the standard calibration gases and the concentration of gas measured was further converted to partial current density.

A formaldehyde detection assay (Sigma-Aldrich MAK131) was employed to quantify formaldehyde concentrations. Briefly, formaldehyde is derivatized with acetoacetanilide in the presence of ammonia yielding a fluorescent product with excitation and emission wavelengths at 370 nm and 470 nm, respectively. The fluorescent signal proportional to formaldehyde concentration was read using a Biotek Synergy LX Multi-Mode microplate reader.

Faradaic efficiencies (FE) were calculated from the amount of charge passed to produce each product divided by the total charge passed at a specific time (gas) or during the overall run (liquid).

5.3.2 Formose reaction

The formose reaction was performed as described in previous literature.[232,233] Initial reagents were paraformaldehyde, glycolaldehyde dimer, and $Ca(OH)_2$ (Sigma Aldrich). Commercial paraformaldehyde was suspended in distilled water, heated to 70°C, and refluxed under alkaline conditions to depolymerize, producing a homogeneous, colorless solution. Glycolaldehyde and $Ca(OH)_2$ were dissolved in distilled water. The total reaction volume was typically 3 mL with 10 mM $Ca(OH)_2$, with the concentrations of formaldehyde and glycolaldehyde as well as the temperature dependent on desired experimental conditions. The reactions were carried out for 75 minutes and then quickly cooled down to room temperature. Upon completion, the samples

exhibited the characteristic bright yellow color of the formose reaction. For CO_2-derived formose reaction, the CO_2RR electrolyte was used directly without any processing. For example, for a 3 mL reaction volume, 1.5 mL of CO_2RR electrolyte with 30 μM glycolaldehyde was combined with an equivalent volume of distilled water. $Ca(OH)_2$ and formaldehyde were added to concentrations of 60 and 70 mM, respectively. The reaction was maintained at 75°C for 75 minutes. The pH was titrated with 1 M NaOH/HCl to 11.

5.3.3 Product and material characterization

^{1}H-NMR

The liquid products accumulated during CO_2 electrolysis and the sugars produced during the formose reaction are analyzed by quantitative NMR (qNMR) (Bruker AV-600) following the same procedure. Dimethyl sulfoxide is used as an internal standard and an aliquot of the solution of interest prepared in D_2O. Solvent presaturation technique is implemented to suppress the water peak.

Mass spectrometry

The produced carbohydrates are benzylated to ensure their separation from their salty matrix post-formose reaction.[234] The aqueous sample is mixed with NaOH/K_2CO_3 (1/4, w/w), benzene, isopropanol, tetrabutylammonium hydrogen sulfate, benzyl chloride, and DMSO. The solution is then vigorously stirred using a stir bar at room temperature for 4 hours. Subsequently, the mixture is worked up using cyclohexane, washed with water, and dried over Na_2SO_4. The benzylated carbohydrates were then injected into an electrospray ionization mass spectrometer (ESI-MS) for mass analysis.

HPAEC-PAD

The completed reactions were analyzed by high-performance anion exchange chromatography with pulsed amperometic detection on a Dionex ICS-5000. The samples were run on a CarboPac™ PA20 IC Column using a 0.4 mL/min isocratic gradient as follows: with 10 mM NaOH for 30 min, 100 mM NaOH for 5 min, and 10 mM NaOH for 5 min. A gold electrode in carbohydrate quad potential mode was employed as the detector. Upon injection, the elution is carried with 10 mM NaOH for 30 min, 100 mM NaOH for 5 min, and 10 mM NaOH for 5 min. Runs were compared to standards of (2-6 carbon) biologically relevant sugars: arabinose, glucose, ribose, fructose, acetaldehyde as well as formaldehyde were employed to identify peaks in the trace.

SEM

Cu nanoparticle coated and BDD electrodes were directly imaged by SEM at 5 keV (Ultra 55-FESEM).

5.3.4 Cell culture

XL1-blue *E. coli* cells were obtained from the Berkeley-QB3 MacroLab. *E. coli* stock stored at -80°C, was inoculated in Lysogeny Broth (Table S5.1) and incubated at 37°C in three consecutive cultures to remove any cryoprotectant. The formose reaction solution was filtered to remove precipitates and the products were recovered using a rotary evaporator. The experiment appropriate mass of bulk formose sugars (0-0.1% (w/v)) was added to the M9 minimal medium and syringe

filtered to sterilize. The cells were then inoculated in M9 minimal medium (Table S5.2) supplemented with glucose or formose sugars. *E. coli* growth curves were acquired in a Tecan M1000 plate reader in a 48-well plate for 24 hours at 37°C under continuous orbital shaking.

5.4 Results and Discussion

5.4.1 CO_2 electrochemical reduction to aldehyde precursors

The electrochemical reduction of CO_2 on Cu catalysts yields more than 16 different products with aldehydes often contributing to less than 5% of the total faradaic efficiency (FE).[223] The formation of surface bound CO (*CO) intermediates and subsequent C-C coupling are both necessary steps for the mechanistic pathway leading to the formation of aldehydes and further reduced C_{2+} products (fig. 5.2a). However, after C-C coupling, aldehydes are expected to be further reduced which is likely the reason for their overall lower efficiency.[235–237] Consequently, catalysts that have been reported with high FE for C_{2+} products, and especially for C_{2+} oxygenates, are more likely to produce an intermediate species like glycolaldehyde. The Cu NP ensemble previously reported in our group (fig. 5.2b) is therefore an ideal candidate to optimize the production of glycolaldehyde due to its high intrinsic activity for CO_2-to-C_{2+} conversion at low overpotential (i.e., partial current density per surface Cu atom 7-fold greater than traditional Cu foil at -0.80 V vs RHE).[227,228] The catalytic properties of this Cu NP ensemble towards glycolaldehyde specifically sits in a favorable range both in terms of selectivity (FE) and activity (current density) when compared to other Cu-based catalysts (fig. S5.1 and S5.2). We evaluated the performance of the Cu NP ensemble across different applied potentials to maximize the rate of CO_2-to-glycolaldehyde production. We identified the peak production to reach 12 μg/hour at -0.80 V vs RHE (fig. 5.2c). An increase or decrease in the overpotential is likely more favorable to the reduction of produced aldehydes or the hydrogen evolution reaction (HER), respectively. Indeed, the peak production of glycolaldehyde occurs at a more positive potential than ethylene and ethanol further suggesting that a too negative applied potential will further reduce any produced aldehydes (fig. S5.3).

Given the optimal applied potential, we then investigated how to further maximize the concentration of glycolaldehyde. The CO_2RR activity of the Cu NP ensemble remains steady after hours of operation as demonstrated by the stable current density and product distribution monitored by gas chromatography (GC) (fig. 5.2d and S5.4). However, the concentration of aldehyde begins to plateau after 5 hours of electrolysis (fig. S5.5). The interrupted accumulation of aldehyde is likely due to their propensity towards further reduction to alcohol or alkene over time.[235–237] As a result, we considered 4 hours CO_2RR adequate to consistently obtain a high enough concentration of glycolaldehyde.

Despite our optimization of the CO_2 electroconversion to glycolaldehyde, the reaction is inherently limited, and the FE of this process has rarely been improved beyond 2-3%. Consequently, we explored ways to convert CO_2 to another relevant reactant to produce sugars: formaldehyde. Traditionally, formaldehyde is derived from syngas or methanol through well-established industrial synthetic processes.[32,38] Nakata *et al*. have presented a promising electrocatalytic avenue to convert CO_2 to formaldehyde with a FE of up to 65% using a BDD electrode.[238] Inspired by this demonstration, we combined previous insights obtained from CO_2

electroreduction on BDD to evaluate its potential for the aqueous production of formaldehyde (Discussion S5.1 and fig. 5.2b). However, using the same reaction conditions as reported by Nakata et al., we did not produce formaldehyde at a comparable FE, and the reaction was principally dominated by HER (fig. 5.2e and S5.6).[238] Future work will require further investigation of the catalyst synthesis to enhance the selectivity. In addition, the high reactivity of formaldehyde exacerbated both under reducing conditions and in the presence of hydroxyl anions will require adjusted reactor and operation design to maximize the reaction turnover. Reducing conditions and the proximity to hydroxyl anions promote aldehyde disproportionation of formaldehyde to primary alcohols and carboxylic acids.[239] Though we were unable to generate an aldehyde product in either glycolaldehyde or formaldehyde in sufficient quantities to alone sustain sugar synthesis, we forged ahead to demonstrate the feasibility of forming sugars integrating CO_2 products and to motivate the electrochemical community to consider aldehydes as valuable CO_2RR products. Consequently, we find that glycolaldehyde is an essential autocatalyst in the formose reaction, even in low, CO_2-derivable concentrations.

5.4.2 Sugar syntheses using the formose reaction

The formose reaction was established by Aleksandr Butlerov in 1861 though it received renewed attention in the 1950's and 60's principally led by Ronald Breslow and Alvin Weiss.[240–242] The reaction is catalyzed by an alkaline metal ion (e.g., Ca^{2+}) under mild heating and alkaline conditions. Condensations and tautomerizations of reactive intermediates convert aldehyde starting reactants into a mixture of sugars through a cyclical polymerization-like process (fig. 5.3a).[240] Though various formose catalysts have been employed, we used Ca^{2+} as it is a low-cost and non-toxic catalyst, which is significant if the sugars are to be used as a feedstock in a bioprocess.[232,233,243]

Having demonstrated CO_2RR for the generation of glycolaldehyde and formaldehyde albeit in small quantities, we sought to verify the formose reaction conditions for the conversion of glycolaldehyde and formaldehyde to sugars. We initially optimized the formose reaction with non-CO_2 derived standard samples of glycolaldehyde and formaldehyde. While the formose reaction has been thought to start as the aldol condensation of two formaldehyde molecules to form glycolaldehyde, such direct dimerization only occurs in very specific conditions (i.e., in the gas-phase or under gamma-irradiation) and has been appraised in the literature as "chemically impossible" in the absence of glycolaldehyde in aqueous solutions.[244–246] Thus the Cannizzaro disproportionation of formaldehyde dominates in an alkaline environment converting formaldehyde to methanol and formic acid instead of sugars.[240,247] As a result, we confirmed experimentally that formaldehyde alone with $Ca(OH)_2$ yields only methanol and formic acid (figs. 5.3a and S5.7). The formose process can be initiated by adding glycolaldehyde, thus shortening the induction period and suppressing the competing Cannizzaro reaction.[245] Glycolaldehyde autocatalytically initiates the formose reaction cycle, in which formaldehyde condenses to a second molecule of glycolaldehyde. The autocatalytic cycle occurs at a much faster rate producing more glycolaldehyde which also reacts with other intermediates to form higher order sugars. Sugars can arise from aldol condensations involving glycolaldehyde as the active methylene component and another aldehyde as the carbonyl component.[240] Glycolaldehyde, even in trace quantities, is an essential autocatalyst for the formation of sugars. We verified that glycolaldehyde alone produces sugars confirming a sugar formation pathway through glycolaldehyde (figs. 5.3a and S5.7).

Therefore, electrochemical CO_2RR-derived glycolaldehyde (e-CO_2Glyc) is a necessary element autocatalyzing CO_2-derived sugar (CO_2Sugar) production.

The formose reaction conditions were optimized to yield the highest quantity of biological feedstock products such as glucose (fig. 5.3). High-performance anion exchange chromatography with pulsed amperometric detection (HPAEC-PAD) was used for the separation and detection of a variety of carbohydrates of comparable weights (fig. 5.3).[248] Unlike other analytical techniques, the separation allows for the identification of structurally similar carbohydrates (i.e., glucose vs fructose) (fig. S5.8).

As a wide range of temperatures has been reported to enable the formose reaction, we tested a range from 45 to 85°C in 10°C increments (fig. 5.3b).[249] A minimum temperature of 55°C was required to activate the reaction. Furthermore, 65°C yielded a higher proportion of C5 sugars (63%), while 75°C yielded more C6 sugars (78%). The total of 2.6 μmol sugars obtained at 75°C further decreases to 0.66 μmol at 85°C, as sugars may decompose into tar at the elevated temperature. We further determined the required concentration of formaldehyde to drive the formose reaction (fig. 5.3c). The Cannizzaro reaction dominates at concentrations below 35 mM as higher formaldehyde concentrations are needed to provide a driving force for C-C bond formation.[241] We found that a concentration of 70 mM formaldehyde adequately serves to synthesize feedstock sugar products. We observed that formaldehyde concentrations starting at 140 mM do not adequately generate sugars. As has been previously described, this is caused by an insufficient concentration of insoluble $Ca(OH)_2$ present to catalyze the reaction.[250] Lastly, since the concentration of e-CO_2Glyc is low (~ 30 μM), it is essential to establish the minimum glycolaldehyde concentration necessary to autocatalyze the formose reaction. We determined this threshold concentration to be 1 μM as presented in figure 5.3d. This is commensurate with glycolaldehyde provided by the CO_2RR. A higher total amount of sugars is obtained with higher glycolaldehyde concentrations (fig. 5.3d). In summary, in the adapted reaction conditions of 70 mM formaldehyde, 75°C and 10 μM glycolaldehyde among the biologically relevant sugars that we identified glucose is the major product (49%), followed by fructose (20%), ribose (17%), galactose (8%), and arabinose (5%).

5.4.3 CO_2 electrolysis products as sugar building blocks

After establishing the optimal conditions for the formose reaction, we tested whether e-CO_2RR-derived products could undergo the formose reaction. The as-obtained concentration of formaldehyde is too low to support the formose reaction as evidenced by Figure 3c. Formaldehyde can be obtained in high yields from CO_2 through industrially established high temperature and pressure hydrogenation of CO_2 to methanol and subsequent formox process.[231,251,252] Formaldehyde can also be concentrated through fractional distillation, which we attempted to partial success but are not presently able to sufficiently scale up (fig. S5.9). The direct conversion of glycolaldehyde alone to sugars is another avenue enabled by the formose reaction, as glycolaldehyde alone enables sugar generation (fig. S5.7). However, presently achievable e-CO_2Glyc concentration is too low to alone support the formose reaction (fig. S5.10). As with formaldehyde, a high concentration of glycolaldehyde is required for sugar generation through the formose reaction (fig. S5.11). As formaldehyde can be obtained industrially in high titers from CO_2 and there is no demonstrated CO_2-to-glycolaldehyde one-pot synthesis, we focused our efforts on e-CO_2Glyc as the essential formose autocatalyst. Hence, we demonstrate a proof-of-concept

sugar generation from commercial formaldehyde (to be CO_2-derived) autocatalyzed by e-CO_2Glyc.

We used the unadulterated CO_2 electrolysis product stream as the glycolaldehyde source with our optimized formose reaction conditions for the conversion of formaldehyde to sugars. The high $KHCO_3$ concentration (0.1 M) in the electrolysis product mixture posed further obstacles. Firstly, the Ca^{2+} and CO_3^{2-} combine to form highly insoluble $CaCO_3$ which does not adequately catalyze the formose reaction. Secondly, $KHCO_3$ acts as a buffer that alters the optimal pH upon addition of the divalent metal catalyst. Thirdly, the high salinity of the reaction mixture complicates product characterization with mass spectrometry by suppressing ionization. Nonetheless, we were able to introduce sufficient $Ca(OH)_2$ for the reaction to proceed by adding excess $Ca(OH)_2$ 10 mM above the concentration of $KHCO_3$ and by carefully titrating the reaction mixture pH with NaOH/HCl to pH 11.

The use of the unadulterated CO_2 electrolysis product stream to produce CO_2Sugars presents another challenge with the introduction of a multitude of coexisting CO_2-derived molecules. The complexity of the reaction mixture complicates the analysis of CO_2Sugars. Therefore, unlike in the previous formose reaction optimizations, HPAEC-PAD measurements are in part affected by the high concentrations of other CO_2-derived products (e.g., ethanol, formate) and by the presence of HCO_3^- anions (fig. S5.12). Fortunately, the spectral signature of sugars is easily distinguishable using ^{1}H-NMR. Specifically, the chemical shifts for carbohydrate protons are typically observed in the 3.5-5 ppm region while most of the other CO_2RR products are found in the 0-4 and >7 ppm region (fig. S5.13). Therefore, the appearance of multiple peaks in this region was used as an initial indication for the formation of CO_2Sugars. With the Ca^{2+} catalyst concentration and pH optimization, ^{1}H-NMR results indicate that CO_2Sugars formation can be autocatalyzed by CO_2Glyc (fig. 5.4a).

Beyond the sugar fingerprint identified by ^{1}H-NMR, we used electrospray ionization mass spectrometry (ESI-MS) to further determine the variety of CO_2Sugars.[253] As previously mentioned, the high salinity of our reaction containing K^+, Na^+, and Ca^{2+} poses an obstacle to ESI-MS analysis. Therefore, we separated our CO_2Sugars from the salty aqueous solution via liquid-liquid extraction by protecting their hydroxyl groups (benzylation), thus increasing their solubility in organic solvents (fig. S5.14). The derivatization of CO_2Sugars by benzylation and separation from the salty mixture allowed their characterization by ESI-MS. These measurements revealed a diverse mixture of fully and partially benzylated carbohydrates ranging from three to eight carbons (fig. 5.4b).

Although powerful, ESI-MS analysis is limited to the identification of sugars of the same molecular weight. HPAEC-PAD remains the method of choice to distinguish multiple carbohydrates of similar compositions (i.e., glucose from galactose or fructose). The high baseline tailing effect observed in the chromatogram of CO_2Sugars likely results from the saturation of the column due to the high concentrations of HCO_3^- present as buffer (fig. S5.12 and S5.16). Nevertheless, carbohydrates in the reaction mixture are still distinguishable during HPAEC-PAD measurements. Comparing the chromatograms of carbohydrate standards with the reaction mixture of CO_2Sugars confirms the presence of biologically relevant sugars such as glucose (fig. 5.4c). Further separation of the reaction mixture from HCO_3^- and other overlapping molecules will be required to improve the analysis of CO_2Sugars and enable quantification by HPAEC-PAD. Additionally, a more extensive survey of carbohydrate standards beyond those that are significant as biological feedstocks should be performed to complete the catalog of CO_2Sugars produced.

To highlight the broad applicability and reproducibility of employing e-CO_2Glyc as the autocatalyst in the formose reaction, we used e-CO_2Glyc obtained at varying CO_2RR conditions. We compared the CO_2Glyc generated at three successive potentials with the Cu NP ensemble and with Cu foil. The input e-CO_2Glyc concentration was normalized across the electrolytes before beginning the formose reaction. As demonstrated by the ^{1}H NMR and HPAEC-PAD spectra (fig. S5.15 and S5.16) for the four different conditions, there is little difference in the ensuing CO_2Sugars. This confirms that the formose reaction is robustly adaptive to different CO_2RR conditions given sufficient CO_2Glyc.

5.4.4 *E. coli* cultures supported by CO_2-derived sugars

With biologically relevant sugars—ribose, galactose, fructose, arabinose, and glucose— in hand, we sought to use them to sustain bacterial growth. Glucose is the preferred source of carbon for *E. coli*; however, it can also metabolize a variety of other carbohydrates including many of those produced in the formose reaction.[254] We collected the products from the standard formose reaction and from CO_2Sugars and employed them directly as feed sources for *E. coli* cultures. We used minimal processing to prepare the formose sugars; briefly, we syringe filtered the solutions directly after the formose reaction to remove precipitates, crystallized the sugars via rotary evaporation which also removed cytotoxic components (e.g., methanol, ethanol), and added a commensurate amount (0.1% w/v) to M9 minimal bacterial medium (Table S5.2). The medium containing the formose sugars was syringe sterilized before inoculating with *E. coli*. Culture growth and biomass accumulation were assessed by optical density. Formose- and CO_2Sugars-fed cultures achieved maximum optical densities of ~0.26 and ~0.22, reaching stationary phases after 4.3 and 3.8 hours respectively (fig. 5.5a). These optical density values correspond to nearly half of the maximum optical density of a control *E. coli*. culture provided with 0.1% pure glucose (fig. S5.17). The optical density of the formose-fed *E. coli* culture is expectedly lower as the feed source consists of a mixture of sugars that may not be metabolizable or metabolized suboptimally when compared to pure glucose. Nevertheless, these results demonstrate that CO_2Sugars can sustain heterotrophic microorganisms in a raw form with little processing. This minimization of processing and separation steps that may be resource-prohibitive is especially valuable for industrial and extra-terrestrial applications. Furthermore, we verified that available CO_2Sugars present in minimal medium were consumed during bacterial growth. To establish this, we obtained ^{1}H-NMR spectra before and after the culturing period. As exhibited in Figure 5c the carbohydrate associated proton peaks mostly disappear after bacteria are grown in the medium. Additionally, the appearance of a peak at ~1.8ppm indicates the formation of acetate during culture growth. *E. coli* secrete acetate as a by-product of glycolysis during aerobic growth in minimal medium. [255] Finally, *E. coli* growth can be visually confirmed in the medium containing different sugars sources (fig. 5.5b). In the future, we envision the production of CO_2Sugars could be coupled with a biomanufacturing platform to generate value-added products on demand.

When taken together, we demonstrate an approach to employ the outputs of CO_2 electrosynthesis to generate sugars. Our work invites the CO_2 electrocatalysis community to reconsider the processing value of so far overlooked by-products. Although minor, some of the building blocks present in the streamline of CO_2 electrolysis could be readily utilized for the construction of biologically-significant molecules. However, there remain several scale-up steps to be determined before achieving a catalytic turnover akin to biological processes. The electrochemical production of both glycolaldehyde and formaldehyde presented in our work is

limited to the μM scale. To maximize these turnovers, catalyst development, electrochemical conditions, and setup designs will require further investigation. As an example, the application of a flow cell design can be used to minimize the further reduction of produced glycolaldehyde. Further studies of the catalyst properties necessary to advance the CO_2 electroreduction to formaldehyde will be required to achieve the targeted activity. For the maximization of both aldehyde concentrations, an additional processing step of distillation should be considered. With such developments, we envision that this inorganic platform could rival photosynthesis in commercial sugar production and could mitigate CO_2-driven climate change. Overall, this proof of concept demonstrates how various catalytic systems can be tailored to facilitate CO_2 conversion to life-sustaining molecules, far beyond the hydrocarbons usually reported in the field of CO_2 electrocatalytic up-cycling.

5.5 Figures

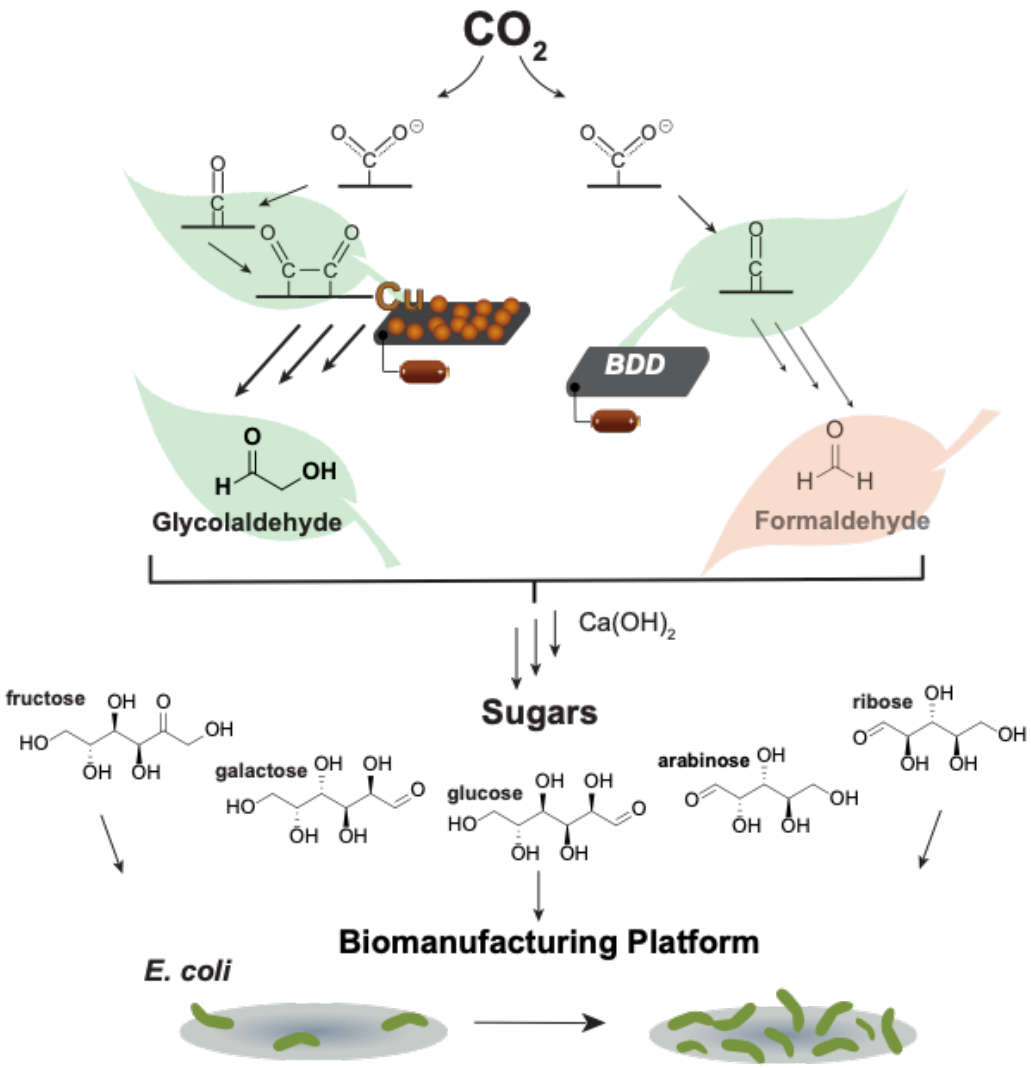


Figure 5.1 Roadmap to sugars: coupling of electrosynthesis with thermocatalysis to convert CO_2 to sugars. CO_2 is electrochemically reduced on copper nanoparticle and boron-doped diamond cathodes to glycolaldehyde and formaldehyde, respectively. Formaldehyde is shaded to indicate that this current pathway does not produce a adequate titer. The thermochemical conversion of formaldehyde with glycolaldehyde is initiated with a divalent metal cation (e.g., $Ca(OH)_2$) at mildly elevated temperatures (<100°C). The generated sugars are readily used as a feedstock for *Escherichia coli* enabling the conversion of CO_2 to a multitude of complex chemicals.

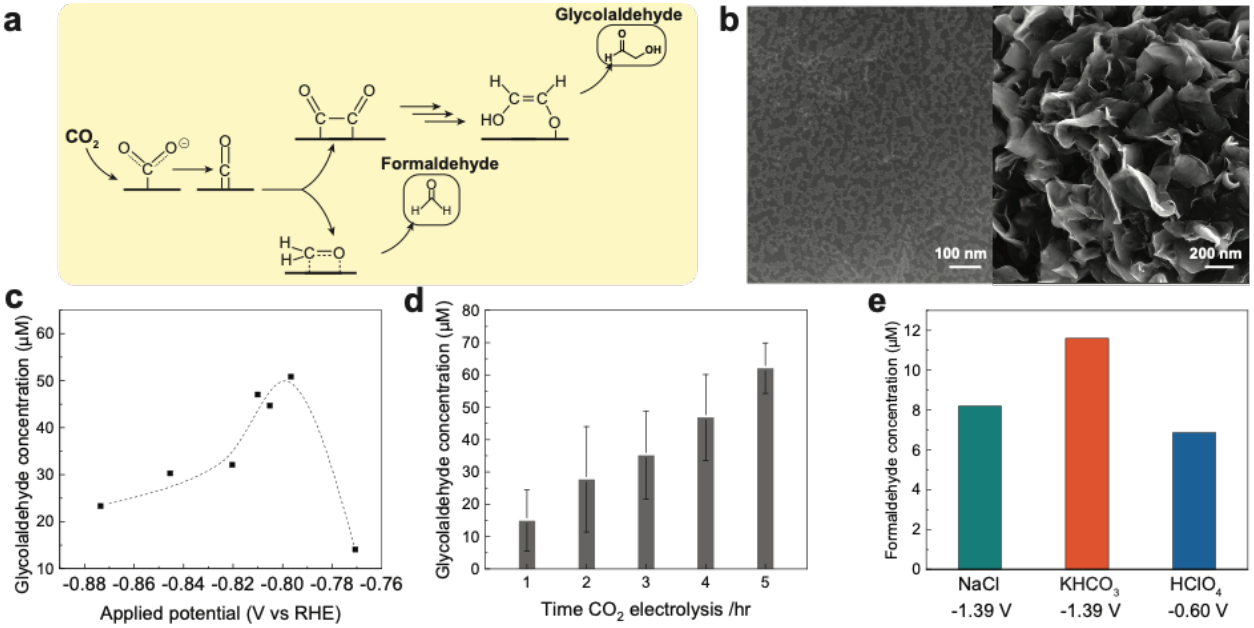


Figure 5.2 CO_2 electrolysis produces upgradeable aldehydes. (a) Scheme of the mechanistic pathway of CO_2 electroreduction to glycolaldehyde and formaldehyde. (b) SEM of the Cu NP ensemble (left) and the BDD (right) electrocatalysts. (c) Concentration of glycolaldehyde obtained after 4 hours of CO_2 electrolysis in 0.1 M $KHCO_3$ using the Cu NP ensemble at various applied potentials. (d) Accumulation of glycolaldehyde produced at -0.80 V vs RHE as a function of electrolysis time using the Cu NP ensemble in 0.1 M $KHCO_3$. (e) Concentration of formaldehyde obtained after 1 hour of CO_2 electrolysis using a BDD electrode in 0.1M NaCl, $KHCO_3$ and $HClO_4$ electrolytes. All applied potentials are reported

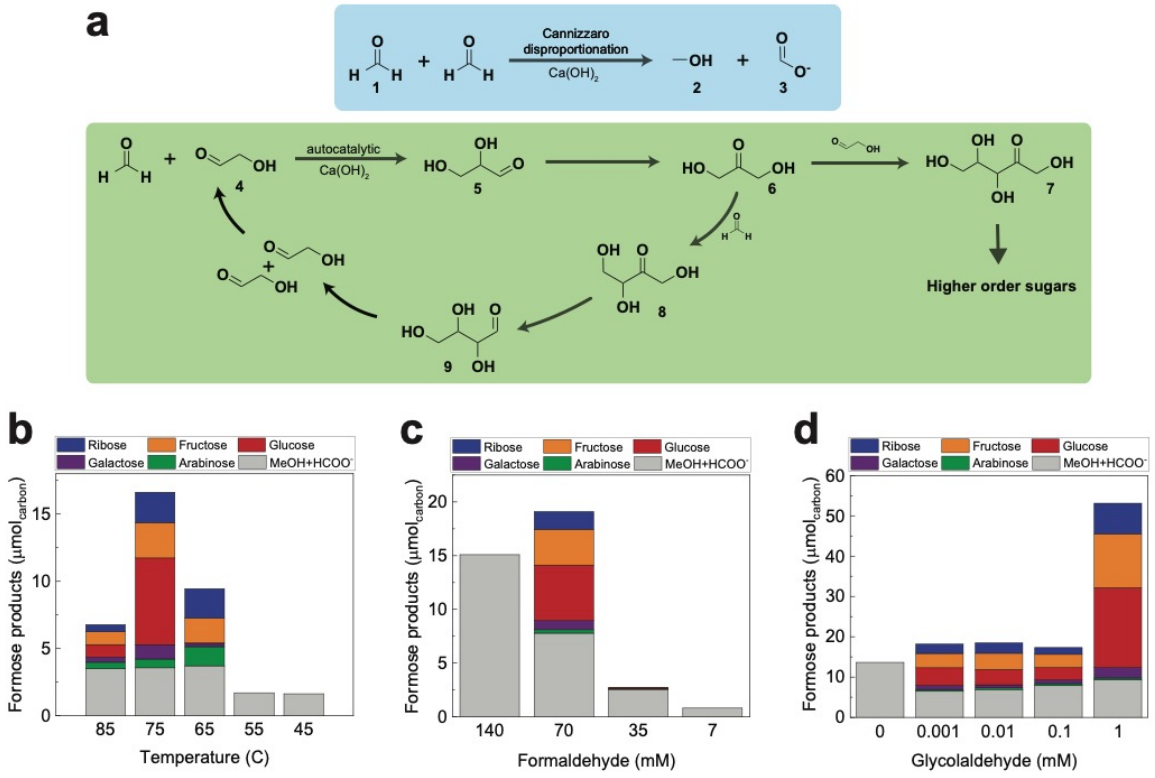


Figure 5.3 Formose reaction overview and optimization. (a) Upper inset: the Cannizzaro disproportionation of formaldehyde (1) methanol (2) and formate (3). In the absence of glycolaldehyde as an autocatalyst, the Cannizzaro reaction dominates in alkaline and aqueous conditions. Lower inset: overview of the formose reaction autocatalyzed with glycolaldehyde (4). Briefly, an aldol condensation of (1) and (4) generates glyceraldehyde (5), which undergoes an aldose-ketose isomerization to make dihydroxyacetone (6). (6) and (4) react to form ribulose which isomerizes to ribose (7). (6) may also undergo a further aldol condensation with (1) to make tetrulose (8), which isomerizes to aldetrose (9). A retro-aldol reaction of (9) produces two molecules of (4), thus forming an autocatalytic cycle. (b) Formose product distribution based on temperature with 100uM glycolaldehyde and 70mM formaldehyde. (c) Formose product distribution with varying formaldehyde concentration with 100uM glycolaldehyde at 75C. (d) Formose product distribution with varying glycolaldehyde concentration with 70mM formaldehyde at 75C. Sugars are quantified by HPAEC-PAD, and methanol and formate are determined by ^{1}H-NMR.

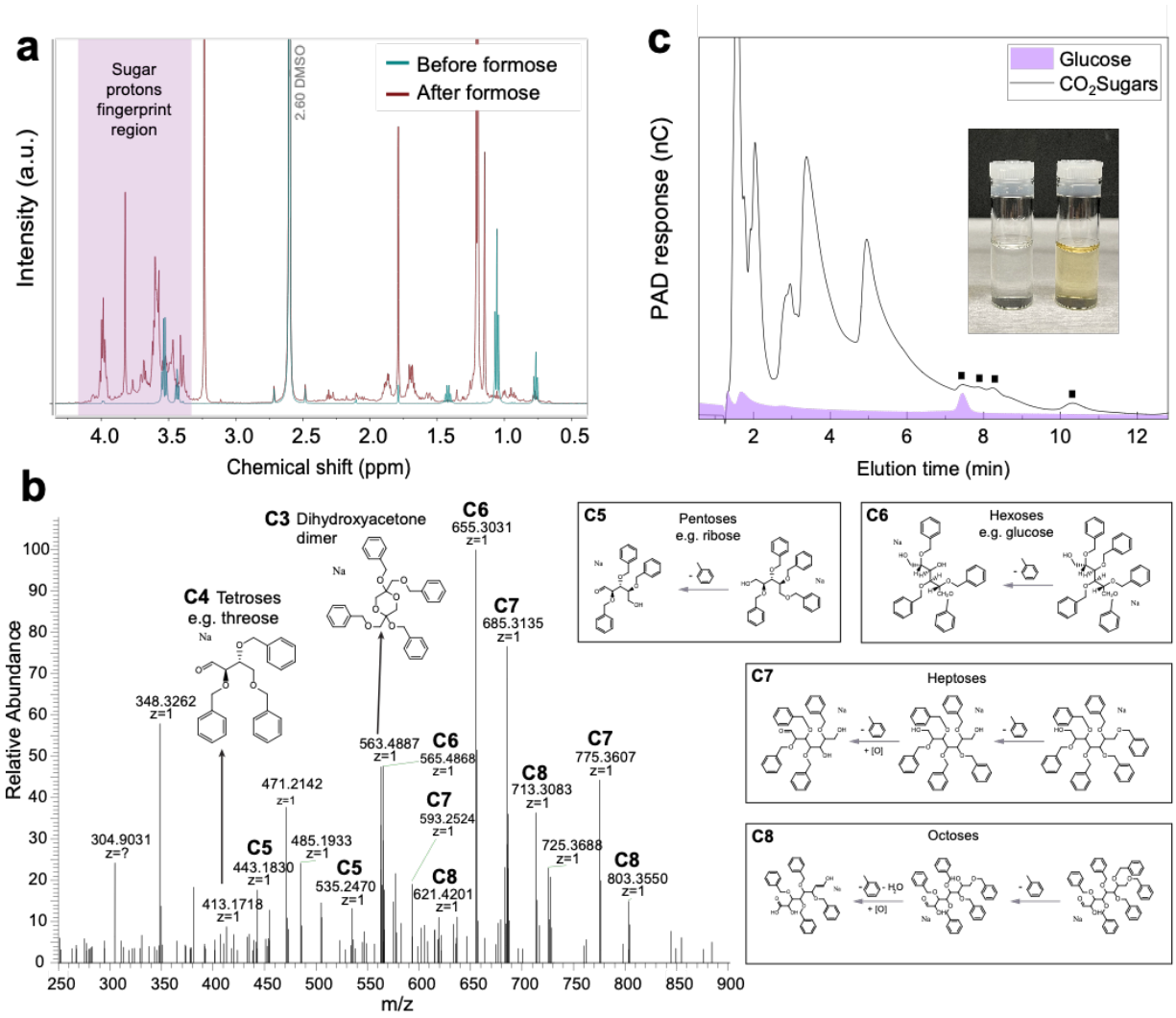


Figure 5.4 Sugar synthesis catalyzed by CO_2 derived glycolaldehyde. (a) ^{1}H-NMR spectra pre- and post- formose reaction demonstrating the appearance of carbohydrate protons in the 3.5-5ppm region. (b) ESI-MS spectrum reveals a diverse mixture of benzylated sugars including pentoses, hexoses, heptoses, and octoses. (c) HPAEC-PAD spectrum reveals the presence of distinguishable CO_2Sugars obtained from the product stream of Cu NP ensemble at -0.80 V vs RHE. Visible peaks in the chromatograms are indicated by black squares. One of them is identified as glucose as it overlays closely with the glucose reference chromatogram. Inset picture displays the product of the formose reaction without e-CO_2Glyc (left) and autocatalyzed by e-CO_2Glyc (right). The yellow color is characteristic of sugar production.

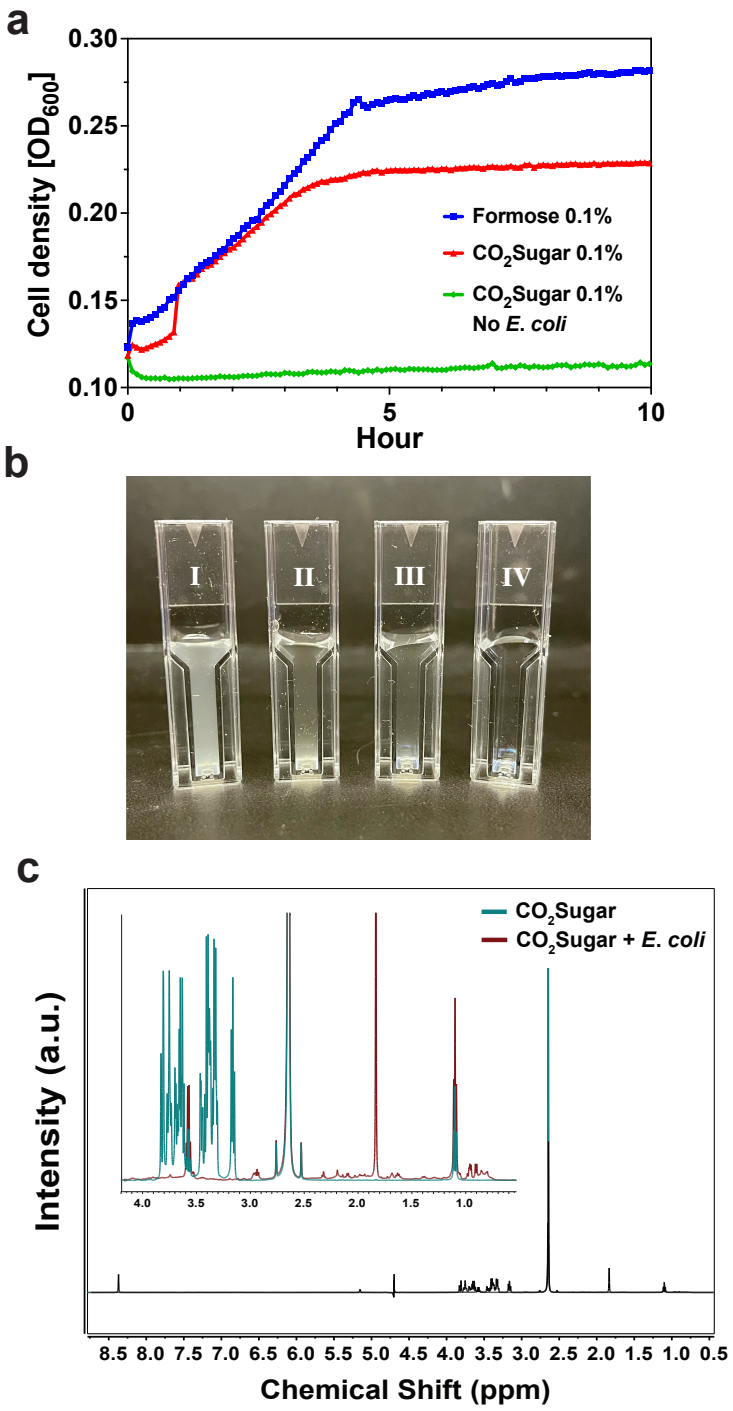


Figure 5.5 Utilization of CO_2Sugar as a bacterial feedstock. (a) Optical density measurements of *Escherichia coli* (*E. coli*) cultured with formose sugars (blue) and CO_2Sugars (red). Control is CO_2Sugars without *E. coli* (green). (b) Picture comparing the visual differences between *E. coli* cultures provided with different sugars. From left to right: I. glucose, II. formose sugars, III. CO_2Sugars, and IV. CO_2Sugars without *E. coli*. (c) ^{1}H-NMR spectra of CO_2Sugar containing minimal medium pre- and post-*E. coli* culture growth. Inset shows magnified 1-4 ppm region.

References

1. Cestellos-Blanco, S., Zhang, H., Kim, J. M., Shen, Y. & Yang, P. Photosynthetic semiconductor biohybrids for solar-driven biocatalysis. *Nature Catalysis* **3**, 245–255 (2020).
2. Sellers, P. J. *et al.* Comparison of radiative and physiological effects of doubled atmospheric CO2 on climate. *Science (1979)* **271**, 1402–1406 (1996).
3. Barber, J. Photosynthetic energy conversion: natural and artificial. *Chem. Soc. Rev.* **38**, 185–196 (2009).
4. Lewis, N. S. Research opportunities to advance solar energy utilization. *Science (1979)* **351**, aad1920 (2016).
5. Cook, T. R. *et al.* Solar energy supply and storage for the legacy and nonlegacy worlds. *Chemical Reviews* **110**, 6474–6502 (2010).
6. Nelson, N. & Ben-Shem, A. The complex architecture of oxygenic photosynthesis. *Nature Reviews Molecular Cell Biology* **5**, 971–982 (2004).
7. Williams, P. J. L. B. & Laurens, L. M. L. Microalgae as biodiesel & biomass feedstocks: Review & analysis of the biochemistry, energetics & economics. *Energy and Environmental Science* **3**, 554–590 (2010).
8. Hill, J., Nelson, E., Tilman, D., Polasky, S. & Tiffany, D. Environmental, economic, and energetic costs and benefits of biodiesel and ethanol biofuels. *Proc Natl Acad Sci U S A* **103**, 11206–10 (2006).
9. Zhu, X.-G., Long, S. P. & Ort, D. R. Improving Photosynthetic Efficiency for Greater Yield. *Annual Review of Plant Biology* **61**, 235–261 (2010).
10. Green, M. A. *et al.* Solar cell efficiency tables (Version 53). *Progress in Photovoltaics: Research and Applications* **27**, 3–12 (2019).
11. Blankenship, R. E. *et al. Comparing photosynthetic and photovoltaic efficiencies and recognizing the potential for improvement*. *Science* vol. 332 (2011).
12. Luo, J. *et al.* Water photolysis at 12.3% efficiency via perovskite photovoltaics and Earth-abundant catalysts. *Science (1979)* **345**, 1593–1596 (2014).
13. Zhu, X. G., Long, S. P. & Ort, D. R. What is the maximum efficiency with which photosynthesis can convert solar energy into biomass? *Current Opinion in Biotechnology* **19**, 153–159 (2008).
14. Mao, J., Li, K. & Peng, T. Recent advances in the photocatalytic CO2 reduction over semiconductors. *Catalysis Science and Technology* **3**, 2481–2498 (2013).
15. Ross, M. B. *et al.* Designing materials for electrochemical carbon dioxide recycling. *Nature Catalysis* **2**, 648–658 (2019).
16. Barton, E. E., Rampulla, D. M. & Bocarsly, A. B. Selective solar-driven reduction of CO2 to methanol using a catalyzed p-GaP based photoelectrochemical cell. *J Am Chem Soc* **130**, 6342–6344 (2008).
17. Sahara, G. *et al.* Photoelectrochemical Reduction of CO2 Coupled to Water Oxidation Using a Photocathode with a Ru(II)-Re(I) Complex Photocatalyst and a CoOx/TaON Photoanode. *J Am Chem Soc* **138**, 14152–14158 (2016).
18. Zhou, X. *et al.* Solar-Driven Reduction of 1 atm of CO2 to Formate at 10% Energy-Conversion Efficiency by Use of a TiO2-Protected III-V Tandem Photoanode in Conjunction with a Bipolar Membrane and a Pd/C Cathode. *ACS Energy Letters* **1**, 764–770 (2016).

19. Kim, D., Sakimoto, K. K., Hong, D. & Yang, P. Artificial photosynthesis for sustainable fuel and chemical production. *Angewandte Chemie - International Edition* **54**, 3259–3266 (2015).
20. Yoshikawa, K. *et al.* Silicon heterojunction solar cell with interdigitated back contacts for a photoconversion efficiency over 26%. *Nature Energy* **2**, 17032 (2017).
21. Chang, X., Wang, T. & Gong, J. CO2photo-reduction: Insights into CO2activation and reaction on surfaces of photocatalysts. *Energy and Environmental Science* **9**, 2177–2196 (2016).
22. Kong, Q. *et al.* Directed Assembly of Nanoparticle Catalysts on Nanowire Photoelectrodes for Photoelectrochemical CO2 Reduction. *Nano Letters* **16**, 5675–5680 (2016).
23. Varela, A. S., Ju, W., Reier, T. & Strasser, P. Tuning the Catalytic Activity and Selectivity of Cu for CO $_2$ Electroreduction in the Presence of Halides. *ACS Catalysis* **6**, 2136–2144 (2016).
24. Das, A. & Ljungdahl, L. G. Electron-Transport System in Acetogens. in *Biochemistry and Physiology of Anaerobic Bacteria* 191–204 (Springer-Verlag, 2006). doi:10.1007/0-387-22731-8_14.
25. Liang, J.-Y. & Lipscomb, W. N. *Binding of substrate CO2 to the active site of human carbonic anhydrase II: A molecular dynamics study (zinc enzyme/binding pathway/enzyme-substrate interaction)*. *Proc. Nati. Acad. Sci. USA* vol. 87 (1990).
26. Gray, H. B. & Winkler, J. R. Electron Transfer in Proteins. *Annual Review of Biochemistry* **65**, 537–561 (1996).
27. Cooney, M. J., Svoboda, V., Lau, C., Martin, G. & Minteer, S. D. Enzyme catalysed biofuel cells. *Energy and Environmental Science* **1**, 320–337 (2008).
28. Schlager, S. *et al.* Electrochemical Reduction of Carbon Dioxide to Methanol by Direct Injection of Electrons into Immobilized Enzymes on a Modified Electrode. *ChemSusChem* **9**, 631–635 (2016).
29. Lamle, S. E., Vincent, K. A., Halliwell, L. M., Albracht, S. P. J. & Armstrong, F. A. Hydrogenase on an electrode: A remarkable heterogeneous catalyst. *Journal of the Chemical Society. Dalton Transactions* **3**, 4152–4157 (2003).
30. Pinyou, P., Blay, V., Muresan, L. M. & Noguer, T. Enzyme-modified electrodes for biosensors and biofuel cells. *Materials Horizons* **6**, 1336–1358 (2019).
31. Kornienko, N., Zhang, J. Z., Sakimoto, K. K., Yang, P. & Reisner, E. Interfacing nature's catalytic machinery with synthetic materials for semi-artificial photosynthesis. *Nature Nanotechnology* **13**, 890–899 (2018).
32. Sarma, A. K., Vatsyayan, P., Goswami, P. & Minteer, S. D. Recent advances in material science for developing enzyme electrodes. *Biosensors and Bioelectronics* **24**, 2313–2322 (2009).
33. Sakimoto, K. K. *et al.* Physical Biology of the Materials-Microorganism Interface. *J Am Chem Soc* **140**, 1978–1985 (2018).
34. Rabaey, K. & Rozendal, R. A. Microbial electrosynthesis — revisiting the electrical route for microbial production. *Nature Reviews Microbiology* **8**, 706–716 (2010).
35. Shi, L. *et al.* Extracellular electron transfer mechanisms between microorganisms and minerals. *Nature Reviews Microbiology* **14**, 651–662 (2016).

36. Nevin, K. P., Woodard, T. L., Franks, A. E., Summers, Z. M. & Lovley, D. R. Microbial Electrosynthesis: Feeding Microbes Electricity To Convert Carbon Dioxide and Water to Multicarbon Extracellular Organic Compounds. *mBio* **1**, (2010).
37. Ragsdale, S. W. & Pierce, E. Acetogenesis and the Wood-Ljungdahl pathway of CO(2) fixation. *Biochim Biophys Acta* **1784**, 1873–98 (2008).
38. Aryal, N., Halder, A., Tremblay, P. L., Chi, Q. & Zhang, T. Enhanced microbial electrosynthesis with three-dimensional graphene functionalized cathodes fabricated via solvothermal synthesis. *Electrochimica Acta* **217**, 117–122 (2016).
39. Su, L. & Ajo-Franklin, C. M. Reaching full potential: bioelectrochemical systems for storing renewable energy in chemical bonds. *Current Opinion in Biotechnology* **57**, 66–72 (2019).
40. Zhang, T. *et al.* Improved cathode materials for microbial electrosynthesis. *Energy and Environmental Science* **6**, 217–224 (2013).
41. Tremblay, P. L., Höglund, D., Koza, A., Bonde, I. & Zhang, T. Adaptation of the autotrophic acetogen Sporomusa ovata to methanol accelerates the conversion of CO2 to organic products. *Scientific Reports* **5**, 16168 (2015).
42. Marshall, C. W., Ross, D. E., Fichot, E. B., Norman, R. S. & May, H. D. Long-term operation of microbial electrosynthesis systems improves acetate production by autotrophic microbiomes. *Environmental Science and Technology* **47**, 6023–6029 (2013).
43. Li, H. *et al.* Integrated electromicrobial conversion of CO2to higher alcohols. *Science (1979)* **335**, 1596 (2012).
44. Liu, C. *et al.* Nanowire-bacteria hybrids for unassisted solar carbon dioxide fixation to value-added chemicals. *Nano Letters* **15**, 3634–3639 (2015).
45. Shively, J. M., van Keulen, G. & Meijer, W. G. SOMETHING FROM ALMOST NOTHING: Carbon Dioxide Fixation in Chemoautotrophs. *Annual Review of Microbiology* **52**, 191–230 (1998).
46. Wang, H. & Ren, Z. J. A comprehensive review of microbial electrochemical systems as a platform technology. *Biotechnology Advances* **31**, 1796–1807 (2013).
47. Nichols, E. M. *et al.* Hybrid bioinorganic approach to solar-to-chemical conversion. *Proc Natl Acad Sci U S A* **112**, 11461–6 (2015).
48. Liu, C., Colón, B. C., Ziesack, M., Silver, P. A. & Nocera, D. G. Water splitting–biosynthetic system with CO2 reduction efficiencies exceeding photosynthesis. *Science (1979)* **352**, 1210–1213 (2016).
49. Dogutan, D. K. & Nocera, D. G. Artificial Photosynthesis at Efficiencies Greatly Exceeding That of Natural Photosynthesis. *Accounts of Chemical Research* **52**, 3143–3148 (2019).
50. Liu, C., Sakimoto, K. K., Colón, B. C., Silver, P. A. & Nocera, D. G. Ambient nitrogen reduction cycle using a hybrid inorganic–biological system. *Proceedings of the National Academy of Sciences* **114**, 6450–6455 (2017).
51. Rodrigues, R. M. *et al.* Perfluorocarbon nanoemulsion promotes the delivery of reducing equivalents for electricity-driven microbial CO 2 reduction. *Nature Catalysis* **2**, 407–414 (2019).
52. Lovley, D. R. & Nevin, K. P. Electrobiocommodities: powering microbial production of fuels and commodity chemicals from carbon dioxide with electricity. *Current Opinion in Biotechnology* **24**, 385–390 (2013).
53. Lovley, D. R. Electromicrobiology. *Annu. Rev. Microbiol* **66**, 391–409 (2012).

54. Virdis, B. *et al.* Analysis of electron transfer dynamics in mixed community electroactive microbial biofilms. *RSC Advances* **6**, 3650–3660 (2016).
55. Kracke, F., Vassilev, I. & Krömer, J. O. Microbial electron transport and energy conservation - The foundation for optimizing bioelectrochemical systems. *Frontiers in Microbiology* **6**, 575 (2015).
56. Light, S. H. *et al.* A flavin-based extracellular electron transfer mechanism in diverse Gram-positive bacteria. *Nature* **562**, 140–157 (2018).
57. Fukushima, T. *et al.* The Molecular Basis for Binding of an Electron Transfer Protein to a Metal Oxide Surface. *J Am Chem Soc* **139**, 12647–12654 (2017).
58. Deutzmann, J. S., Sahin, M. & Spormann, A. M. Extracellular enzymes facilitate electron uptake in biocorrosion and bioelectrosynthesis. *mBio* **6**, 1–8 (2015).
59. Reguera, G. *et al.* Extracellular electron transfer via microbial nanowires. *Nature* **435**, 1098–1101 (2005).
60. Wang, F. *et al.* Structure of Microbial Nanowires Reveals Stacked Hemes that Transport Electrons over Micrometers. *Cell* **177**, 361-369.e10 (2019).
61. Kornienko, N. *et al.* Spectroscopic elucidation of energy transfer in hybrid inorganic-biological organisms for solar-to-chemical production. *Proc Natl Acad Sci U S A* **113**, 11750–11755 (2016).
62. Zhang, R. *et al.* Proteomic and Metabolic Elucidation of Solar-Powered Biomanufacturing by Bio-Abiotic Hybrid System. *Chem* (2019) doi:10.1016/j.chempr.2019.11.002.
63. Robertson, S. J., Grattieri, M., Behring, J., Bestetti, M. & Minteer, S. D. Transitioning from batch to flow hypersaline microbial fuel cells. *Electrochimica Acta* **317**, 494–501 (2019).
64. Guo, J. *et al. Light-driven fine chemical production in yeast biohybrids*. *Science* vol. 362 (2018).
65. Smith, M. J. & Francis, M. B. A Designed A. vinelandii-S. elongatus Coculture for Chemical Photoproduction from Air, Water, Phosphate, and Trace Metals. *ACS Synthetic Biology* **5**, 955–961 (2016).
66. Angelis, S. *et al.* Co-culture of microalgae, cyanobacteria, and macromycetes for exopolysaccharides production: Process preliminary optimization and partial characterization. *Applied Biochemistry and Biotechnology* **167**, 1092–1106 (2012).
67. Marshall, C. W., Ross, D. E., Fichot, E. B., Norman, R. S. & May, H. D. Electrosynthesis of commodity chemicals by an autotrophic microbial community. *Applied and Environmental Microbiology* **78**, 8412–8420 (2012).
68. Jia, J. *et al.* Solar water splitting by photovoltaic-electrolysis with a solar-to-hydrogen efficiency over 30%. *Nature Communications* **7**, 13237 (2016).
69. McNeely, K., Xu, Y., Bennette, N., Bryant, D. A. & Dismukes, G. C. Redirecting reductant flux into hydrogen production via metabolic engineering of fermentative carbon metabolism in a cyanobacterium. *Applied and Environmental Microbiology* **76**, 5032–5038 (2010).
70. Atsumi, S., Higashide, W. & Liao, J. C. Direct photosynthetic recycling of carbon dioxide to isobutyraldehyde. *Nature Biotechnology* **27**, 1177–1180 (2009).
71. Antonovsky, N. *et al.* Sugar Synthesis from CO2 in Escherichia coli. *Cell* **166**, 115–125 (2016).
72. Kung, Y., Runguphan, W. & Keasling, J. D. From fields to fuels: Recent advances in the microbial production of biofuels. *ACS Synthetic Biology* **1**, 498–513 (2012).

73. Liao, J. C., Mi, L., Pontrelli, S. & Luo, S. Fuelling the future: Microbial engineering for the production of sustainable biofuels. *Nature Reviews Microbiology* **14**, 288–304 (2016).
74. Lu, Z.-X. *et al.* Cell Damage Induced by Photocatalysis of TiO 2 Thin Films. *Langmuir* **19**, 8765–8768 (2003).
75. Chan, C. H., Levar, C. E., Jiménez-Otero, F. & Bond, D. R. Genome Scale Mutational Analysis of Geobacter sulfurreducens Reveals Distinct Molecular Mechanisms for Respiration and Sensing of Poised Electrodes versus Fe(III) Oxides. *J Bacteriol* **199**, e00340-17 (2017).
76. Ha, C.-S. & Gardella, J. A. Surface Chemistry of Biodegradable Polymers for Drug Delivery Systems. *Chemical Reviews* **105**, 4205–4232 (2005).
77. Su, Y. *et al.* Close-Packed Nanowire-Bacteria Hybrids for Efficient Solar-Driven CO2 Fixation. *Joule* **4**, 800–811 (2020).
78. Chiappini, C. *et al.* Biodegradable silicon nanoneedles delivering nucleic acids intracellularly induce localized in vivo neovascularization. *Nature Materials* **14**, 532–539 (2015).
79. Sharei, A. *et al.* A vector-free microfluidic platform for intracellular delivery. *Proc Natl Acad Sci U S A* **110**, 2082–2087 (2013).
80. Tian, B. *et al.* Three-dimensional, flexible nanoscale field-effect transistors as localized bioprobes. *Science (1979)* **329**, 830–834 (2010).
81. Xie, C., Lin, Z., Hanson, L., Cui, Y. & Cui, B. Intracellular recording of action potentials by nanopillar electroporation. *Nature Nanotechnology 2012 7:3* **7**, 185–190 (2012).
82. Logan, B. E. Exoelectrogenic bacteria that power microbial fuel cells. *Nature Reviews Microbiology* **7**, 375–381 (2009).
83. Lovley, D. R. Bug juice: Harvesting electricity with microorganisms. *Nature Reviews Microbiology* vol. 4 497–508 (2006).
84. Sakimoto, K. K., Wong, A. B. & Yang, P. Self-photosensitization of nonphotosynthetic bacteria for solar-to-chemical production. *Science (1979)* **351**, 74–77 (2016).
85. Zhang, H. *et al.* Bacteria photosensitized by intracellular gold nanoclusters for solar fuel production. *Nature Nanotechnology* **13**, 900–905 (2018).
86. Nichols, E. M. *et al.* Hybrid bioinorganic approach to solar-to-chemical conversion. *Proceedings of the National Academy of Sciences* **112**, 11461–11466 (2015).
87. Liu, C., Colón, B. C., Ziesack, M., Silver, P. A. & Nocera, D. G. Water splitting-biosynthetic system with CO2 reduction efficiencies exceeding photosynthesis. *Science (1979)* **352**, 1210–1213 (2016).
88. Zhang, T. More efficient together. *Science (1979)* **350**, 738–739 (2015).
89. Liu, C. *et al.* Nanowire-bacteria hybrids for unassisted solar carbon dioxide fixation to value-added chemicals. *Nano Letters* **15**, 3634–3639 (2015).
90. Rabaey, K. & Rozendal, R. A. Microbial electrosynthesis — revisiting the electrical route for microbial production. *Nature Reviews Microbiology 2010 8:10* **8**, 706–716 (2010).
91. Lewis, N. S. & Nocera, D. G. Powering the planet: Chemical challenges in solar energy utilization. *Proc Natl Acad Sci U S A* **103**, 15729–15735 (2006).
92. Cui, M., Nie, H., Zhang, T., Lovley, D. & Russell, T. P. Three-dimensional hierarchical metal oxide-carbon electrode materials for highly efficient microbial electrosynthesis. *Sustainable Energy and Fuels* **1**, 1171–1176 (2017).
93. Zhang, T. *et al.* Improved cathode materials for microbial electrosynthesis. *Energy and Environmental Science* **6**, 217–224 (2013).

94. Ammam, F., Tremblay, P. L., Lizak, D. M. & Zhang, T. Effect of tungstate on acetate and ethanol production by the electrosynthetic bacterium Sporomusa ovata. *Biotechnology for Biofuels* **9**, 163 (2016).
95. Patil, S. A. *et al.* Selective Enrichment Establishes a Stable Performing Community for Microbial Electrosynthesis of Acetate from CO2. *Environmental Science and Technology* **49**, 8833–8843 (2015).
96. Su, Y. *et al.* Single-nanowire photoelectrochemistry. *Nature Nanotechnology* **11**, 609–612 (2016).
97. Liu, M. *et al.* Enhanced electrocatalytic CO2 reduction via field-induced reagent concentration. *Nature 2016 537:7620* **537**, 382–386 (2016).
98. LaBelle, E. v. & May, H. D. Energy efficiency and productivity enhancement of microbial electrosynthesis of acetate. *Frontiers in Microbiology* **8**, 756 (2017).
99. Jourdin, L., Freguia, S., Flexer, V. & Keller, J. Bringing High-Rate, CO2-Based Microbial Electrosynthesis Closer to Practical Implementation through Improved Electrode Design and Operating Conditions. *Environmental Science and Technology* **50**, 1982–1989 (2016).
100. Mohanakrishna, G., Seelam, J. S., Vanbroekhoven, K. & Pant, D. An enriched electroactive homoacetogenic biocathode for the microbial electrosynthesis of acetate through carbon dioxide reduction. *Faraday Discussions* **183**, 445–462 (2015).
101. Qu, F., Li, N. B. & Luo, H. Q. Highly sensitive fluorescent and colorimetric pH sensor based on polyethylenimine-capped silver nanoclusters. *Langmuir* **29**, 1199–1205 (2013).
102. Möller, B., Oßmer, R., Howard, B. H., Gottschalk, G. & Hippe, H. Sporomusa, a new genus of gram-negative anaerobic bacteria including Sporomusa sphaeroides spec. nov. and Sporomusa ovata spec. nov. *Archives of Microbiology 1984 139:4* **139**, 388–396 (1984).
103. Holmberg, J. P., Ahlberg, E., Bergenholtz, J., Hassellöv, M. & Abbas, Z. Surface charge and interfacial potential of titanium dioxide nanoparticles: Experimental and theoretical investigations. *Journal of Colloid and Interface Science* **407**, 168–176 (2013).
104. Sára, M. & Sleytr, U. B. S-layer proteins. *Journal of Bacteriology* **182**, 859–868 (2000).
105. Beveridge, T. J. Structures of gram-negative cell walls and their derived membrane vesicles. *Journal of Bacteriology* **181**, 4725–4733 (1999).
106. Blanchet, E. *et al.* Importance of the hydrogen route in up-scaling electrosynthesis for microbial CO2 reduction. *Energy and Environmental Science* **8**, 3731–3744 (2015).
107. Chadwick, G. L., Otero, F. J., Gralnick, J. A., Bond, D. R. & Orphan, V. J. NanoSIMS imaging reveals metabolic stratification within current-producing biofilms. *Proc Natl Acad Sci U S A* **116**, 20716–20724 (2019).
108. Zhang, J. Z. *et al.* Photoelectrochemistry of Photosystem II in Vitro vs in Vivo. *J Am Chem Soc* **140**, 6–9 (2018).
109. Cestellos-Blanco, S. *et al.* Production of PHB from CO2-derived acetate with minimal processing assessed for space biomanufacturing. *Frontiers in Microbiology* **12**, 2126 (2021).
110. ISECG. *The Global Exploration Roadmap January 2018*. (2018).
111. Council, N. R. *Recapturing a Future for Space Exploration: Life and Physical Sciences Research for a New Era*. *Recapturing a Future for Space Exploration: Life and Physical Sciences Research for a New Era* (National Academies Press, 2012). doi:10.17226/13048.
112. Council, N. R. *Pathways to exploration: Rationales and approaches for a U.S. Program of Human Space Exploration*. *Pathways to Exploration: Rationales and Approaches for a*

U.S. Program of Human Space Exploration (National Academies Press, 2014). doi:10.17226/18801.
113. Nasa Headquarters, O. of the C. F. O. *FY 2021 Volume of Integrated Performance*. (2019).
114. NASA. *NASA 2018 Strategic Plan*. (2018).
115. Northon, K. NASA Selects Proposals for First Space Technology Research Institutes. https://www.nasa.gov/press-release/nasa-selects-proposals-for-first-ever-space-technology-research-institutes (2017).
116. Wertz, J. R. & Larson, W. *Reducing Space Mission Cost*. (Microcrosm Press).
117. Linck, E. *et al. Evaluation of a Human Mission to Mars by 2033*. (2019).
118. Moore, C. L. Technology development for human exploration of Mars. *Acta Astronautica* **67**, 1170–1175 (2010).
119. Tanner, C., Young, J., Thompson, R. & Wilhite, A. *On-Orbit Propellant Resupply Options for Mars Exploration Architectures*. (2006).
120. Linne, D. L. *et al. Overview of NASA Technology Development for In-Situ Resource Utilization (ISRU)*. *68 th International Astronautical Congress (IAC)* (2017).
121. Berliner, A. J. *et al.* Towards a Biomanufactory on Mars. 1–20 (2020) doi:10.20944/preprints202012.0714.v1.
122. Menezes, A. A. *Realizing a Self-Reproducing Space Factory with Engineered and Programmed Biology*. *LPICo* vol. 2063 (2018).
123. Nangle, S. N. *et al.* The case for biotech on Mars. *Nature Biotechnology* vol. 38 401–407 (2020).
124. Owen, T. *et al.* The composition of the atmosphere at the surface of Mars. *Journal of Geophysical Research* **82**, 4635–4639 (1977).
125. Soundararajan, M. *et al.* Phototrophic N2 and CO2 Fixation Using a Rhodopseudomonas palustris-H2 Mediated Electrochemical System With Infrared Photons. *Frontiers in Microbiology* **10**, 1817 (2019).
126. Kobayashi, M. & Kobayashi, M. Waste Remediation and Treatment Using Anoxygenic Phototrophic Bacteria. in *Anoxygenic Photosynthetic Bacteria* 1269–1282 (Kluwer Academic Publishers, 2006). doi:10.1007/0-306-47954-0_62.
127. Cestellos-Blanco, S., Zhang, H., Kim, J. M., Shen, Y. xiao & Yang, P. Photosynthetic semiconductor biohybrids for solar-driven biocatalysis. *Nature Catalysis* vol. 3 245–255 (2020).
128. Sudesh, K., Abe, H. & Doi, Y. Synthesis, structure and properties of polyhydroxyalkanoates: Biological polyesters. *Progress in Polymer Science (Oxford)* vol. 25 1503–1555 (2000).
129. Müller-Santos, M. *et al.* The protective role of PHB and its degradation products against stress situations in bacteria. *FEMS Microbiology Reviews* **058**, 1–13 (2020).
130. Koller, M. Polyhydroxyalkanoate biosynthesis at the edge of water activitiy-haloarchaea as biopolyester factories. *Bioengineering* vol. 6 (2019).
131. Dalsasso, R. R., Pavan, F. A., Bordignon, S. E., Aragão, G. M. F. de & Poletto, P. Polyhydroxybutyrate (PHB) production by Cupriavidus necator from sugarcane vinasse and molasses as mixed substrate. *Process Biochemistry* **85**, 12–18 (2019).
132. Sheu, D. S., Chen, W. M., Yang, J. Y. & Chang, R. C. Thermophilic bacterium Caldimonas taiwanensis produces poly(3-hydroxybutyrate-co-3-hydroxyvalerate) from

starch and valerate as carbon sources. *Enzyme and Microbial Technology* **44**, 289–294 (2009).
133. Obruca, S., Sedlacek, P., Koller, M., Kucera, D. & Pernicova, I. Involvement of polyhydroxyalkanoates in stress resistance of microbial cells: Biotechnological consequences and applications. *Biotechnology Advances* vol. 36 856–870 (2018).
134. Meereboer, K. W., Misra, M. & Mohanty, A. K. Review of recent advances in the biodegradability of polyhydroxyalkanoate (PHA) bioplastics and their composites. *Green Chemistry* vol. 22 5519–5558 (2020).
135. McAdam, B., Fournet, M. B., McDonald, P. & Mojicevic, M. Production of polyhydroxybutyrate (PHB) and factors impacting its chemical and mechanical characteristics. *Polymers* vol. 12 1–20 (2020).
136. Vigil Fuentes, M. A. *et al.* Study on the 3D printability of poly(3-hydroxybutyrate-co-3-hydroxyvalerate)/poly(lactic acid) blends with chain extender using fused filament fabrication. *Scientific Reports* **10**, 11804 (2020).
137. Alarfaj, A. A., Arshad, M., Sholkamy, E. N. & Munusamy, M. A. Extraction and characterization of polyhydroxybutyrates (PHB) from Bacillus thuringiensis KSADL127 isolated from mangrove environments of Saudi Arabia. *Brazilian Archives of Biology and Technology* **58**, 781–788 (2015).
138. Kovalcik, A. Recent Advances in 3D Printing of Polyhydroxyalkanoates: A Review. *The EuroBiotech Journal* **5**, 48–55 (2021).
139. Fernández-Naveira, Á., Abubackar, H. N., Veiga, M. C. & Kennes, C. Production of chemicals from C1 gases (CO, CO2) by Clostridium carboxidivorans. *World Journal of Microbiology and Biotechnology* **33**, 43 (2017).
140. Nevin, K. P. *et al.* Electrosynthesis of organic compounds from carbon dioxide is catalyzed by a diversity of acetogenic microorganisms. *Applied and Environmental Microbiology* **77**, 2882–2886 (2011).
141. Friman, H., Schechter, A., Ioffe, Y., Nitzan, Y. & Cahan, R. Current production in a microbial fuel cell using a pure culture of Cupriavidus basilensis growing in acetate or phenol as a carbon source. *Microbial Biotechnology* **6**, 425–434 (2013).
142. Wierckx, N., Koopman, F., Bandounas, L., De Winde, J. H. & Ruijssenaars, H. J. Isolation and characterization of Cupriavidus basilensis HMF14 for biological removal of inhibitors from lignocellulosic hydrolysatembt. *Microbial Biotechnology* **3**, 336–343 (2010).
143. Pepè Sciarria, T. *et al.* Bio-electrorecycling of carbon dioxide into bioplastics. *Green Chemistry* **20**, 4058–4066 (2018).
144. Kiefer, D., Merkel, M., Lilge, L., Henkel, M. & Hausmann, R. From Acetate to Bio-Based Products: Underexploited Potential for Industrial Biotechnology. *Trends in Biotechnology* vol. 39 397–411 (2021).
145. Fast, A. G. & Papoutsakis, E. T. Stoichiometric and energetic analyses of non-photosynthetic CO 2-fixation pathways to support synthetic biology strategies for production of fuels and chemicals. *Current Opinion in Chemical Engineering* **1**, 380–395 (2012).
146. Ray, J. *et al.* Complete genome sequence of Cupriavidus basilensis 4G11, isolated from the Oak Ridge Field Research Center site. *Genome Announcements* **3**, 322–337 (2015).

147. Tyo, K. E., Zhou, H. & Stephanopoulos, G. N. High-throughput screen for poly-3-hydroxybutyrate in Escherichia coli and synechocystis sp. strain PCC6803. *Applied and Environmental Microbiology* **72**, 3412–3417 (2006).
148. Harvey W. Blanch, D. S. C. Biochemical Engineering, Second Edition. *CRC Press, - Science* 280–282 https://books.google.ca/books?id=ST_p2AOApZsC&printsec=frontcover&redir_esc=y#v=onepage&q&f=false (1997).
149. Mozumder, M. S. I., De Wever, H., Volcke, E. I. P. & Garcia-Gonzalez, L. A robust fed-batch feeding strategy independent of the carbon source for optimal polyhydroxybutyrate production. *Process Biochemistry* **49**, 365–373 (2014).
150. Wood, J. M. Bacterial responses to osmotic challenges. *Journal of General Physiology* vol. 145 381–388 (2015).
151. Aryal, N., Tremblay, P. L., Lizak, D. M. & Zhang, T. Performance of different Sporomusa species for the microbial electrosynthesis of acetate from carbon dioxide. *Bioresource Technology* **233**, 184–190 (2017).
152. Kedia, G., Passanha, P., Dinsdale, R. M., Guwy, A. J. & Esteves, S. R. Evaluation of feeding regimes to enhance PHA production using acetic and butyric acids by a pure culture of Cupriavidus necator. *Biotechnology and Bioprocess Engineering* **19**, 989–995 (2014).
153. Jeevarajan, A. S., Vani, S., Taylor, T. D. & Anderson, M. M. Continuous pH monitoring in a perfused bioreactor system using an optical pH sensor. *Biotechnology and Bioengineering* **78**, 467–472 (2002).
154. Menezes, A. A., Cumbers, J., Hogan, J. A. & Arkin, A. P. Towards synthetic biological approaches to resource utilization on space missions. *Journal of the Royal Society Interface* **12**, (2015).
155. Atlić, A. *et al.* Continuous production of poly([R]-3-hydroxybutyrate) by Cupriavidus necator in a multistage bioreactor cascade. *Applied Microbiology and Biotechnology* **91**, 295–304 (2011).
156. Li, M., Eskridge, K., Liu, E. & Wilkins, M. Enhancement of polyhydroxybutyrate (PHB) production by 10-fold from alkaline pretreatment liquor with an oxidative enzyme-mediator-surfactant system under Plackett-Burman and central composite designs. *Bioresource Technology* **281**, 99–106 (2019).
157. Li, M. & Wilkins, M. Fed-batch cultivation and adding supplements to increase yields of polyhydroxybutyrate production by Cupriavidus necator from corn stover alkaline pretreatment liquor. *Bioresource Technology* **299**, 122676 (2020).
158. Erisman, J. W., Sutton, M. A., Galloway, J., Klimont, Z. & Winiwarter, W. How a century of ammonia synthesis changed the world. *Nature Geoscience* **1**, 636–639 (2008).
159. Kim, D., Sakimoto, K. K., Hong, D. & Yang, P. Artificial Photosynthesis for Sustainable Fuel and Chemical Production. *Angewandte Chemie International Edition* **54**, 3259–3266 (2015).
160. Chen, H., Dong, F. & Minteer, S. D. The progress and outlook of bioelectrocatalysis for the production of chemicals, fuels and materials. *Nature Catalysis* vol. 3 225–244 (2020).
161. Haas, T., Krause, R., Weber, R., Demler, M. & Schmid, G. Technical photosynthesis involving CO2 electrolysis and fermentation. *Nature Catalysis* **1**, 32–39 (2018).
162. Rabaey, K. & Rozendal, R. A. Microbial electrosynthesis — revisiting the electrical route for microbial production. *Nature Reviews Microbiology* **8**, 706–716 (2010).

163. Claassens, N. J., Sousa, D. Z., Dos Santos, V. A. P. M., De Vos, W. M. & Van Der Oost, J. Harnessing the power of microbial autotrophy. *Nature Reviews Microbiology* vol. 14 692–706 (2016).
164. He, J. & Janáky, C. Recent Advances in Solar-Driven Carbon Dioxide Conversion: Expectations versus Reality. *ACS Energy Letters* **5**, 1996–2014 (2020).
165. Huang, H. *et al.* CRISPR/Cas9-Based Efficient Genome Editing in Clostridium ljungdahlii, an Autotrophic Gas-Fermenting Bacterium. *ACS Synthetic Biology* **5**, 1355–1361 (2016).
166. Ripatti, D. S., Veltman, T. R. & Kanan, M. W. Carbon Monoxide Gas Diffusion Electrolysis that Produces Concentrated C 2 Products with High Single-Pass Conversion. *Joule* **3**, 240–256 (2019).
167. Prévoteau, A., Carvajal-Arroyo, J. M., Ganigué, R. & Rabaey, K. Microbial electrosynthesis from CO2: forever a promise? *Current Opinion in Biotechnology* vol. 62 48–57 (2020).
168. Molitor, B., Mishra, A. & Angenent, L. T. Power-to-protein: Converting renewable electric power and carbon dioxide into single cell protein with a two-stage bioprocess. *Energy and Environmental Science* **12**, 3515–3521 (2019).
169. Hu, P. *et al.* Integrated bioprocess for conversion of gaseous substrates to liquids. *Proc Natl Acad Sci U S A* **113**, 3773–3778 (2016).
170. Liu, X. *et al.* Syntrophic interspecies electron transfer drives carbon fixation and growth by Rhodopseudomonas palustris under dark, anoxic conditions. *Science Advances* **7**, eabh1852 (2021).
171. Labelle, E. V., Marshall, C. W. & May, H. D. Microbiome for the Electrosynthesis of Chemicals from Carbon Dioxide. *Accounts of Chemical Research* **53**, 62–71 (2020).
172. Fang, X., Kalathil, S., Divitini, G., Wang, Q. & Reisner, E. A three-dimensional hybrid electrode with electroactive microbes for efficient electrogenesis and chemical synthesis. *Proc Natl Acad Sci U S A* **117**, 5074–5080 (2020).
173. MacFarlane, D. R. *et al.* A Roadmap to the Ammonia Economy. *Joule* **4**, 1186–1205 (2020).
174. Smith, C. & Torrente-Murciano, L. The potential of green ammonia for agricultural and economic development in Sierra Leone. *One Earth* **4**, 104–113 (2021).
175. Soloveichik, G. Electrochemical synthesis of ammonia as a potential alternative to the Haber–Bosch process. *Nature Catalysis* vol. 2 377–380 (2019).
176. Hao, Y. C. *et al.* Promoting nitrogen electroreduction to ammonia with bismuth nanocrystals and potassium cations in water. *Nature Catalysis* **2**, 448–456 (2019).
177. Lazouski, N., Chung, M., Williams, K., Gala, M. L. & Manthiram, K. Non-aqueous gas diffusion electrodes for rapid ammonia synthesis from nitrogen and water-splitting-derived hydrogen. *Nature Catalysis* **3**, 463–469 (2020).
178. Singh, A. R. *et al.* Strategies toward Selective Electrochemical Ammonia Synthesis. *ACS Catalysis* **9**, 8316–8324 (2019).
179. Suryanto, B. H. R. *et al.* Challenges and prospects in the catalysis of electroreduction of nitrogen to ammonia. *Nature Catalysis* **2**, 290–296 (2019).
180. Liu, Y. *et al.* Facile Ammonia Synthesis from Electrocatalytic N2 Reduction under Ambient Conditions on N-Doped Porous Carbon. *ACS Catalysis* **8**, 1186–1191 (2018).

181. Zhang, K., Guo, R., Pang, F., He, J. & Zhang, W. Low-Coordinated Gold Atoms Boost Electrochemical Nitrogen Reduction Reaction under Ambient Conditions. *ACS Sustainable Chemistry and Engineering* **7**, 10214–10220 (2019).
182. Xue, Z. H. *et al.* Electrochemical Reduction of N2 into NH3 by Donor-Acceptor Couples of Ni and Au Nanoparticles with a 67.8% Faradaic Efficiency. *J Am Chem Soc* **141**, 14976–14980 (2019).
183. Lu, S. *et al.* Perfluorocarbon nanoemulsions create a beneficial O2 microenvironment in N2-fixing biological | inorganic hybrid. *Chem Catalysis* **1**, 704–720 (2021).
184. Lu, S., Guan, X. & Liu, C. Electricity-powered artificial root nodule. *Nature Communications 2020 11:1* **11**, 1–10 (2020).
185. Dong, F., Lee, Y. S., Gaffney, E. M., Liou, W. & Minteer, S. D. Engineering Cyanobacterium with Transmembrane Electron Transfer Ability for Bioelectrochemical Nitrogen Fixation. *ACS Catalysis* **11**, 13169–13179 (2021).
186. Rasche, M. E. & Arp, D. J. Hydrogen Inhibition of Nitrogen Reduction by Nitrogenase in Isolated Soybean Nodule Bacteroids'. *Plant Physiol* **91**, 663–668 (1989).
187. Burgess, B. K., Wherland, S., Newton, W. E. & Stiefel, E. I. Nitrogenase Reactivity: Insight into the Nitrogen-Fixing Process through Hydrogen-Inhibition and HD-Forming Reactions. *Biochemistry* **20**, 5140–5146 (1981).
188. Larimer, F. W. *et al.* Complete genome sequence of the metabolically versatile photosynthetic bacterium Rhodopseudomonas palustris. *Nature Biotechnology* **22**, 55–61 (2004).
189. Jiao, Y., Kappler, A., Croal, L. R. & Newman, D. K. Isolation and characterization of a genetically tractable photoautotrophic Fe(II)-oxidizing bacterium, Rhodopseudomonas palustris strain TIE-1. *Applied and Environmental Microbiology* **71**, 4487–4496 (2005).
190. McKinlay, J. B. & Harwood, C. S. Carbon dioxide fixation as a central redox cofactor recycling mechanism in bacteria. *Proc Natl Acad Sci U S A* **107**, 11669–11675 (2010).
191. Hu, H., Liang, Y., Li, S., Guo, Q. & Wu, C. A modified o -phthalaldehyde fluorometric analytical method for ultratrace ammonium in natural waters using edta-naoh as buffer. *Journal of Analytical Methods in Chemistry* **2014**, (2014).
192. Wang, B., Jiang, Z., Yu, J. C., Wang, J. & Wong, P. K. Enhanced CO 2 reduction and valuable C 2+ chemical production by a CdS-photosynthetic hybrid system . *Nanoscale* **11**, 9296–9301 (2019).
193. Gutschick, V. P. *Energetics of Microbial Fixation of Dinitrogen. Advances in Biochemical Engineering* (1982) doi:10.1007/3-540-11019-4_7.
194. Beringer, J. E., Brewin, N., Johnston, A. W. B., Schulman, H. M. & Hopwood, D. A. The Rhizobium-legume symbiosis. *Proceedings of the Royal Society of London - Biological Sciences* **204**, 219–233 (1979).
195. Schwember, A. R., Schulze, J., del Pozo, A. & Cabeza, R. A. Regulation of Symbiotic Nitrogen Fixation in Legume Root Nodules. *Plants* **8**, 333 (2019).
196. McKinlay, J. B. *et al.* Non-growing rhodopseudomonas palustris increases the hydrogen gas yield from acetate by shifting from the glyoxylate shunt to the tricarboxylic acid cycle. *Journal of Biological Chemistry* **289**, 1960–1970 (2014).
197. McKinlay, J. B. & Harwood, C. S. Carbon dioxide fixation as a central redox cofactor recycling mechanism in bacteria. *Proceedings of the National Academy of Sciences* **107**, 11669–11675 (2010).

198. Rey, F. E., Heiniger, E. K. & Harwood, C. S. Redirection of metabolism for biological hydrogen production. *Applied and Environmental Microbiology* **73**, 1665–1671 (2007).
199. Adessi, A., McKinlay, J. B., Harwood, C. S. & De Philippis, R. A Rhodopseudomonas palustris nifA* mutant produces H2 from NH 4 + -containing vegetable wastes. *International Journal of Hydrogen Energy* **37**, 15893–15900 (2012).
200. La Sarre, B., McCully, A. L., Lennon, J. T. & McKinlay, J. B. Microbial mutualism dynamics governed by dose-dependent toxicity of cross-fed nutrients. *ISME Journal* **11**, 337–348 (2017).
201. Ding, Y. *et al.* Nanorg Microbial Factories: Light-Driven Renewable Biochemical Synthesis Using Quantum Dot-Bacteria Nanobiohybrids. *J Am Chem Soc* **141**, 10272–10282 (2019).
202. LaSarre, B., McCully, A. L., Lennon, J. T. & McKinlay, J. B. Microbial mutualism dynamics governed by dose-dependent toxicity of cross-fed nutrients. *The ISME Journal* **11**, 337–348 (2017).
203. McKinlay, J. B. & Harwood, C. S. Calvin cycle flux, pathway constraints, and substrate oxidation state together determine the H2 biofuel yield in photoheterotrophic bacteria. *mBio* **2**, (2011).
204. Ranaivoarisoa, T. O., Singh, R., Rengasamy, K., Guzman, M. S. & Bose, A. Towards sustainable bioplastic production using the photoautotrophic bacterium Rhodopseudomonas palustris TIE-1. *Journal of Industrial Microbiology and Biotechnology* **46**, 1401–1417 (2019).
205. Zheng, Y. *et al.* A pathway for biological methane production using bacterial iron-only nitrogenase. *Nature Microbiology* **3**, 281–286 (2018).
206. Moller, B., Obmer, R., Howard, B. H., Gottsehalk, G. & Hippe, H. *Sporomusa, a new genus of gram-negative anaerobic bacteria including Sporomusa sphaeroides spec. nov. and Sporomusa ovata spec. nov. *. *Arch Mierobiol* vol. 139 (1984).
207. Liu, Q., Wu, L., Jackstell, R. & Beller, M. Using carbon dioxide as a building block in organic synthesis. *Nature Communications 2015 6:1* **6**, 1–15 (2015).
208. Alain Goeppert, Miklos Czaun, Prakash, G. K. S. & A. Olah, G. Air as the renewable carbon source of the future: an overview of CO 2 capture from the atmosphere. *Energy & Environmental Science* **5**, 7833–7853 (2012).
209. Hepburn, C. *et al.* The technological and economic prospects for CO2 utilization and removal. *Nature 2019 575:7781* **575**, 87–97 (2019).
210. Curtis V. Manning, Christopher P. McKay & Kevin J. Zahnle. Thick and thin models of the evolution of carbon dioxide on Mars. *Icarus* **180**, 38–59 (2006).
211. Muscatello, A. C. & Santiago-Maldonado, E. Mars In Situ Resource Utilization Technology Evaluation. doi:10.2514/6.2012-360.
212. Berliner, A. J. *et al.* Towards a Biomanufactory on Mars. *Frontiers in Astronomy and Space Sciences* **0**, 120 (2021).
213. Tackett, B. M., Gomez, E. & Chen, J. G. Net reduction of CO2 via its thermocatalytic and electrocatalytic transformation reactions in standard and hybrid processes. *Nature Catalysis 2019 2:5* **2**, 381–386 (2019).
214. Li, W. *et al.* A short review of recent advances in CO2 hydrogenation to hydrocarbons over heterogeneous catalysts. *RSC Advances* **8**, 7651–7669 (2018).

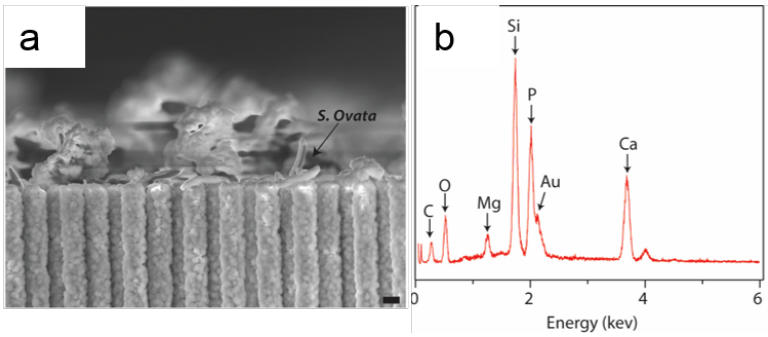
215. Jiang, Z., Xiao, T., Kuznetsov, V. L. & Edwards, P. P. Turning carbon dioxide into fuel. *Philosophical Transactions of the Royal Society A: Mathematical, Physical and Engineering Sciences* **368**, 3343–3364 (2010).
216. Oloman, C. & Li, H. Electrochemical Processing of Carbon Dioxide. *ChemSusChem* **1**, 385–391 (2008).
217. Feaster, J. T. *et al.* Understanding Selectivity for the Electrochemical Reduction of Carbon Dioxide to Formic Acid and Carbon Monoxide on Metal Electrodes. *ACS Catalysis* **7**, 4822–4827 (2017).
218. Philips, M. F., Gruter, G.-J. M., Koper, M. T. M. & Schouten, K. J. P. Optimizing the Electrochemical Reduction of CO2 to Formate: A State-of-the-Art Analysis. *ACS Sustainable Chemistry & Engineering* **8**, 15430–15444 (2020).
219. Hori, Y., Kikuchi, K. & Suzuki, S. Production of CO and CH4 in Electrochemical Reduction of CO2 at Metal Electrodes in Aqueous Hydrogencarbonate Solution. *Chemistry Letters* 1695–1698 (1985).
220. Jitaru, M., Lowy, D. A., Toma, M., Toma, B. C. & Oniciu, L. Electrochemical reduction of carbon dioxide on flat metallic cathodes. *Journal of Applied Electrochemistry 1997 27:8* **27**, 875–889 (1997).
221. Zheng, Y. *et al.* Understanding the Roadmap for Electrochemical Reduction of CO2 to Multi-Carbon Oxygenates and Hydrocarbons on Copper-Based Catalysts. *J Am Chem Soc* **141**, 7646–7659 (2019).
222. Xue, Y., Guo, Y., Cui, H. & Zhou, Z. Catalyst Design for Electrochemical Reduction of CO2 to Multicarbon Products. *Small Methods* **5**, 2100736 (2021).
223. P. Kuhl, K., R. Cave, E., N. Abram, D. & F. Jaramillo, T. New insights into the electrochemical reduction of carbon dioxide on metallic copper surfaces. *Energy & Environmental Science* **5**, 7050–7059 (2012).
224. Rui, L. *et al.* Electrochemical Reduction of Carbon Dioxide to 1-Butanol on Oxide-Derived Copper. *Angewandte Chemie* **132**, 21258–21265 (2020).
225. Chen, H., Dong, F. & Minteer, S. D. The progress and outlook of bioelectrocatalysis for the production of chemicals, fuels and materials. *Nature Catalysis* vol. 3 225–244 (2020).
226. Harbaugh, J. *NASA Awards $750,000 in Competition to Convert CO2 into Sugar*. http://www.nasa.gov/directorates/spacetech/centennial_challenges/75K-awarded-in-competition-to-convert-carbon-dioxide-into-sugar.html (2021).
227. Kim, D., Kley, C. S., Li, Y. & Yang, P. Copper nanoparticle ensembles for selective electroreduction of CO2 to C2–C3 products. *Proc Natl Acad Sci U S A* **114**, 10560–10565 (2017).
228. Li, Y. *et al.* Electrochemically scrambled nanocrystals are catalytically active for CO2-to-multicarbons. *Proceedings of the National Academy of Sciences* **117**, 9194–9201 (2020).
229. Mohan, D., Pittman Jr., C. U. & Steele, P. H. Pyrolysis of Wood/Biomass for Bio-oil: A Critical Review. *Energy and Fuels* **20**, 848–889 (2006).
230. Schandel, C. B., Høj, M., Osmundsen, C. M., Jensen, A. D. & Taarning, E. Thermal Cracking of Sugars for the Production of Glycolaldehyde and Other Small Oxygenates. *ChemSusChem* **13**, 688–692 (2020).
231. Heim, L. E., Konnerth, H. & Prechtl, M. H. G. Future perspectives for formaldehyde: Pathways for reductive synthesis and energy storage. *Green Chemistry* vol. 19 2347–2355 (2017).

232. Appayee, C. & Breslow, R. Deuterium studies reveal a new mechanism for the formose reaction involving hydride shifts. *J Am Chem Soc* **136**, 3720–3723 (2014).
233. Lambert, J. B., Gurusamy-Thangavelu, S. A. & Ma, K. The silicate-mediated formose reaction: Bottom-up synthesis of sugar silicates. *Science (1979)* **327**, 984–986 (2010).
234. Szeja, W., Fokt, I. & Grynkiewicz, G. Benzylation of sugar polyols by means of the PTC method. *Recueil des Travaux Chimiques des Pays-Bas* **108**, 224–226 (1989).
235. Charnay, B. P., Cui, Z., Marx, M. A., Palazzo, J. & Co, A. C. Insights into the CO2 Reduction Pathway through the Electrolysis of Aldehydes on Copper. *ACS Catalysis* **11**, 3867–3876 (2021).
236. Clark, E. L. & Bell, A. T. Direct Observation of the Local Reaction Environment during the Electrochemical Reduction of CO2. *J Am Chem Soc* **140**, 7012–7020 (2018).
237. Löffler, M., Khanipour, P., Kulyk, N., Mayrhofer, K. J. J. & Katsounaros, I. Insights into Liquid Product Formation during Carbon Dioxide Reduction on Copper and Oxide-Derived Copper from Quantitative Real-Time Measurements. *ACS Catalysis* **10**, 6735–6740 (2020).
238. Nakata, K., Ozaki, T., Terashima, C., Fujishima, A. & Einaga, Y. High-Yield Electrochemical Production of Formaldehyde from CO2 and Seawater. *Angewandte Chemie International Edition* **53**, 871–874 (2014).
239. Birdja, Y. Y. & Koper, M. T. M. The Importance of Cannizzaro-Type Reactions during Electrocatalytic Reduction of Carbon Dioxide. *J Am Chem Soc* **139**, 2030–2034 (2017).
240. Breslow, R. On the mechanism of the formose reaction. *Tetrahedron Letters* **1**, 22–26 (1959).
241. Mizuno, T. & Weiss, A. H. Synthesis and utilization of formose sugars. *Advances in Carbohydrate Chemistry and Biochemistry* **29**, 173–227 (1974).
242. Butlerow, A. Bildung einer zuckerartigen Substanz durch Synthese. *Justus Liebigs Ann Chem* **120**, 295–298 (1861).
243. Pallmann, S. *et al.* Schreibersite: An effective catalyst in the formose reaction network. *New Journal of Physics* **20**, 55003 (2018).
244. Eckhardt, A. K., Linden, M. M., Wende, R. C., Bernhardt, B. & Schreiner, P. R. Gas-phase sugar formation using hydroxymethylene as the reactive formaldehyde isomer. *Nature Chemistry* (2018) doi:10.1038/s41557-018-0128-2.
245. Khomenko, T. I. *et al.* Homogeneously catalyzed formaldehyde condensation to carbohydrates: IV. Alkaline earth hydroxide catalysts used with glycolaldehyde co-catalyst. *Journal of Catalysis* **45**, 356–366 (1976).
246. Irie Setsuko. Selective Formose Reaction Initiated By Photo- And γ-Irradiation. *Chemistry Letters* **13**, 2153–2156 (1984).
247. Tambawala, H. & Weiss, A. H. Homogeneously catalyzed formaldehyde condensation to carbohydrates: II. Instabilities and Cannizzaro effects. *Journal of Catalysis* **26**, 388–400 (1972).
248. Ball, G. F. M. The application of HPLC to the determination of low molecular weight sugars and polyhydric alcohols in foods: A review. *Food Chemistry* **35**, 117–152 (1990).
249. Omran, A., Menor-Salvan, C., Springsteen, G. & Pasek, M. The Messy Alkaline Formose Reaction and Its Link to Metabolism. *Life 2020, Vol. 10, Page 125* **10**, 125 (2020).
250. Yoshihiro, S., Takashi, F., Chikahiro, S. & Teruo, M. Formose Reactions. III. Evaluation of Various Factors Affecting the Formose Reaction. *Bull Chem Soc Jpn* **50**, 1527–1531 (1977).

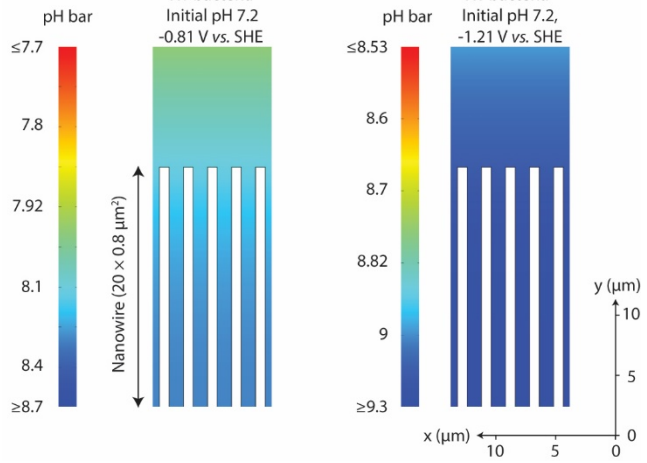
251. Soares, A. P. V., Portela, M. F. & Kiennemann, A. Methanol Selective Oxidation to Formaldehyde over Iron-Molybdate Catalysts. *http://dx.doi.org/10.1081/CR-200049088* **47**, 125–174 (2007).
252. Millar, G. J. & Collins, M. Industrial Production of Formaldehyde Using Polycrystalline Silver Catalyst. *Industrial and Engineering Chemistry Research* **56**, 9247–9265 (2017).
253. Shen, X. & Perreault, H. Characterization of carbohydrates using a combination of derivatization, high-performance liquid chromatography and mass spectrometry. *Journal of Chromatography A* **811**, 47–59 (1998).
254. Lendenmann, U. & Egli, T. Is Escherichia coli growing in glucose-limited chemostat culture able to utilize other sugars without lag? *Microbiology (N Y)* **141**, 71–78 (1995).
255. Pinhal, S., Ropers, D., Geiselmann, J. & de Jong, H. Acetate metabolism and the inhibition of bacterial growth by acetate. *Journal of Bacteriology* **201**, 147–166 (2019).
256. Nakata, K., Ozaki, T., Terashima, C., Fujishima, A. & Einaga, Y. High-Yield Electrochemical Production of Formaldehyde from CO2 and Seawater. *Angewandte Chemie International Edition* **53**, 871–874 (2014).
257. Xu, J., Natsui, K., Naoi, S., Nakata, K. & Einaga, Y. Effect of doping level on the electrochemical reduction of CO2 on boron-doped diamond electrodes. *Diamond and Related Materials* **86**, 167–172 (2018).
258. Birdja, Y. Y. & Koper, M. T. M. The Importance of Cannizzaro-Type Reactions during Electrocatalytic Reduction of Carbon Dioxide. *J Am Chem Soc* **139**, 2030–2034 (2017).

Supplementary Information

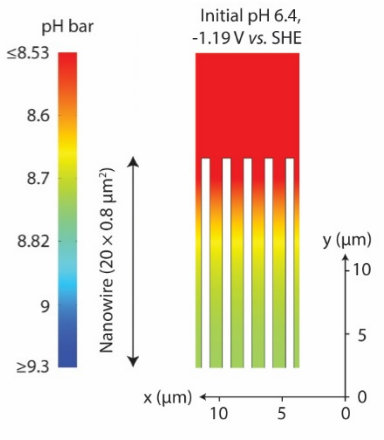
S.I.: Chapter 2



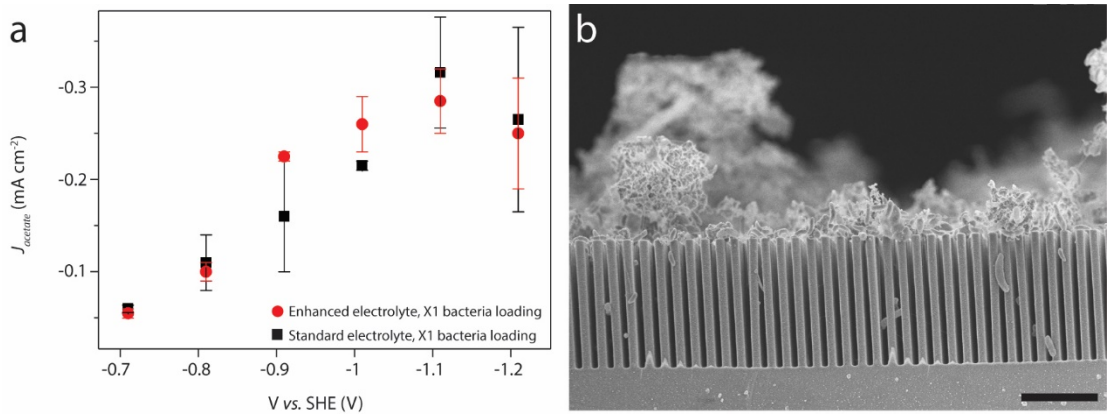
Supplementary Figure 2.1 | Characterization of the precipitate on the nanowire surface. (a) SEM image shows the precipitate formed on the nanowire surface at η of −1.2 V vs. SHE when standard media was used as the electrolyte. *S. ovata* also escaped from the nanowire arrays. (b) The EDS data indicated that the precipitate consisted mainly of calcium and magnesium phosphate and carbonate while $CaCO_3$, $MgCO_3$ and $Mg(OH)_2$ species may also exist due to the increased pH as described in Fig. S2.2



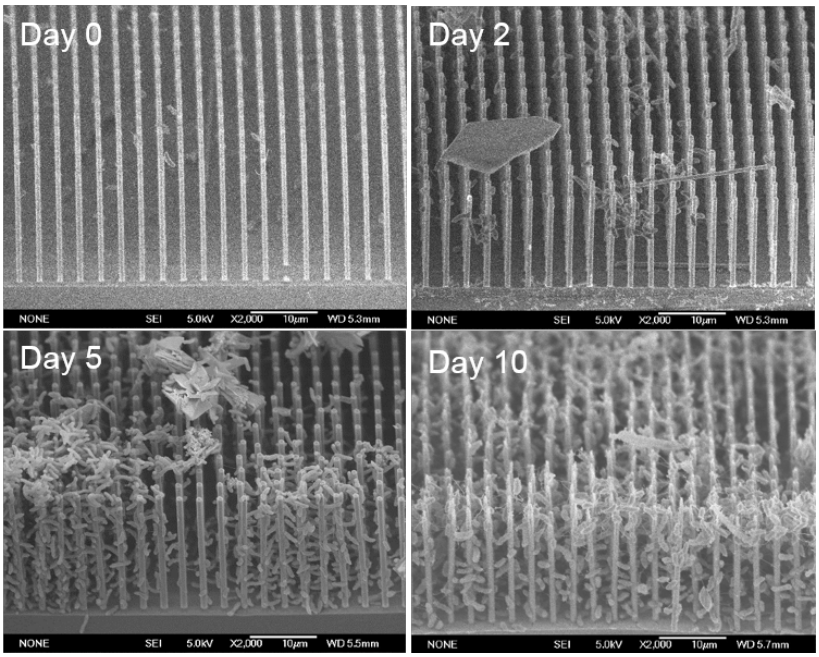
Supplementary Figure 2.2 | COMSOL simulations confirm the pH profile around nanowires at low (−0.81 V *vs.* SHE) and high overpotential (−1.21 V *vs.* SHE) when the standard media was used as the electrolyte. The boundary pH values were the bulk pH measured in the cathode chamber. The alkaline environment is not suitable for *S. ovata*.



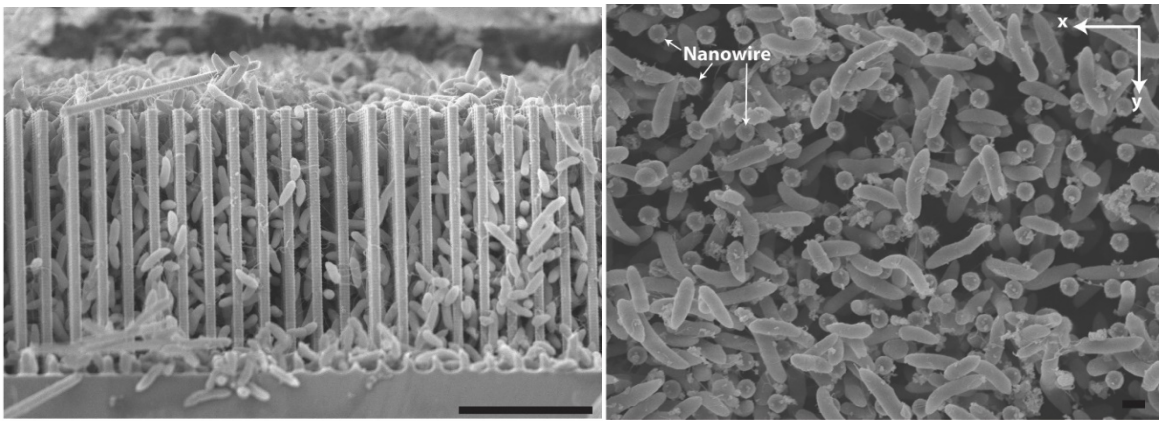
Supplementary Figure 2.3 | The COMSOL simulation confirms the pH profile around nanowires at overpotential of −1.21 V *vs.* SHE when the phosphate enhanced media was used as the electrolyte.



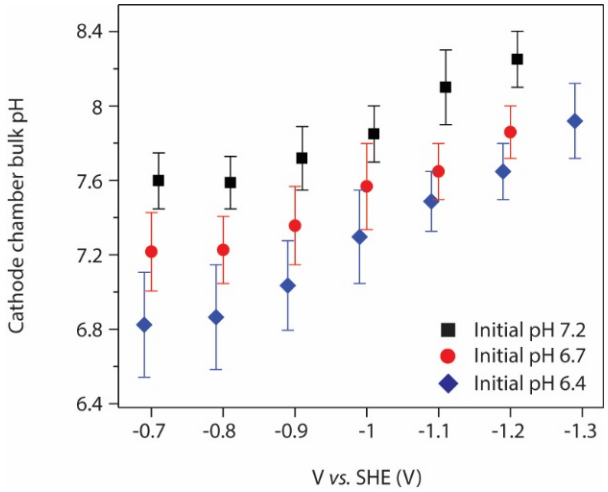
Supplementary Figure 2.4 | Even using phosphate enhanced media as electrolyte, simply increasing the bias to −1.2V *vs.* SHE did not enhance the acetate production rate. Bacteria still escaped from the electrodes. (a) The acetate current $J_{acetate}$ showed no significant current improvement at high bias of −1.21 V vs. SHE after standard media was replaced by phosphate enhanced media as the electrolytes, when 4% v/v bacteria was inoculated (n=3). (b) An SEM image of the hybrids after operation at η of −1.21 V vs. SHE showed that although no precipitate was observed, most of the bacteria remained on the top of the nanowires.



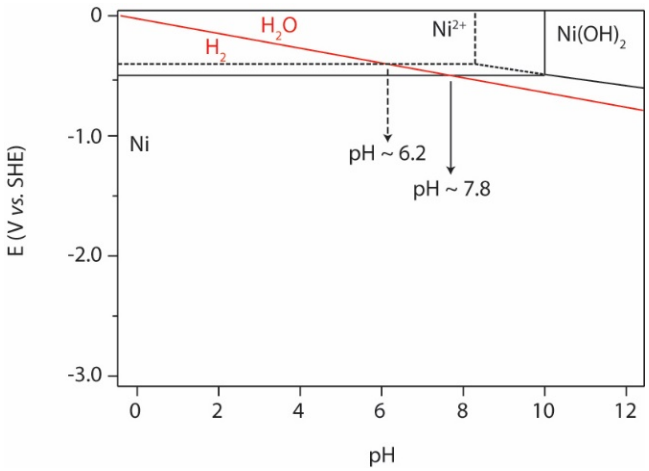
Supplementary Figure 2.5 | SEM images showed the development of *S. ovata* within the nanowire array. After inoculating 4% v/v bacteria suspension, using phosphate enhanced media as the electrolyte, and moderate current and overpotential (0.1~0.2 mA/cm^2 and −0.8~−0.9 V vs. SHE), *S. ovata* gradually grew around nanowires and formed densely-packed hybrid system.



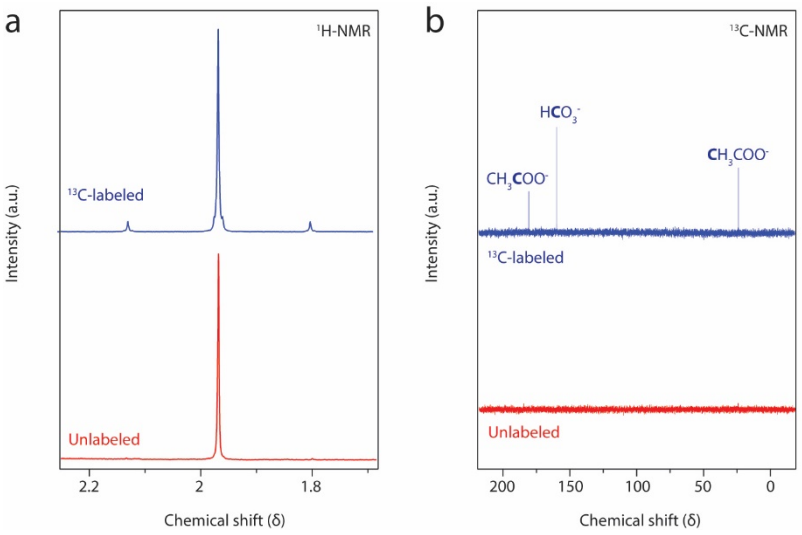
Supplementary Figure 2.6 | Representative cross-section (a) and top-down view (b) images of a close-packed bacteria/nanowire hybrid after the system was inoculated with 20% v/v bacteria suspension using phosphate enhanced media as the electrolyte, and operated at 0.1~0.2 mA/cm^2 and −0.8 V vs. SHE for 3 days. The cell density of the close-packed hybrid can be estimated by multiplying the bacteria density along the z-axis (~10, from panel a) by the bacteria density in the x-y plane (~1.3 per nanowire, from panel b). The resulting bacteria loading density is about 13 per nanowire. The scale bars are 10 μm and 1 μm respectively.



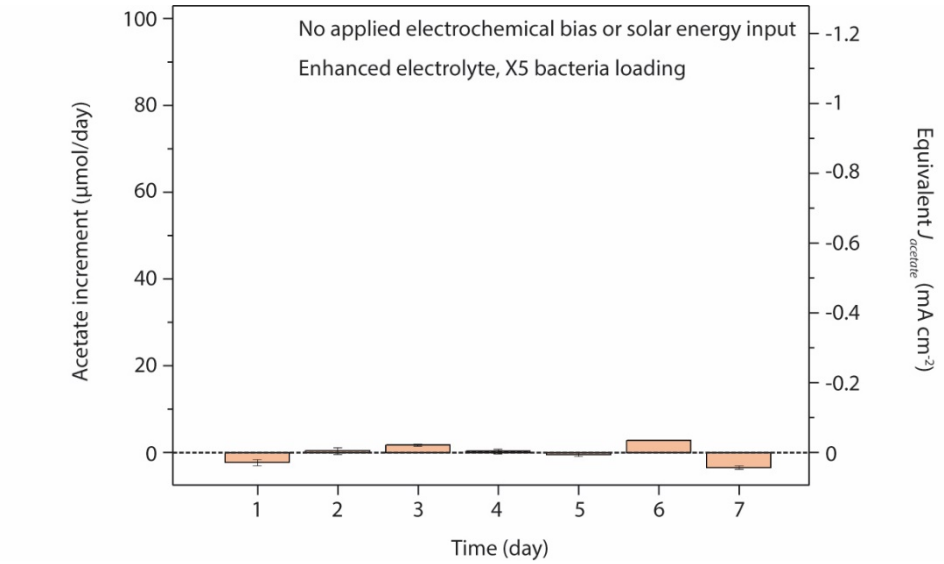
Supplementary Figure 2.7 | The bulk pH in the cathode chamber as a function of the applied electrochemical potential. Phosphate enhanced media with different initial pH was used as the electrolyte.



Supplementary Figure 2.8 |. Pourbaix diagram of the Ni-water system. The pourbaix diagram is calculated based on the initial Ni^{2+} concentration (10^{-7} mol/L, based on the DSMZ media) and the dissolved Ni^{2+} concentration if all the sputtered Ni on the nanowires is assumed to be dissolved (~10^{-4} mol/L). When the pH is larger than 7.8, all the sputtered Ni on the nanowires in aqueous solution should be well preserved. If pH is smaller than 6.2, the sputtered Ni may dissolve which hinders electron transfer.



Supplementary Figure 2.9 | Nuclear magnetic resonance (NMR) characterization of the produced acetate. (a) 1H-NMR spectra of acetate produced with ^{13}C labeled electrolyte and unlabeled electrolyte. For ^{13}C labeled samples, the satellite peaks result from $^{1}J_{CH}$ and $^{2}J_{CH}$ coupling. (b) The ^{13}C signal was observed in bicarbonate and acetate when $NaH^{13}CO_3$ was added to the electrolyte. Since the purged CO_2 gas was not ^{13}C labeled, not all of the produced acetate appears as ^{13}C labeled.



Supplementary Figure 2.10 | Acetate production under dark or open-circuit condition. The acetate production and the equivalent $J_{acetate}$ were negligible when no electrochemical bias or solar energy input was applied.



Supplementary Figure 2.11 | SEM image of the bacteria/nanowire hybrids of the solar-driven experiment after one-week operation. Scale bar: 10 μm.

S.I.: Chapter 3

Supplementary Table 3.1: DM9 recipe

Component	Concentration (per 1L)
NH_4Cl	1 g
Na_2HPO_4	7 g
NaH_2PO_4- $2H_2O$	3.9 g
$CaCl_2$- $2H_2O$	1.47mL of 10 g/L
$MgSO_4$- $7H_2O$	10mL of 0.1M

Addition of 2g/L sodium acetate is optional

Supplementary Table 3.2: S. ovata growth and acetate production parameters

Parameter	Value	Unit	Source
Operating conditions			
T	308.15	K	Experiment
P_{tot}	30	psi	Experiment
$\mathrm{OD}_{545}(t = 0\ \mathrm{hr})$	0.01	--	Experiment
$c_{\mathrm{Ac}}\ (t = 0\ \mathrm{hr})$	1.64	mM	Experiment
Reactor geometry			
$V_{\mathrm{L}}/V_{\mathrm{G}}$	0.43	--	Experiment
Biomass growth			
μ_{max}	0.044	hr^{-1}	[1]
$K_{\mathrm{S,H_2}}$	20	μM	[2]
$K_{\mathrm{S,CO_2}}$	20	μM	[2]
Biomass yield			
$Y'_{\mathrm{X/H_2}}$	0.49	mol mol^{-1}	Element balance
$Y'_{\mathrm{Ac/H_2}}$	0.25	mol mol^{-1}	Element balance
$Y'_{\mathrm{X/CO_2}}$	1	mol mol^{-1}	Element balance
$Y'_{\mathrm{Ac/CO_2}}$	0.5	mol mol^{-1}	Element balance
α	31.5	mol mol^{-1}	Fitted
Gas solubility			
$H_{\mathrm{H_2}}$	0.78	mM bar^{-1}	[3]
$H_{\mathrm{CO_2}}$	33	mM bar^{-1}	[3]
Gas/liquid mass transfer			
$k_{\mathrm{L}}a$	0.405	hr^{-1}	Fitted
Other conversions			
Cell molar mass	25	gCDW mol^{-1}	--
Cell density per OD unit	0.33	g L^{-1} OD^{-1}	--

Supplementary Table 3.3: C. basilensis growth and PHB production parameters

Parameter	Value	Unit	Source
Operating conditions			

T	303.15	K	Experiment
$OD_{600}(t = 0\ \text{hr})$	0.001	--	Experiment
$c_{\text{Ac}}(t = 0\ \text{hr})$	26	mM	Experiment
$c_{\text{N}}\ (t = 0\ \text{hr})$	10.1	mM	Supplementary Note 1
Biomass growth			
$\mu_{\text{max,X}}$	0.37	hr^{-1}	Fitted (Supplementary Note 2)
$K_{\text{S,Ac}}$	5	μM	Supplementary Note 3
$K_{\text{I,Ac}}$	500	mM	Supplementary Note 3
$K_{\text{S,N}}$	2.05	mM	Fitted
$K_{\text{I,N}}$	120.8	mM	[4]
$Y'_{\text{X/Ac}}$	0.936	mol mol^{-1}	Supplementary Note 4
$Y'_{\text{X/N}}$	5.096	mol mol^{-1}	[4]
PHB Accumulation			
$\mu_{\text{max,PHB}}$	0.095	hr^{-1}	Fitted
$Y'_{\text{PHB/Ac}}$	0.157	mol mol^{-1}	Supplementary Note 4
$f_{\text{PHB,max}}$	6.13	mol mol^{-1}	[4]
β	3.85	--	[4]

Supplementary notes 3.1

Note 1: Estimating an initial nitrogen concentration

To estimate the initial nitrogen concentration in the diluted, spent *S. ovata* medium, we used the starting concentration of 1 g/L NH_4Cl (~18.5 mM N), accounted for nitrogen consumption by *S. ovata* using the estimate that 0.24 moles of nitrogen are consumed per mole of biomass (using the biomass formula $CH_{1.77}N_{0.24}O_{0.49}$), and divided the result by 1.8 to account for the dilution of spent *S. ovata* medium prior to inoculation with *C. basiliensis*.

Note 2: Estimating $\mu_{\text{max,X}}$

Because no PHB accumulation occurs during the first 16 hrs of *C. basiliensis* growth and neither acetate nor nitrogen concentrations limit growth during this period, we used these initial time points to fit a maximum growth rate for *C. basiliensis* cells, resulting in an estimate of 0.37 hr^{-1}.

Note 3: Half-saturation and inhibition constants for C. basiliensis *growth on acetate*

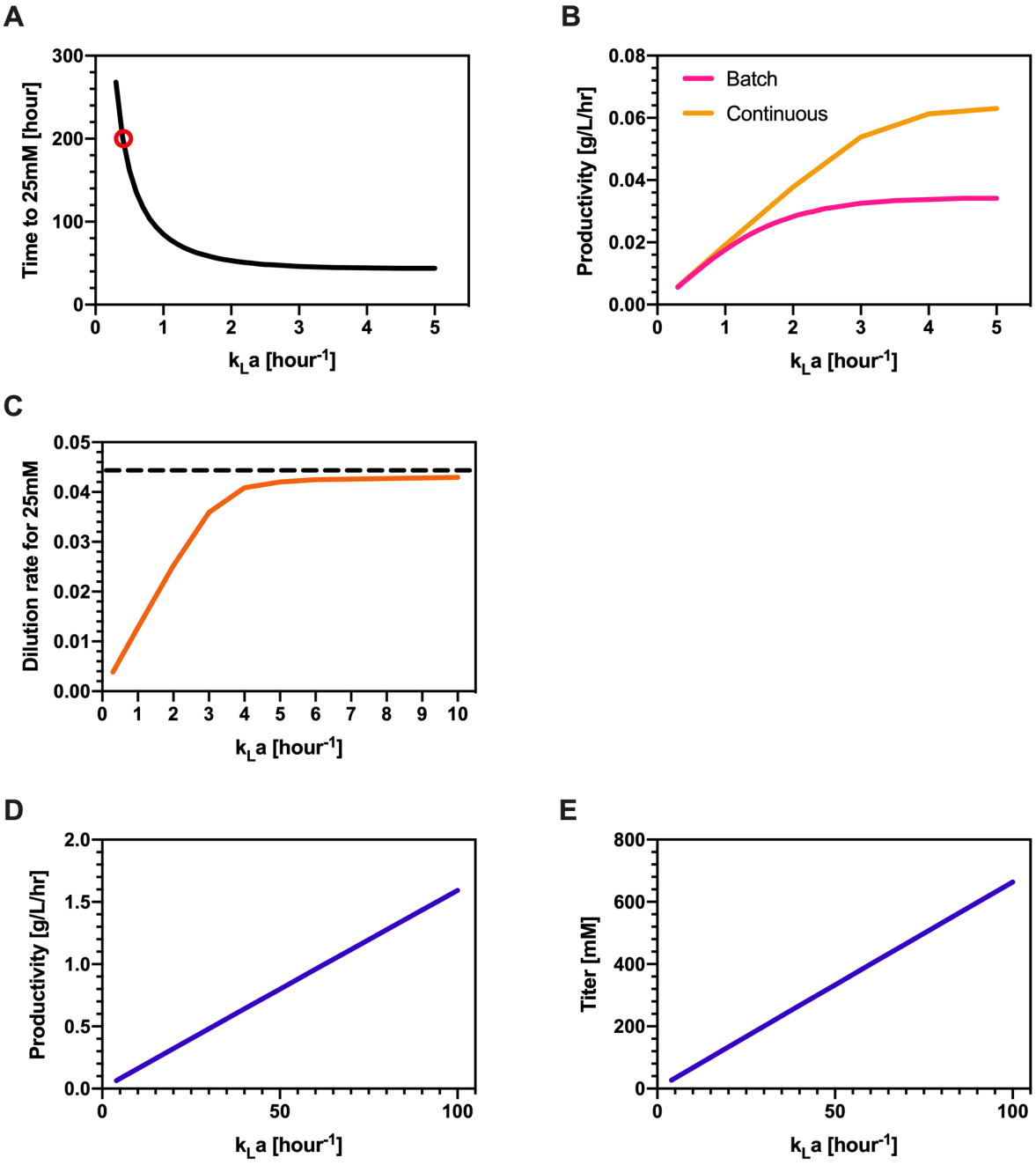
We could not find literature estimates of the half-saturation and inhibition constants for *C. basiliensis* growth on acetate, although values as low as 1 μM have been reported for diverse microorganisms.[5,6] We used 5 μM as an estimate, although the actual value doesn't impact model results unless it is >1 mM (data not shown). A similar paucity of data exists for inhibition constants for *C. basiliensis*. However, 750 – 800 mM ranges are common for both *E. coli*[7] and in volatile fatty acid-degrading consortia[8], so we used 500 mM as a conservative estimate for this value. The model fit is only marginally affected provided $K_{\text{I,Ac}}$ > ~150 mM.

Note 4: On biomass and PHB yields on acetate

We similarly could not find literature estimates for biomass and PHB yields on acetate for *C. basiliensis*. However, a wealth of growth data exists with glucose as the substrate for the closely related species *C. necator*[9], which reports $Y_{\text{X/S}}$ and $Y_{\text{P/S}}$ values of 0.52 g cells g^{-1} glucose and 0.3 g PHB g^{-1} glucose, respectively. Noting that 1 glucose yields 2 pyruvates, and 2 acetates yield 1 pyruvate, we approximate the

value of 1 glucose molecule as equal to the value of 4 acetate molecules. This results in a biomass yield of 0.39 g cells g^{-1} acetate, or equivalently 23.4 g cells mol^{-1} acetate, equivalent to the experimental yield of *E. coli* biomass on acetate[10], lending validity to our approach. Following the same strategy results in an estimated PHB yield of 0.225 g PHB g^{-1} acetate.

Supplementary figure 3.1 and discussion on improvements toward bioprocess scalability



Supplementary Figure 3.1 | Starting with the presented cell culture conditions, we generated a plot **A)** to calculate the time required to reach 25 mM acetate given a particular k_La in a fed batch

system. The red circle corresponds to the fitted k_La value from the experimental demonstration. We could decrease the time required to reach 25mM by 150 hours (or ~75%) by increasing the k_La to 10 hr^{-1}. However, the specific growth rate of *S. ovata* ultimately places an upper limit on the acetate production rate, beyond which further increases in k_La will be of no utility. Continuous operation enables higher acetate productivity because bacteria can be maintained at relatively high concentrations in the exponential growth phase. Setting the liquid dilution rate to maintain a constant acetate concentration of 25 mM results in a productivity 2-fold higher than the batch case (**B**) at k_La values >~3 hr^{-1}. To maintain 25 mM as k_La increases, the dilution rate must also increase, approaching the maximum specific growth rate of 0.044 hr^{-1} (**C**). However, because the dilution rate cannot exceed the specific growth rate without causing cell washout, productivity in this system is limited to ~0.066 g/L/h. Significantly higher productivities are achievable if the acetate titer is allowed to exceed 25 mM. To illustrate this point, we plot the acetate productivity (**D**) and titer (**E**) as a function of k_La for a fixed dilution rate of 0.04 hr^{-1}. We note that the high acetate concentrations observed at productivities >1 g/L/h could be toxic to *S. ovata* and that, in these cases, active control would be necessary to maintain near-neutral pH in the reactor.

Supplementary Table 3.4: Weights of process components for different versions of the CO_2 to acetate to PHB bioreaction. Targeting production 1kg PHB assuming production of 1g PHB L^{-1} day^{-1}, translating to 1000L bioreactors in series.

Parameter	**Abiotic PHB production**	**Biological production without media recycle**	**Biological production with media recycle (this method)**	**Biological production with media recycle and automated pH adjustment**
Media Components (S. ovata and DM9 media as applicable)	0 kg	14.9 kg	12.0 kg	1 kg
Acetate purification	0 kg	Ethyl acetate (1:1 ratio, 900kg) Distillation column (weight varies)	0 kg	0 kg
Pre-made PHB	1.00 kg	0 kg	0 kg	0 kg
Approximate Total System Mass	**1 kg**	**>> 14.9 kg**	**12 kg**	**1 kg**

Potential for further recycle?	No	Yes	Yes	Yes

S.I.: Chapter 4

Supplementary Text 4.1:

Cell culture medium preparation recipes and notes:
Unless otherwise noted all the media is prepared in degassed H_2O. H_2O is degassed by purging N_2/Ar until boiling. 25% more ultrapure water is used to account for evaporation losses. In order to prevent precipitation of medium components during autoclaving, certain components are added after autoclaving (or boiling). These were separately autoclaved, or syringe filtered. The hungate technique was employed to maintain anoxic media and solutions.

	STOCK	BETAINE MEDIUM	YEAST MEDIUM	AUTOTROPHIC MEDIUM
BEFORE BOILING	NaCl, $MgSO_4$, NH_4Cl and $CaCl_2$ (5X) [1]	20 mL	20 mL	20 mL
	K_2HPO_4 and KH_2PO_4 (5X) [2]	20 mL	20 mL	20 mL
	$FeSO_4$ (500X) [3]	0.2 mL	0.2 mL	0.2 mL
	$NaHSeO_3$ (1000X) [4]	0.1 mL	0.1 mL	0.1 mL
	Trace Metal [5]	0.1 mL	0.1 mL	0.1 mL
	Tungstate (1X) [6]	0.1 mL	0.1 mL	0.1 mL
	Ultrapure water	55 mL	55 mL	55 mL
BEFORE AUTOCLAVE	Yeast	0.2 g	0.2 g	
	Casitone	0.2 g		
AFTER AUTOCLAVE	$NaHCO_3$ (8g/100mL)	5 mL	5 mL	5 mL
	Vitamin [7]	1 mL	1 mL	1 mL
	Reducing Reagent [8]	2 mL	2 mL	2 mL
	Betaine stock [9]	5 mL		
	Total:	**100 mL**	**100 mL**	**100 mL**

***S. ovata* Medium Supplementary Table 4.1**

	STOCK	CO-CULTURE MEDIUM
BEFORE AUTOCLAVE	NaCl, $MgSO_4$, and $CaCl_2$ (5X) [10]	20 mL
	$FeSO_4$ (500X) [3]	0.2 mL
	$NaHSeO_3$ (1000X) [4]	0.1 mL
	Trace Metal [5]	0.1 mL

	Tungstate (1X) [6]	0.1 mL
	Ultrapure water	54 mL
AFTER AUTOCLAVE	$NaHCO_3$ (8g/100mL)	5 mL
	Vitamin [7]	1 mL
	K_2HPO_4 and KH_2PO_4 [2]	20 mL
	Total:	**100 mL**

Co-culture Medium Supplementary Table 4.2

	STOCK	**CO-CULTURE MEDIUM**
BEFORE AUTOCLAVE	NaCl, $MgSO_4$, and $CaCl_2$ (5X) [11]	5 mL
	NaCl (5X) [12]	15 mL
	$FeSO_4$ (500X) [3]	0.2 mL
	$NaHSeO_3$ (1000X) [4]	0.1 mL
	Trace Metal [5]	0.1 mL
	Tungstate (1X) [6]	0.1 mL
	Ultrapure water	54 mL
AFTER AUTOCLAVE	$NaHCO_3$ (8g/100mL)	5 mL
	Vitamin [7]	1 mL
	K_2HPO_4, Na_2HPO_4 KH_2PO_4 and NaH_2PO_4 [13]	20 mL
	Total:	**100 mL**

Co-culture Electrolyte Table 4.3

	STOCK	**PM MEDIUM**	**DIAZO/PHOTO-HETEROTROPHIC MEDIUM**	**DIAZO/PHOTO-AUTOTROPHIC MEDIUM**
BEFORE AUTOCLAVE	0.5 M Na_2HPO_4	2.5 mL	2.5 mL	2.5 mL
	0.5 M KH_2PO_4	2.5 mL	2.5 mL	2.5 mL
	10% $(NH_4)_2SO_4$	1 mL		
	Concentrated Base [14]	0.1 mL	0.1 mL	0.1 mL
	0.1 M $Na_2S_2O_3$	0.1 mL	0.1 mL	
	PABA (2 mg/mL)	0.1 mL	0.1 mL	0.1 mL
	0.5 M $NaHCO_3$			5 mL
	Ultrapure water	92 mL	95 mL	88 mL
AFTER AUTOCLAVE	1M Sodium Acetate	2 mL (20mM)	Variable	
	NiCl			1 μM
	Total:	**100 mL**	**100 mL**	**100mL**

***R. palustris* Medium Supplementary Table 4.4**

[1] NaCl 11.25 g/L, $MgSO_4 \cdot 7H_2O$ 2.5 g/L, NH_4Cl 2.5 g/L and $CaCl_2$ 1.25 g/L

[2] K_2HPO_4 1.74 g/L and KH_2PO_4 1.135 g/L

[3] $FeSO_4$ $7H_2O$ 1 g/L

[4] $NaHSeO_3$ $5H_2O$ 10^{-4} mol/L

[5] Trace Metal

Component	**Amount**
HCl (25%)	10 mL
$FeCl_2$ $4H_2O$	1.5 g
$ZnCl_2$	0.07 g
$MnCl_2$ $4H_2O$	0.1 g
H_3BO_3	0.006 g
$CoCl_2$ $2H_2O$	0.19 g
$NiCl_2$ $6H_2O$	0.002 g
Na_2MoO_4 $2H_2O$	0.036 g
Ultrapure water	990 mL
Total	**1000 mL**

[6] $NaWO_4$ $2H_2O$ 4 g/L

[7] Vitamin

Component	**Amount**
Biotin	2 g
Folic acid	2 g
Pyridozine-HCl	10 g
Thiamine-HCl	5 g
Riboflavin	5 g
Nicotinic acid	5 g
Ca-D-pantothenate	5 g
Vitamin B_{12}	0.1 g
p-Aminobenzoic acid	5 g
a-Lipoic acid	5 g
Ultrapure water	1000 mL
Total	**1000 mL**

[8] Reducing Reagent

Component	**Amount**
L-Cysteine-HCl H_2O	1.5 g
Na_2S $9H_2O$	1.5 g
Ultrapure water	100 mL
Total	**100 mL**

[9] Betaine H_2O 1.34 g/L

[10] NaCl 11.25 g/L, $MgSO_4 \cdot 7H_2O$ 2.5 g/L, and $CaCl_2$ 1.25 g/L

[11] NaCl 4.518 g/L, $MgSO_4 \cdot 7H_2O$ 2.5 g/L, and $CaCl_2$ 1.25 g/L

[12]NaCl 4.518 g/L

[13] K_2HPO_4 1.74 g/L KH_2PO_4 1.135 g/L, $Na_2HPO_4{*}7H_2O$ 10.725 g/L, $NaH_2PO_4{*}H_2O$ 4.69 g/L

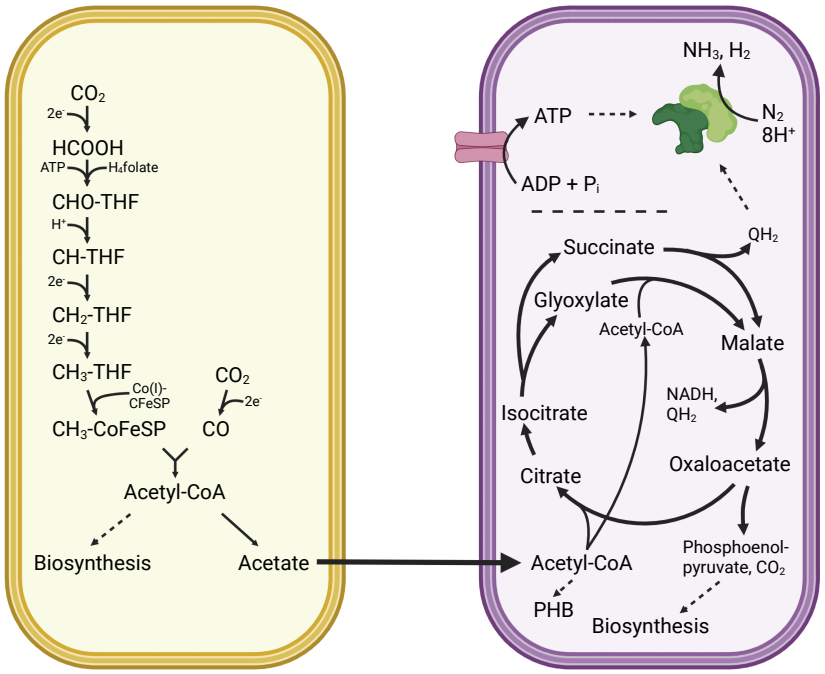
[14] Concentrated Base

Component	**Amount**
Nitrilotriacetic acid (free acid)	20 g
$MgSO_4$ anhydrous	28.9 g
$CaCl_2$ $2H_2O$	6.67 g
$(NH_4)_6Mo_7O_{24}$ $4H_2O$	0.0185 g
$FeSO_4$ $7H_2O$	0.198 g
Ultrapure water	900 mL
Metal 44 [15]	100 mL
Total:	**1000 mL**

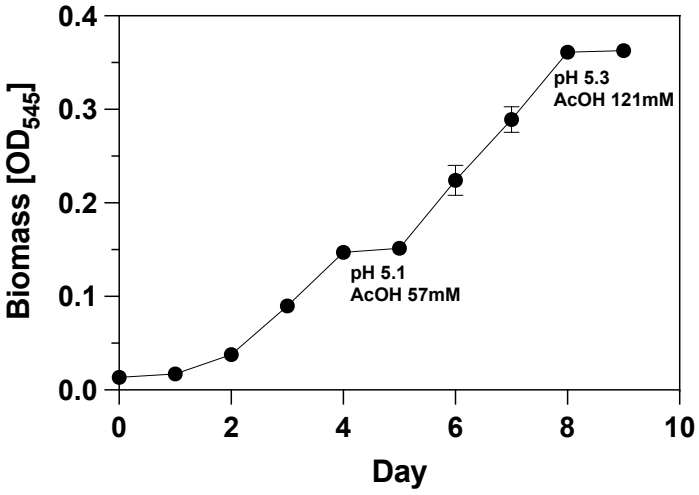
[15] Metal 44

Component	**Amount**
EDTA (free acid)	2.5 g
$ZnSO_4$ $7H_2O$	10.95 g
$FeSO_4$ $7H_2O$	5 g
$MnSO_4$ H_2O	1.54 g
$CuSO_4$ $5H_2O$	0.392 g
$Co(NO_3)_2$ $6H_2O$	0.25 g
$Na_2B_4O_7$ 10 H_2O	0.177 g
Ultrapure water	1000 ml
Total:	**1000 mL**

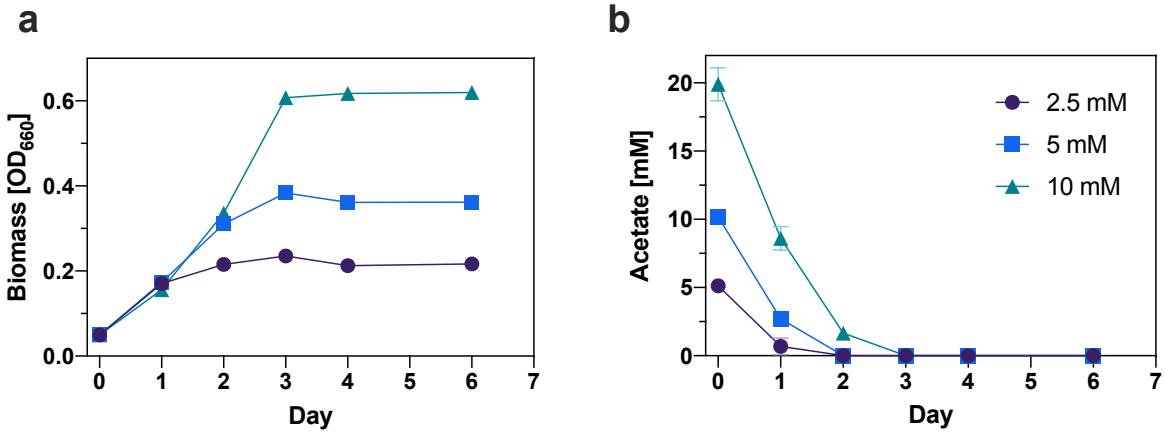
Supplementary Figures



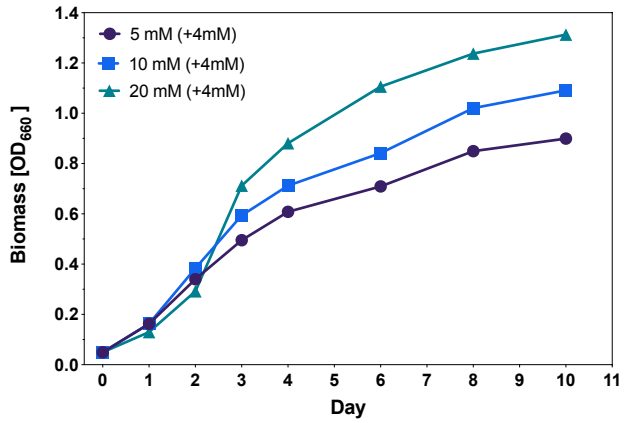
Supplementary Figure 4.1 | Overview of internal metabolic pathways in *S. ovata* and *R. palustris nif*A*. *S. ovata* converts CO_2 to acetate via the Wood-Ljungdahl pathway in which 1 CO_2 is converted to formate to be adhered onto tetrahydrofolate and finally combined with an iron coronoid protein as a methyl group. The methyl group is joined with CO to form Acetyl-CoA which is either converted to acetate (releasing ATP) is used in protein biosynthesis. *R. palustris nif*A* initially transforms acetate to Acetyl-CoA which is then used in the tricarboxylic acid cycle with a glyoxylate shunt to generate reducing equivalents (to be used in cellular processes like N_2 hydrogenation) and produce metabolic intermediates for protein biosynthesis.



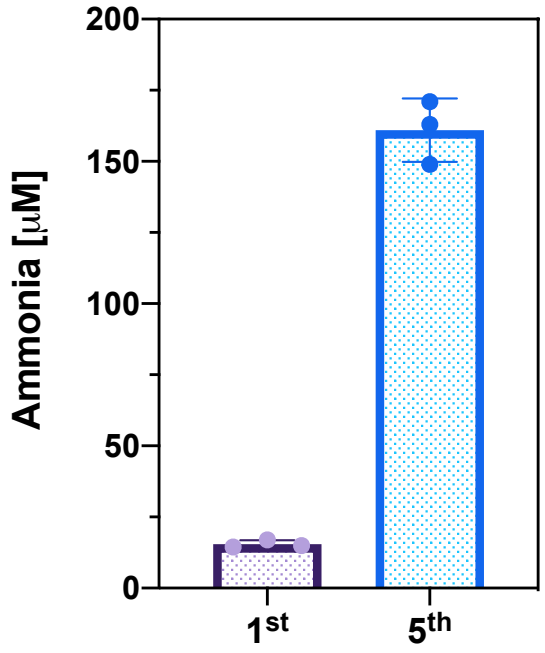
Supplementary Figure 4.2 | Autotrophic *S. ovata* culture shows dependency of culture growth with medium pH. Autotrophic medium has a pH of 6.8 pre-inoculation, which decreases to ~5.2 with an acetate (AcOH) concentration of ~60mM. Culture growth plateaus once medium is acidified, but growth can be recovered by stabilizing medium pH to 6.8. Culture plateaus once again with medium acidification. Error bars represent one standard deviation of three independent measurements.



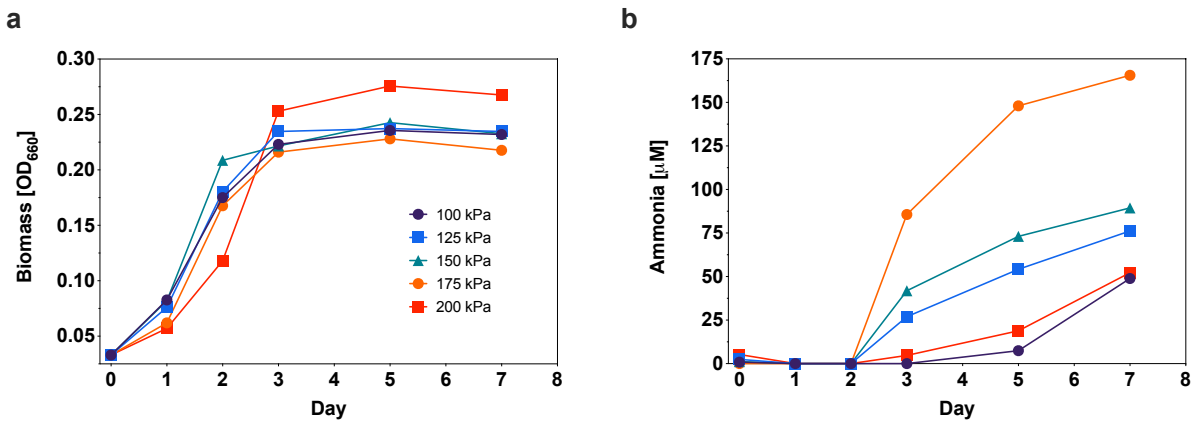
Supplementary Figure 4.3 | *R. palustris nif*A* cultures supplemented with 2.5mM, 5mM and 10mM acetate. a) Final biomass yield is proportional to the acetate provided. b) Tracking the acetate concentration reveals that the acetate is largely consumed by the mid-exponential phase. Error bars represent one standard deviation of three independent measurements.



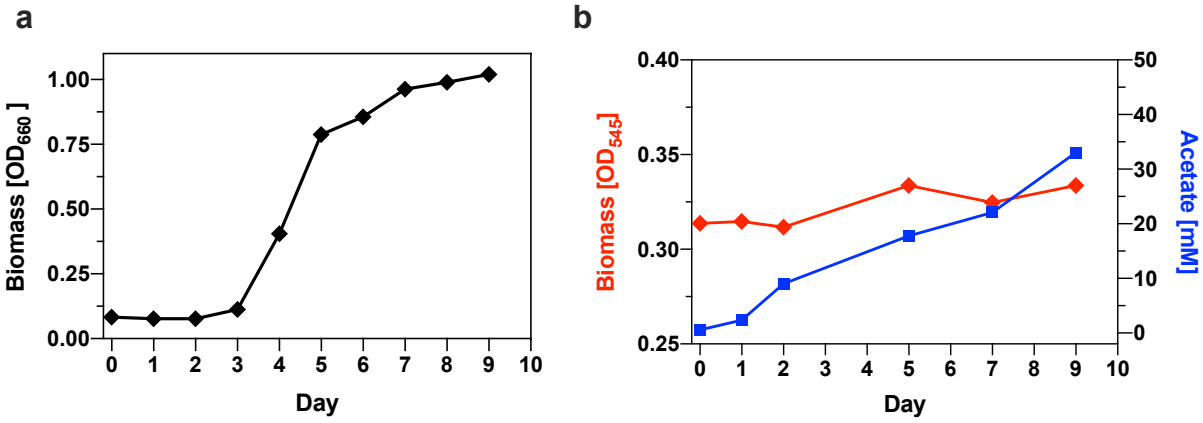
Supplementary Figure 4.4 | *R. palustris nif*A* cultures are supplemented with 5mM, 10mM and 20mM acetate initially and an additionally 4mM acetate is provided on days 2, 4 and 6. This indicates that further *R. palustris nif*A* culture growth may be induced by additional acetate provision.



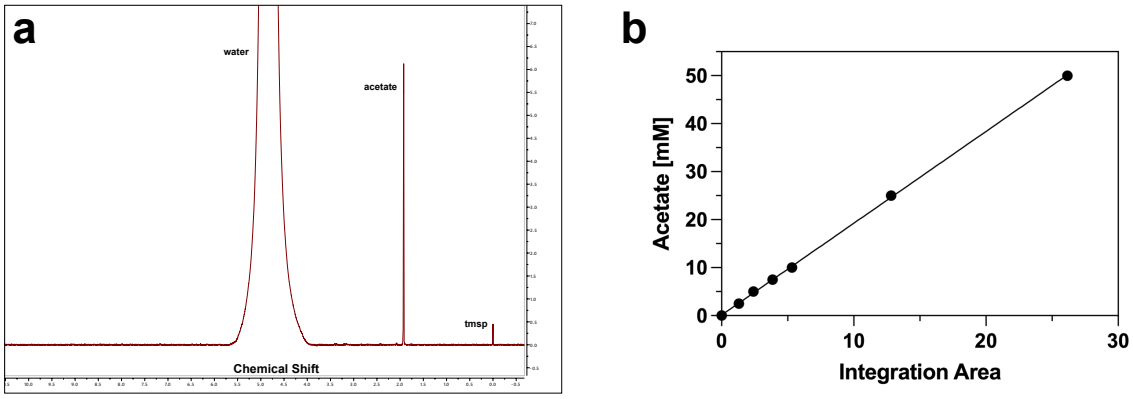
Supplementary Figure 4.5 | *R. palustris nif*A* cultures grown diazotrophically in 1st cycle from frozen stock and 5th cycle from frozen stock. Ammonia secretion in *R. palustris nif*A* may be increased by recursively selecting for cultures with the highest ammonia content. Additionally, cultures soon after the frozen stock stage may not be as metabolically active. Error bars represent one standard deviation of three independent measurements.



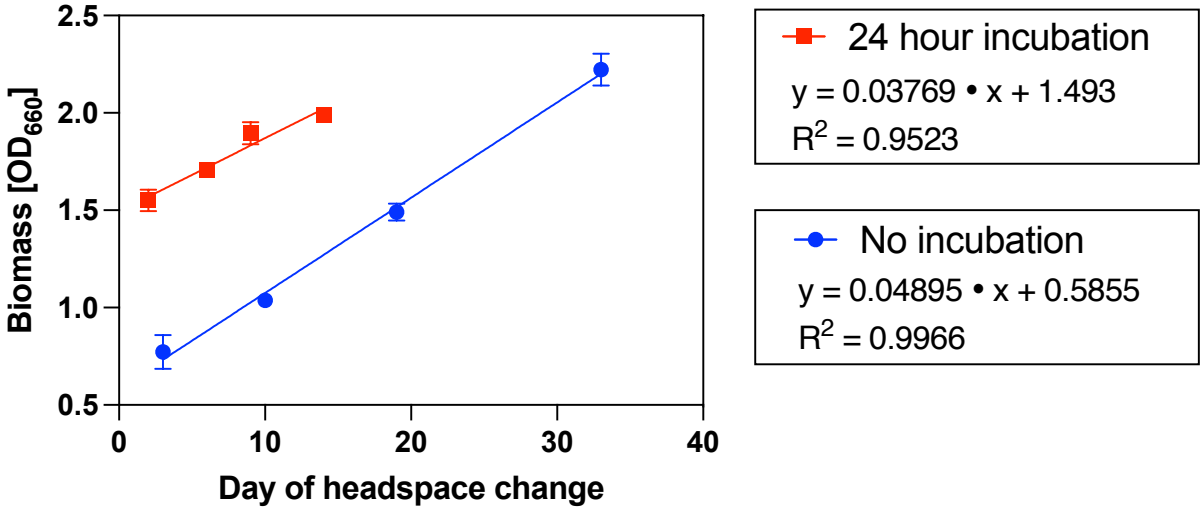
Supplementary Figure 4.6 | a) Diazotrophic, photoheterotrophic *R. palustris nif*A* cultures grown under increasing headspace pressures. Cultures were supplemented with 2.5mM acetate and kept under pure N_2 headspace. b) Extracellular ammonia increases with increasing headspace pressure up to 175kPa.



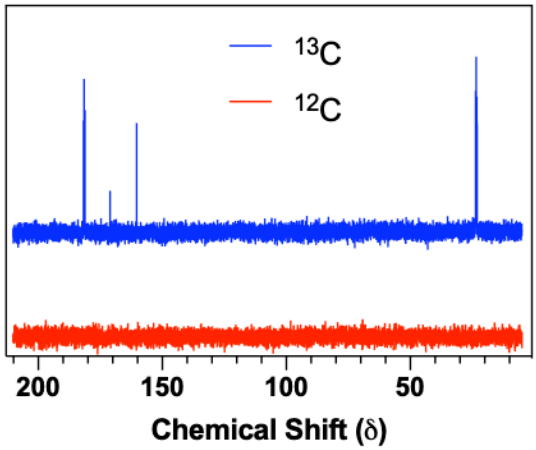
Supplementary Figure 4.7 | *R. palustris nif*A* and *S. ovata* grown individually to verify compatibility of co-culture medium. a) *R. palustris nif*A* culture supplemented with 25mM acetate and b) *S. ovata* culture supplemented with 100uM ammonia.



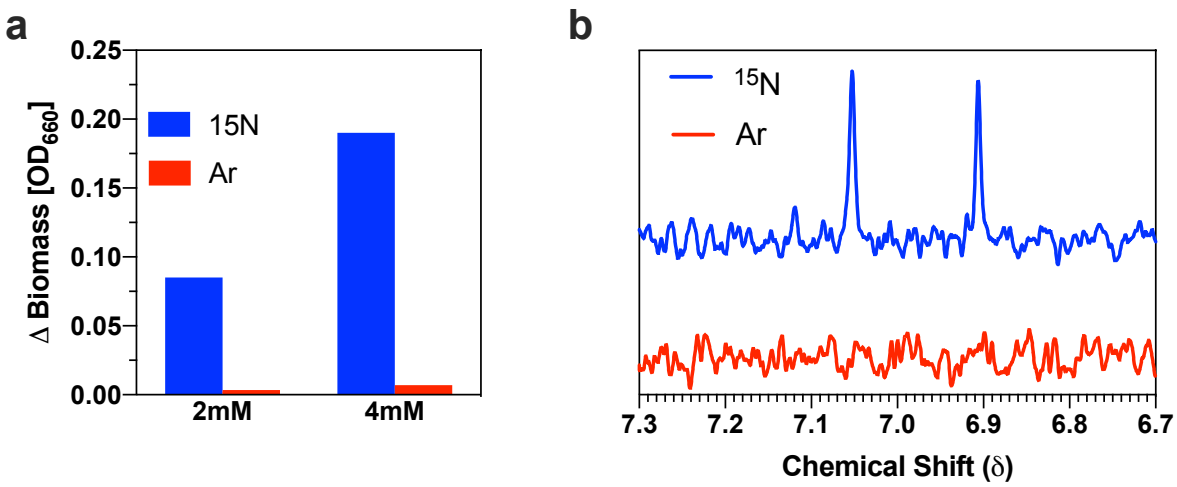
Supplementary Figure 4.8 | a) Representative ^{1}H-NMR spectrum of the medium from an autotrophic *S. ovata* culture. Protons from the methyl group of acetate are detected at 1.92 ppm. sodium 3- (trimethylsilyl)-2,2',3,3'-tetradeuteropropionate (tmsp) is used as an internal standard. b) Calibration curve for acetate quantification with ^{1}H-NMR (R^2=0.999).



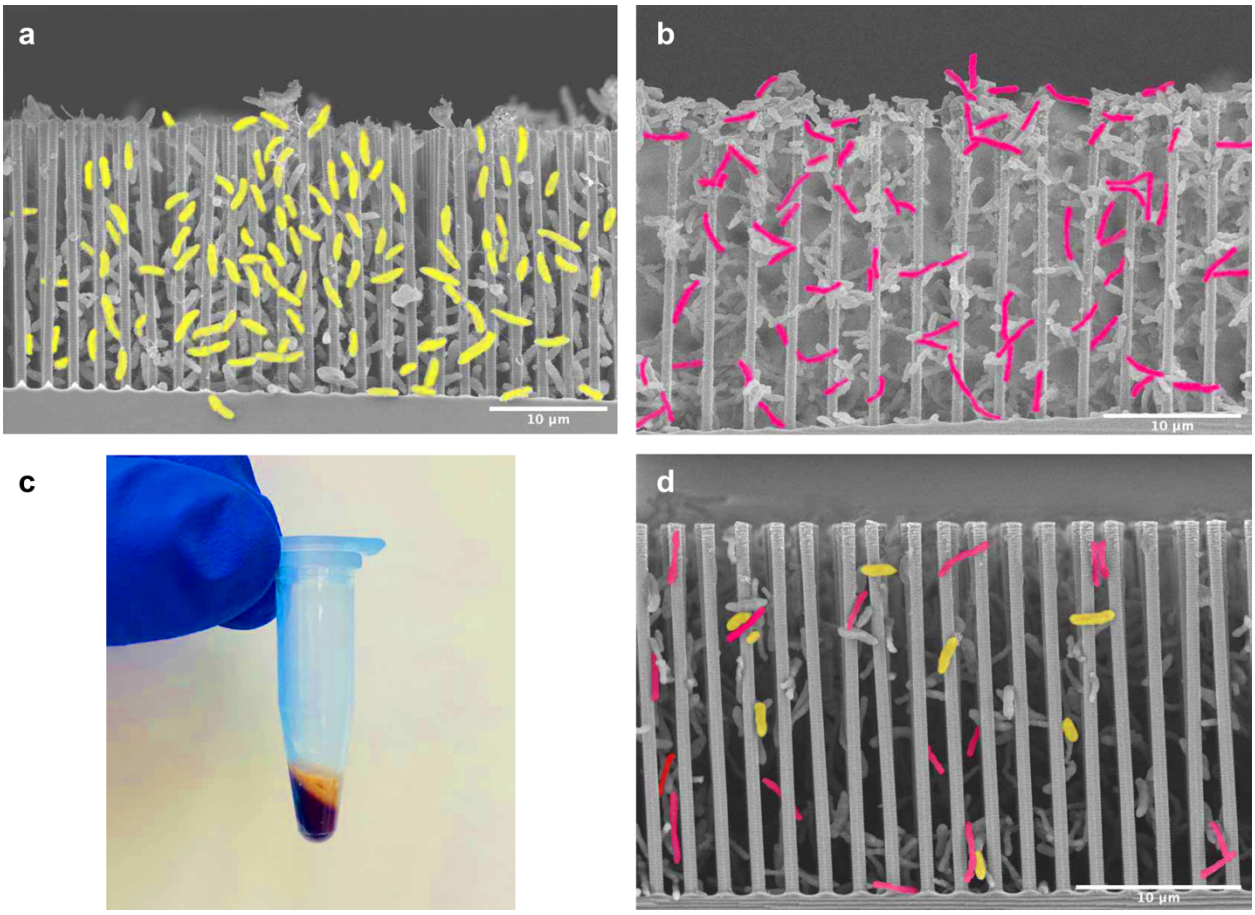
Supplementary Figure 4.9 | *R. palustris nif*A* and *S. ovata* co-culture growth dynamic. Blue plot corresponds to co-cultures where *R. palustris nif*A* and *S. ovata* were inoculated simultaneously while the red plot corresponds to the co-cultures where *S. ovata* was incubated individually for 24 hours prior to the addition of *R. palustris nif*A*. Plot points denote the biomass yield on the day on which the headspace was exchanged to pure N_2. Linear regression fit indicates a linear relation between biomass yields in different co-cultures conditions. Error bars represent one standard deviation of three independent measurements.



Supplementary Figure 4.10 | Carbon NMR spectrum depicting the produced isotope labeled acetate from ^{13}C labeled experiment (blue) and the unlabeled experiment (red) without any isotope labeled acetate.



Supplementary Figure 4.11 | *R. palustris nif*A* cultures with $^{15}N_2$ and Ar headspaces supplemented with 2mM and 4mM acetate. A) Total biomass yield for each condition. B) ^{1}H-NMR spectrum with $^{15}NH_3$ (blue) and no NH_3 for cultures grown with Ar (red).



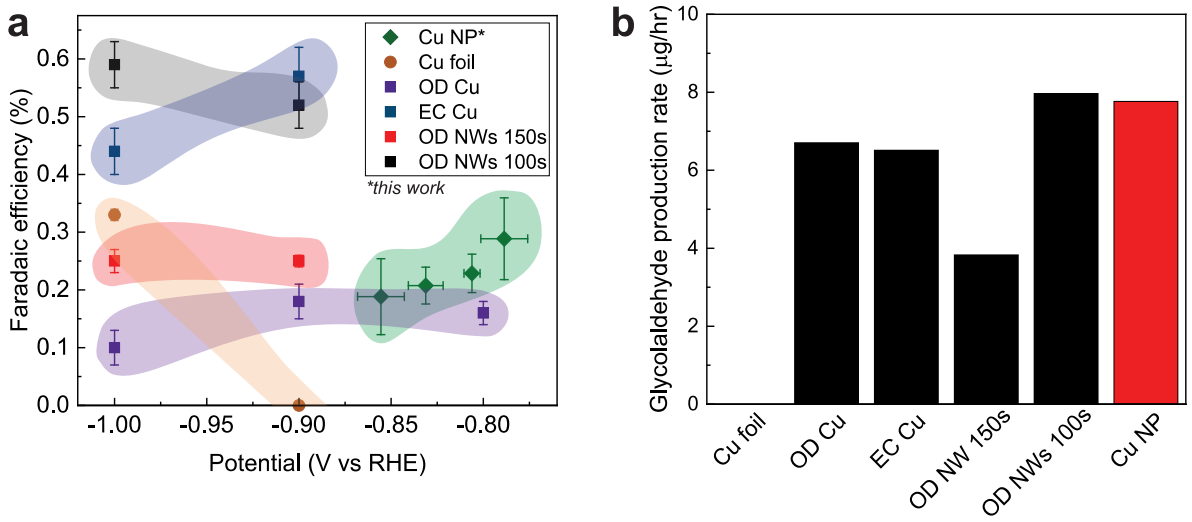
Supplementary Figure 4.12 | Scanning electron micrographs of pure a) *S. ovata* and b) *R. palustris nif*A* cultures on silicon nanowire arrays. c) *S. ovata* and *R. palustris nif*A* co-culture ultracentrifuged (12,000 RPM) showing separation of individual bacterial strains visible by color (*S. ovata* is yellow/beige and *R. palustris* is dark pink). The approximate final cell ratio is 2:3 *S. ovata* to *R. palustris nif*A*, having been seeded at a 6:1 *S. ovata* to *R. palustris nif*A* cell ratio. d) Scanning electron micrograph of *S. ovata* and *R. palustris nif*A* co-culture after a routine electrochemical experiment. *S. ovata* and *R. palustris* are false-colored yellow and pink respectively.

S.I.: Chapter 5

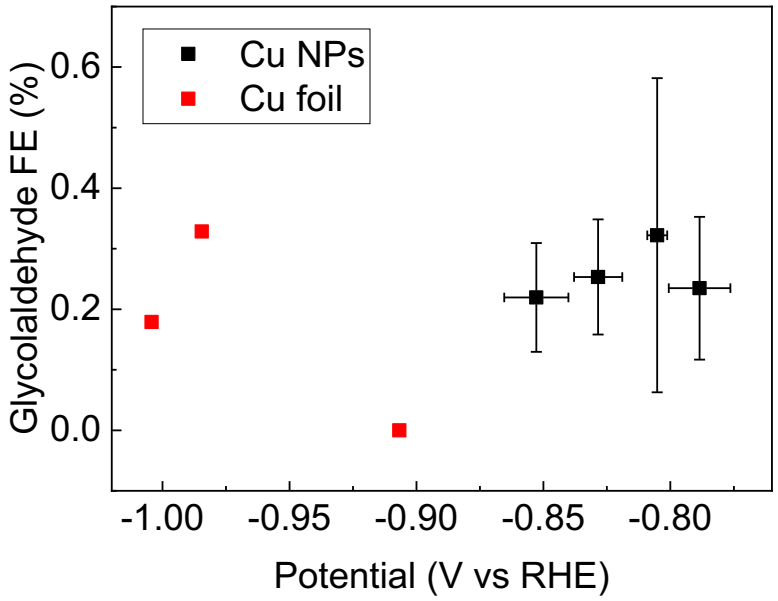
Supplementary Discussion 5.1: the CO_2 electroreduction to formaldehyde on BDD

Very few works have documented the CO_2 electrochemical reduction to formaldehyde using a boron doped diamond (BDD) electrode. Among them, Nakata *et al*. reports the remarkable electroconversion of CO_2 into formaldehyde using BDD with a FE up to 65% and 62% in a methanol and an aqueous electrolyte, respectively.[256] However, using the same experimental conditions as Nakata and coworkers, we measured a significantly lower turnover of CO_2 to formaldehyde. Additionally, their best catalytic performance was achieved in a methanol electrolyte which is not desirable in the following carbohydrate synthesis. The production of formaldehyde in aqueous media is for that purpose more suitable.

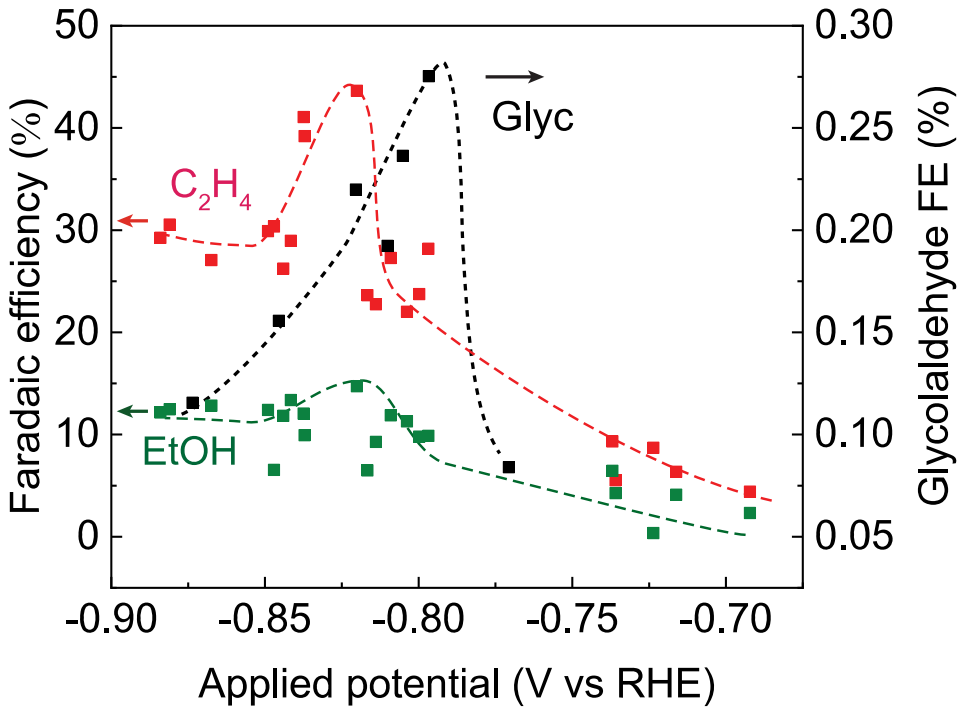
There are two main limitations to the electroproduction of formaldehyde from CO_2 in aqueous conditions that need to be considered. First, our work relies on the use of a commercial BDD electrode which likely possess limited catalytic properties. In their work, Xu and coworkers demonstrate that the degree of boron doping affects the hybridization of the BDD which determines the relative production of formic acid and CO.[257] Second, in presence of water, formaldehyde is likely to undergo the Cannizzaro disproportionation reaction and yield alcohol and carboxylic acid instead. This phenomenon was highlighted in the work of Birdja and Koper.[239] This reaction is typically promoted by the high concentration of hydroxide ions (OH^-) generated during the reduction of CO_2. To address this issue, the authors emphasize the importance of the electrolyte pH as well as buffer capacity to mitigate the impact of the Cannizzaro reaction. In fact, we detected more formic acid when using similar conditions as Nakata et al. Therefore, we decreased the electrolyte pH to maximize the stabilization of any formaldehyde produced.[258] While the overpotential necessary to produce formaldehyde was significantly improved in comparison to more neutral conditions (i.e., 790 mV more positive), the absolute formaldehyde concentration attainable after 1 hour of electrolysis remained limited to ~7 μM. Increase of the overpotential led to a rise in formate concentration which suggests the formation of favorable conditions for the Cannizzaro reaction. Additionally, extending the time of electrolysis from 30 min to 1 hour or 1.5 hours did not lead to a significant change of concentration. This observation further emphasizes the difficulty to accumulate formaldehyde in our system (**Fig. S6**). Overall, both a more thorough study of the catalyst and the reaction conditions are necessary to ultimately improve the rate and selectivity of the CO_2 electroreduction to formaldehyde.



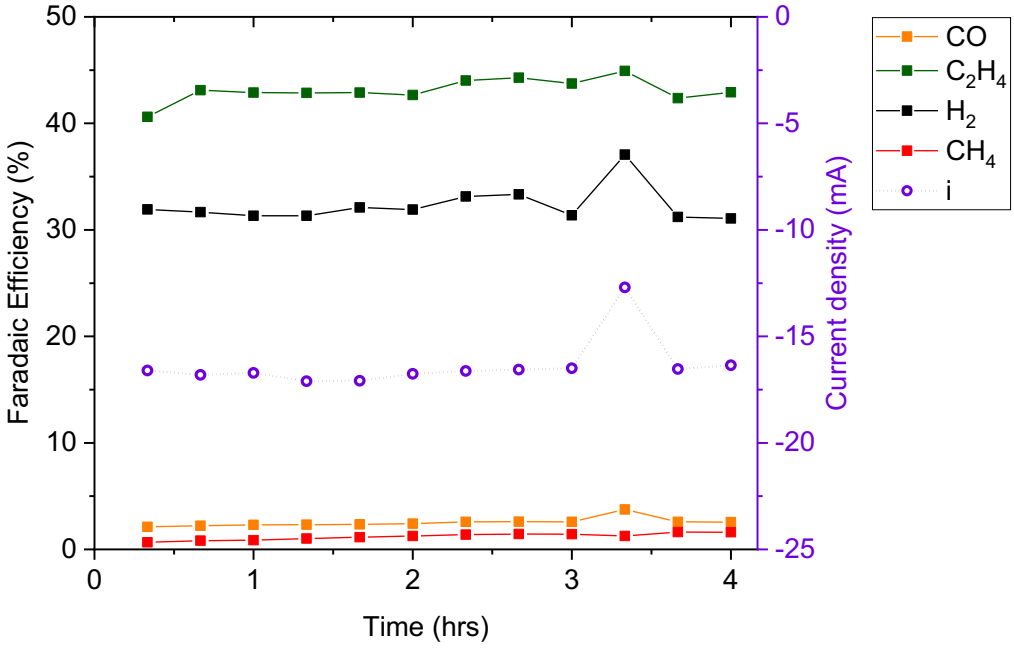
Supplementary Figure 5.1 | CO_2 electroconversion to glycolaldehyde performance across Cu catalyst. **(a)** Comparison of the glycolaldehyde faradaic efficiency of our Cu nanoparticle ensemble catalyst with other reported Cu-based catalysts as a function of the applied potential. **(b)** Comparison of the rate of glycolaldehyde production during CO_2 electrolysis between our Cu nanoparticle ensemble catalyst and various reported Cu-based catalysts at -0.86 V and -0.90 V vs RHE, respectively.



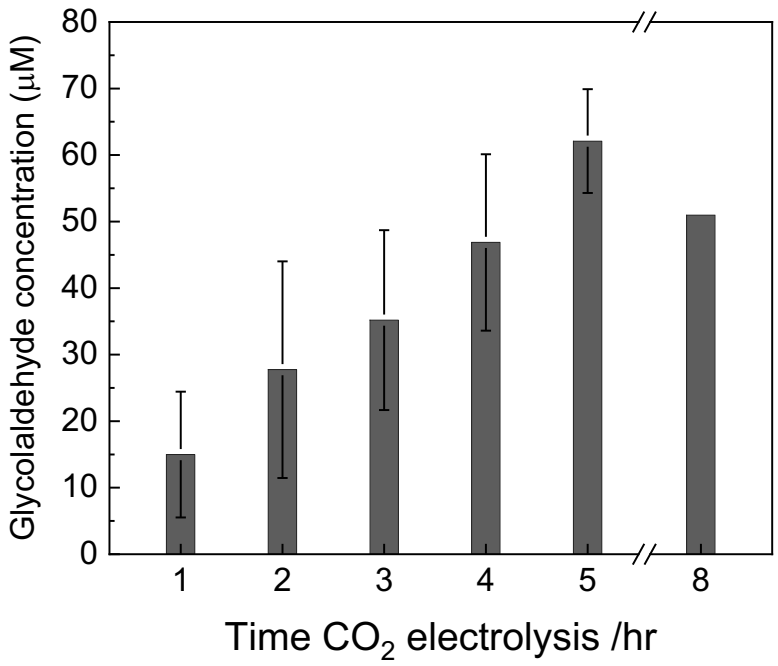
Supplementary Figure 5.2 | Glycolaldehyde faradaic efficiency of Cu foil and the Cu nanoparticle ensemble indicates an onset potential towards glycolaldehyde 100 mV more positive for the Cu nanoparticle-based catalyst. Error bars indicate one standard deviation of three independent measurements.



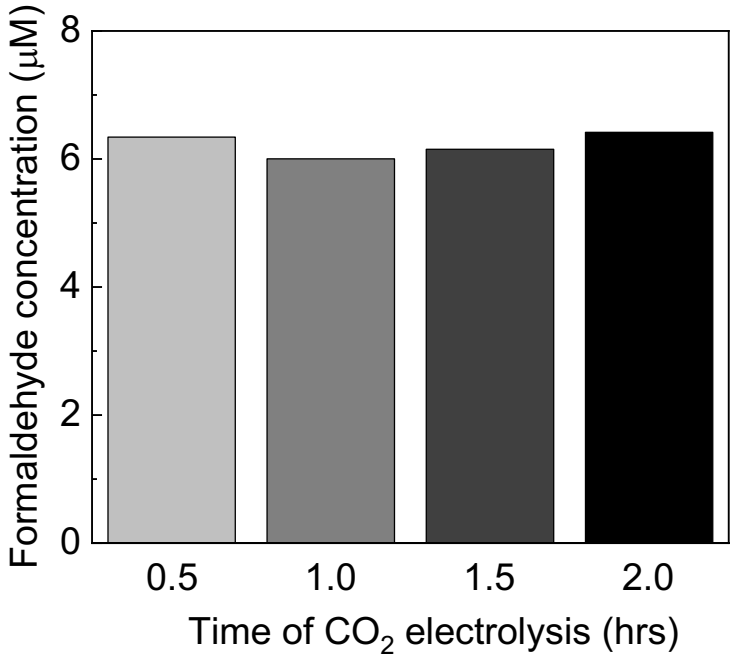
Supplementary Figure 5.3 | Comparison of the faradaic efficiency of glycolaldehyde (right y-axis) with ethylene and ethanol (left y-axis) using the Cu nanoparticle ensemble at various applied potentials.



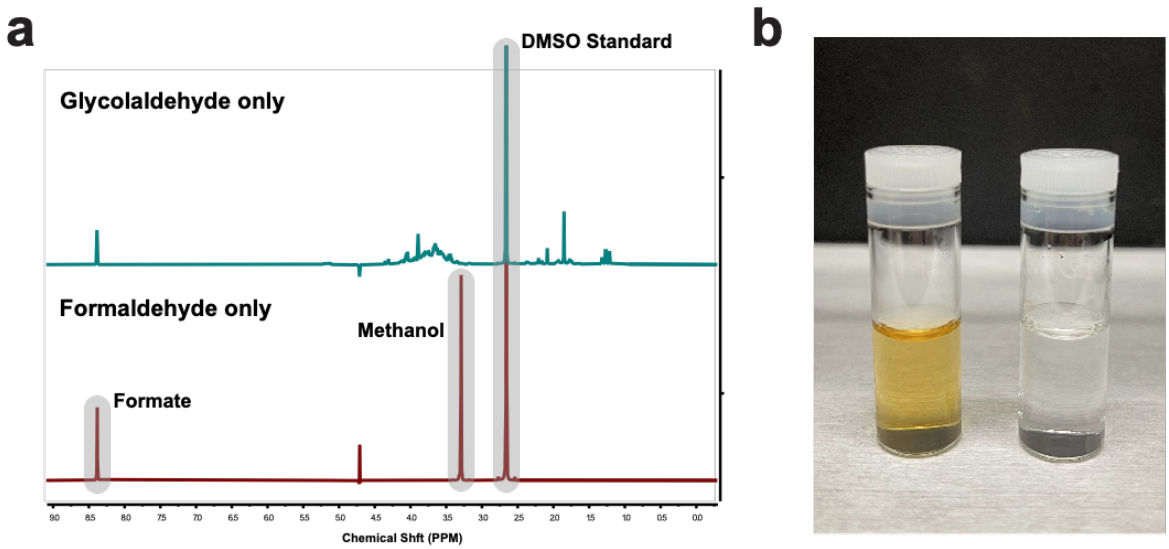
Supplementary Figure 5.4 | CO_2RR gas products faradaic efficiency (left y-axis) and total current density (right y-axis) monitored over time at 20 min interval for a total of 4 hours electrolysis.



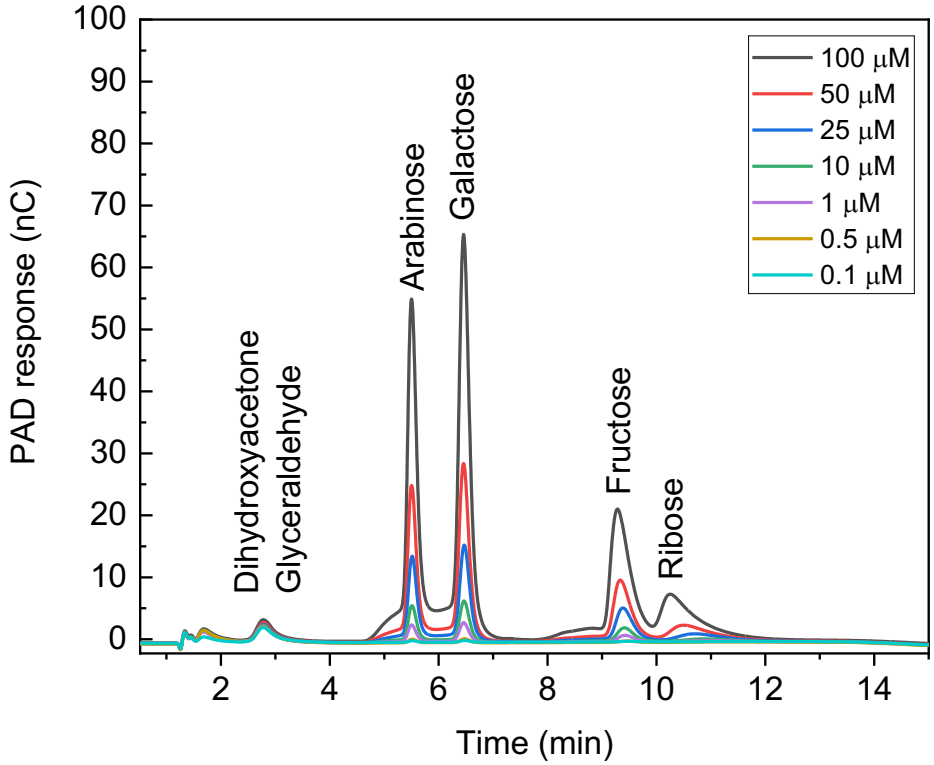
Supplementary Figure 5.5 | Glycolaldehyde concentration as a function of time of CO_2 electrolysis at -0.8 V vs RHE using the Cu nanoparticle ensemble. Error bars indicate one standard deviation of three independent measurements.



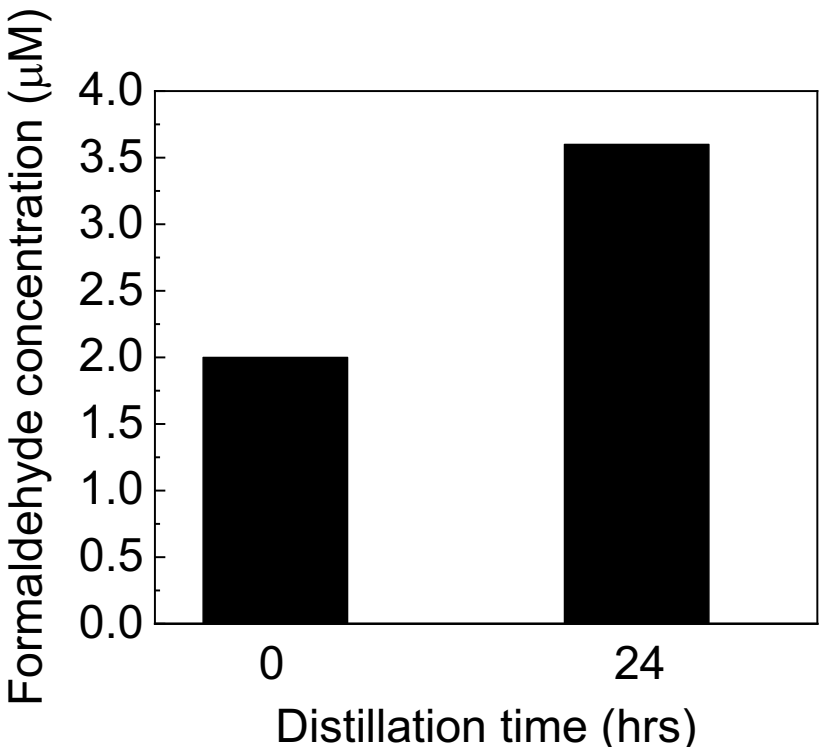
Supplementary Figure 5.6 | Formaldehyde concentration as a function of the time of CO_2 electrolysis using BDD electrode in 0.1 M $HClO_4$.



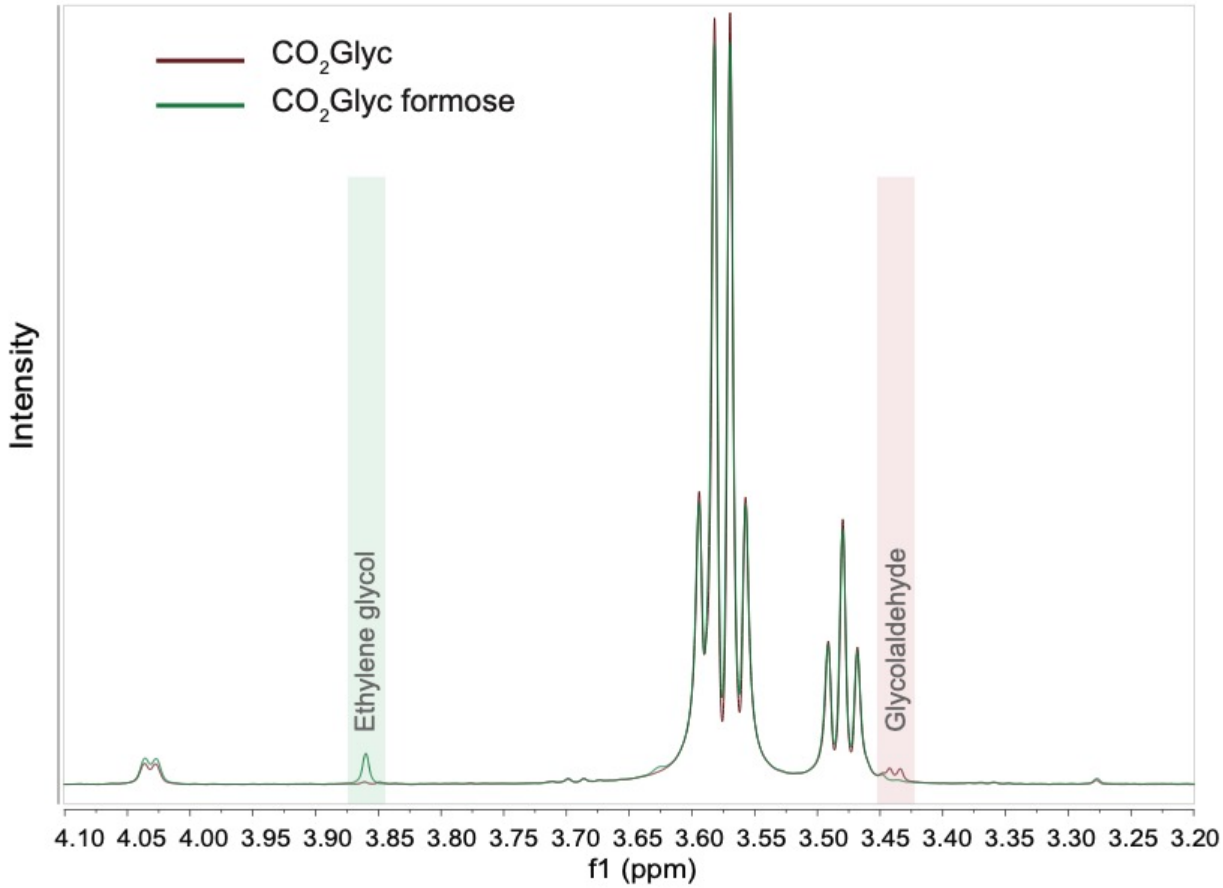
Supplementary Figure 5.7 | Formose reactions initiated either with solely glycolaldehyde or formaldehyde. **(a)** ^{1}H-NMR shows the formation of sugars with glycolaldehyde as the only precursor. Formaldehyde alone undergoes Cannizzaro disproportionation to form formate and methanol, but no sugars. **(b)** Formose reaction with glycolaldehyde depicts the characteristic yellow formose color (left) while the formose reaction initiated with formaldehyde remains clear (right).



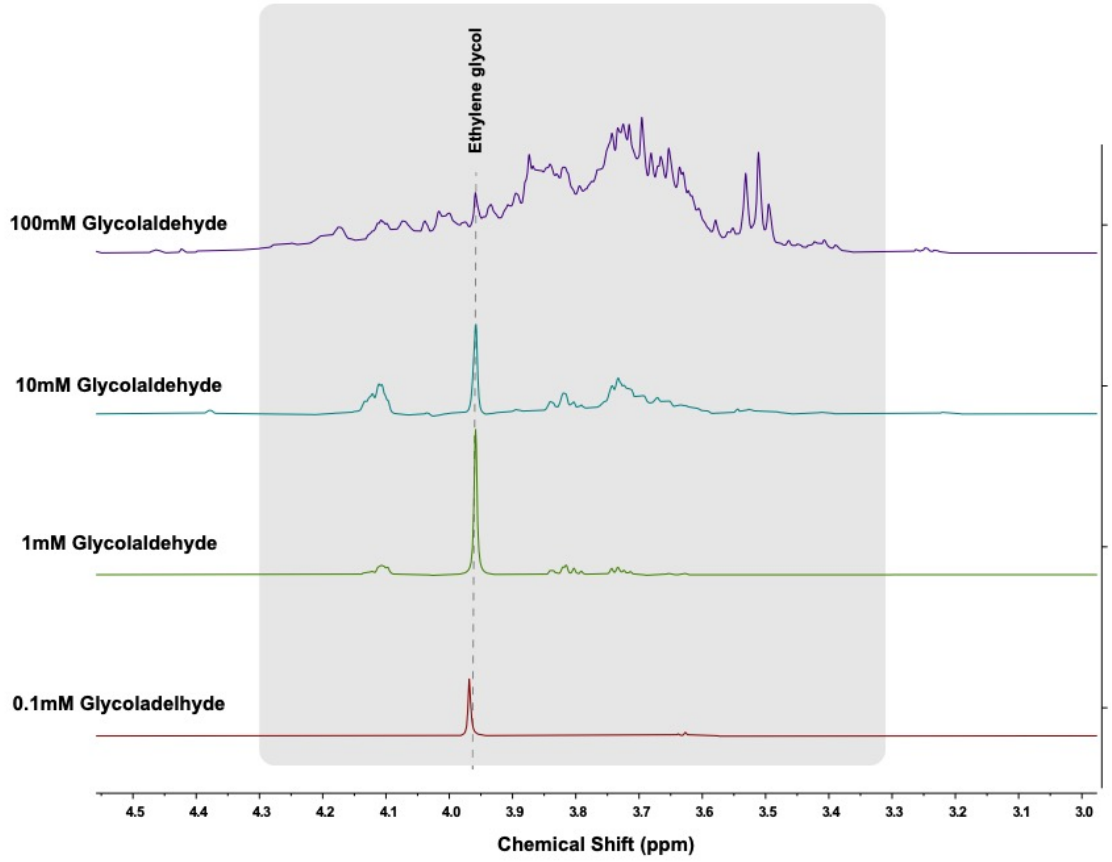
Supplementary Figure 5.8 | HPAEC-PAD chromatogram of a standard carbohydrates mixture with various concentration. Hexoses of identical molecular weight (e.g., glucose and fructose) are well-separated and allows their clear identification and quantification.



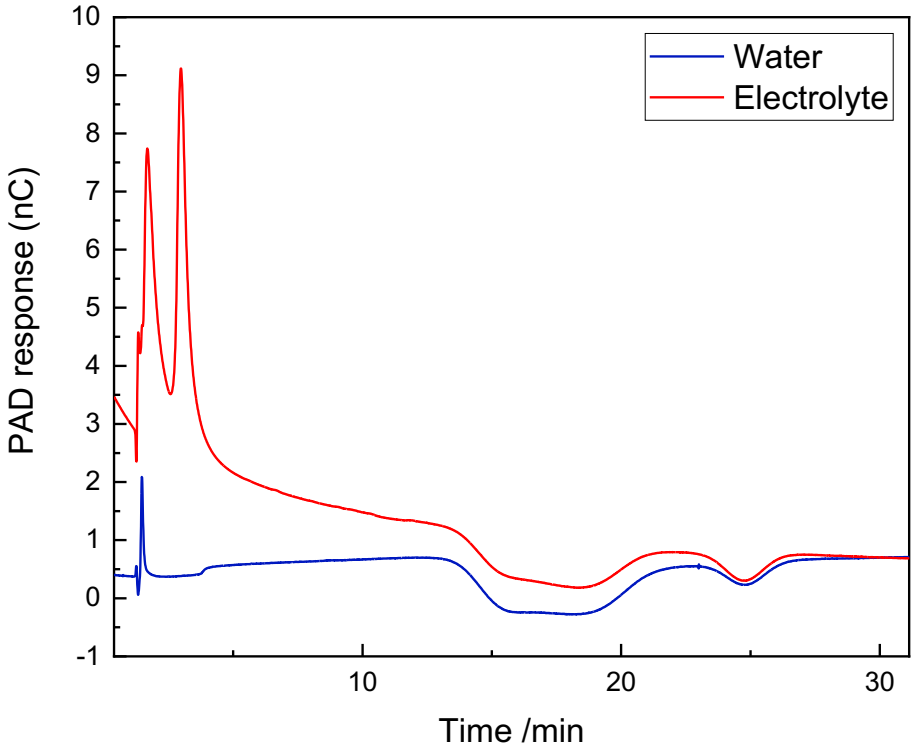
Supplementary Figure 5.9 | Increase of formaldehyde concentration in aqueous solution upon distillation processing.



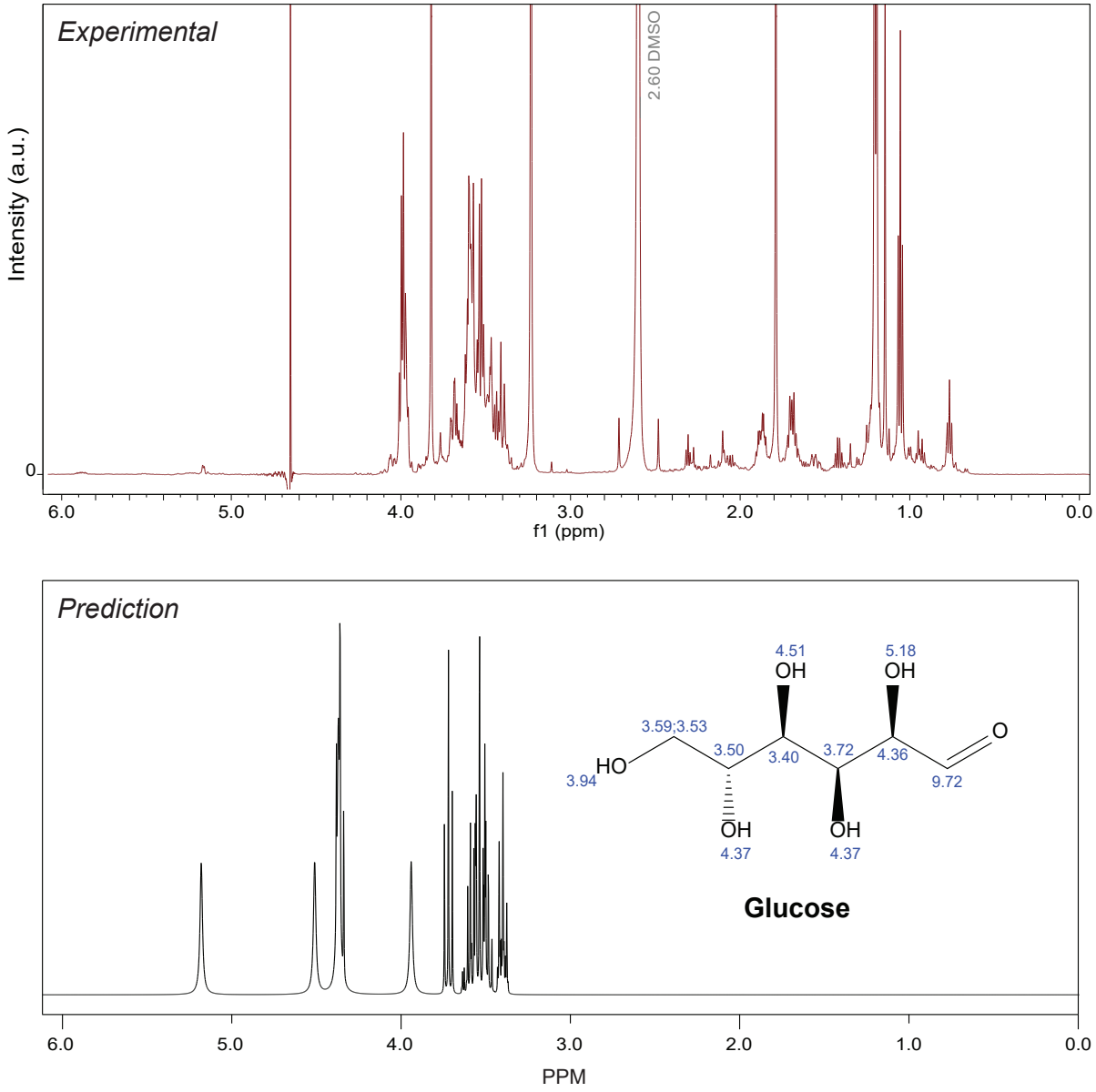
Supplementary Figure 5.10 | ^{1}H-NMR of CO_2Glyc before and after formose reaction in the absence of formaldehyde. The concentration of glycolaldehyde is too low to enable the formation of sugars. Instead CO_2Glyc is hydrogenated to form ethylene glycol.



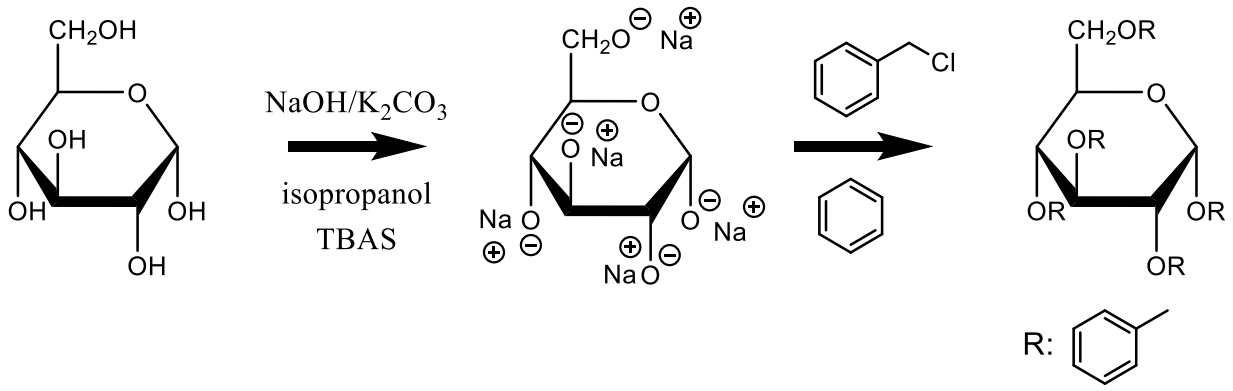
Supplementary Figure 5.11 | ^{1}H-NMR of formose reactions with glycolaldehyde as the sole starting aldehyde. Spectra by ascending order of the starting glycolaldehyde concentration demonstrate the effect of glycolaldehyde concentration on the effectiveness of the formose reaction to produce sugars. Shaded region indicates the chemical shift region for carbohydrate protons. Spectra show that glycolaldehyde, which has a signature peak at a chemical shift of 3.44ppm, is all consumed during the reactions.



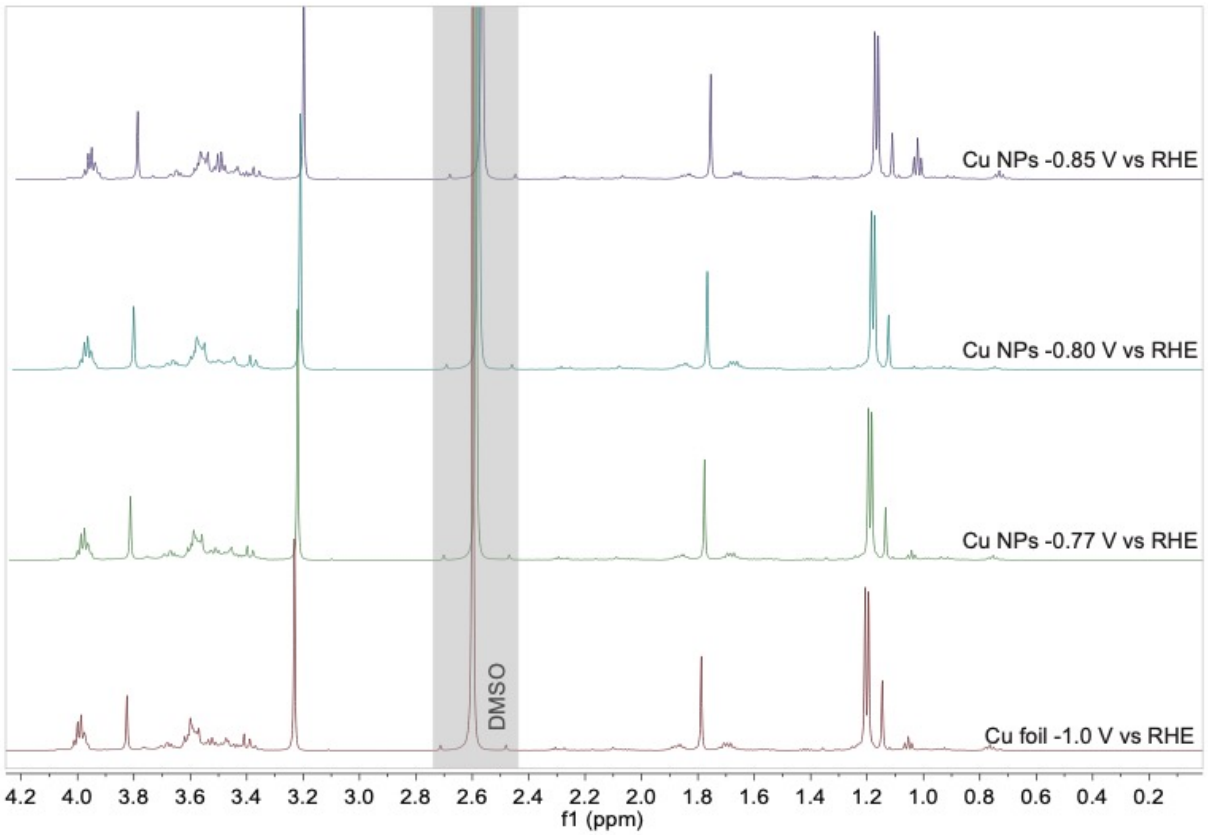
Supplementary Figure 5.12 | HPAEC-PAD background chromatograms for water (blue) and 0.1 M $KHCO_3$ electrolyte (red).



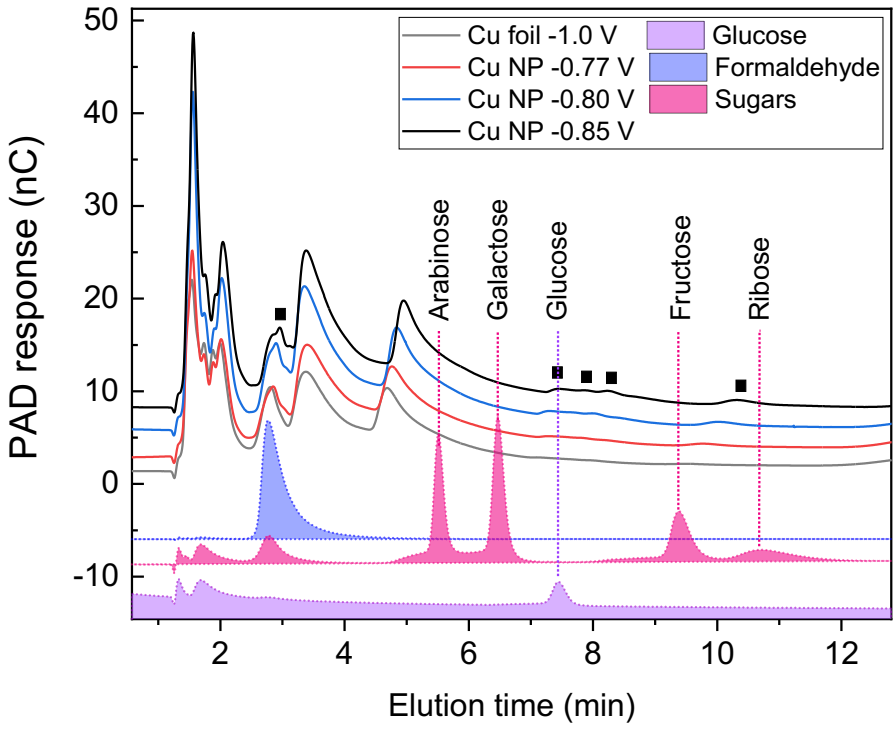
Supplementary Figure 5.13 | ^{1}H NMR signature of carbohydrates (e.g., glucose). Experimental spectra for CO_2Form sugars (top) and ChemDraw simulated peak positions of glucose proton signals.



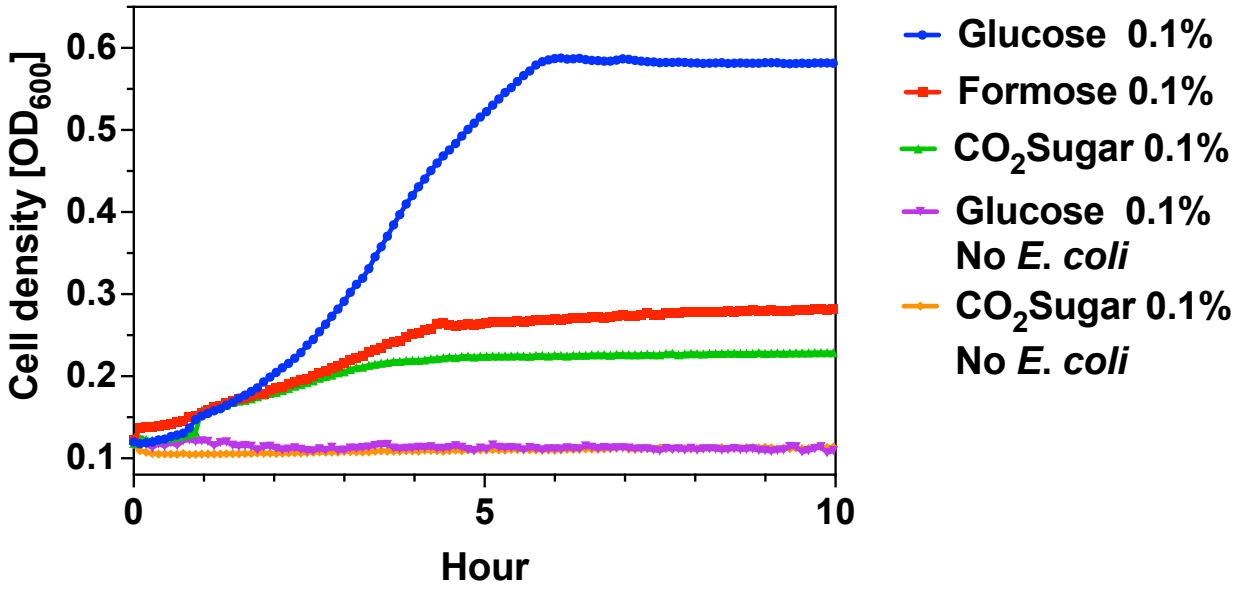
Supplementary Figure 5.14 |. Benzylation of carbohydrates (e.g., glucose is depicted here) to protect hydroxyl groups and perform liquid-liquid extraction of the CO_2Sugars to separate them from their aqueous phase. [234]



Supplementary Figure 5.15 | ^{1}H NMR spectra of CO_2Form sugars obtained from the output of CO_2Glyc obtained with Cu foil and at various applied potentials using the Cu nanoparticle ensemble.



Supplementary Figure 5.16 |. HPAEC-PAD chromatograms of CO_2Sugars produced using the post-electrolysis electrolyte generated using Cu foil and the Cu NP ensemble at various applied potentials. Peaks that correspond to formaldehyde and glucose become more pronounced at mor negative applied potentials with the Cu NP ensemble.



Supplementary Figure 5.17 |. Optical density plots of *E. coli* cultures grown with glucose, formose sugar, and CO_2Sugars Controls constitute of glucose and CO_2Sugars without *E. coli*

Lysogeny Broth

1L	Component
10g	Tryptone
5g	Yeast Extract
10g	NaCl

Supplementary Table 5.1

Add ultrapure H_2O to a 1L final volume (before use or scale accordingly). Autoclave before use.

M9 Minimal Medium

1L	Component
6g	Na_2HPO_4
3g	KH_2PO_4
0.5g	NaCl
1g	NH_4Cl

1L	Component
1mL	1M $MgSO_4$
1mL	0.1M $CaCl_2$

Supplementary Tables 5.2a and 5.2b

Add ultrapure H_2O to 5a components to a 1L final volume (or scale accordingly). After autoclaving add the final sterile components (5b) through a syringe filter. Add glucose, or other carbon source, from a sterile stock solution to a final desired concentration.